University of Sussex

Aspects of Quantum Gravity and Matter

Jan Schröder

Submitted for the degree of Doctor of Philosophy

University of Sussex

January 2015

UNIVERSITY OF SUSSEX

Jan Schröder, Doctor of Philosophy

Aspects of Quantum Gravity and Matter

Summary

A quantum theory of gravity remains one of the greatest challenges of contemporary physics. It is well established that a perturbative treatment of gravity as a quantum field theory leads to a non-renormalisable setup. However gravity could still exist as a consistent and predictive quantum field theory on a non-perturbative level. This is explored in the asymptotic safety scenario which was initially proposed by S. Weinberg.

In this thesis we investigate the ultraviolet behaviour of gravity within the asymptotic safety conjecture and discuss phenomenological implications. We start out by introducing the concept of the functional renormalisation group and its application to gravity. This non-perturbative tool is the technical basis for our investigation of a template quantum gravity action, namely a function $f(R)$ in the Ricci scalar in four dimensions. We compute exact fixed point solutions to very high polynomial orders via the development of a dedicated high performance code. The picture of an interacting UV fixed point that receives only small quantitative corrections from higher derivative operators is confirmed and extended.

The results are then expanded to include minimally coupled matter fields and we investigate the matter effects on the gravitational fixed point. We determine regimes of compatibility in the vicinity of the purely gravitational setup but also find constraints on the number of matter fields.

Finally we look at the phenomenological implications of a running Newton's coupling, one of the key features of the asymptotic safety setup, to graviton-mediated eikonal scattering amplitudes. In this kinematic regime we investigate the possibility of a TeV-sized fundamental Planck mass via the introduction of compact extra dimensions. We identify the fingerprints of asymptotic safety in the t-channel scattering amplitude and find crucial differences compared to semi-classical computations.

Acknowledgements

A research project of this scope is not possible without the guidance and expertise of a great supervisor. I wish to thank Daniel Litim for his encouragement, support and the always enlightening discussions.

I am devoted to Kathi. She brings so much happiness into my life. Her ongoing support and warm understanding are invaluable and precious to me.

I feel incredibly fortunate to have encountered extraordinary friends over the years, in chronological order Kris, Sebastian and Nina. Thank you for always being there when it counts!

I am very grateful to my parents for inspiring my enduring love of nature and physics.

Sussex was a great place to study and there are many people who made it so much more than just a place to work. I'm deeply indebted to Laura and Barry for their never-ending hospitality. I enjoyed legendary parties and inspiring discussions with Kevin, Edouard, Rob, Tugba, Mateja, Andy, Aga, Kostas, Glauber, Ting-Cheng, Mike, Raul, Jorge, Jose, Ken, Djuna, Heather, Nicola, Chris and Christopher.

This work was supported by the *Studienstiftung des deutschen Volkes*.

The most terrifying fact about the universe is not that it is hostile but that it is indifferent; but if we can come to terms with this indifference and accept the challenges of life within the boundaries of death - however mutable man may be able to make them - our existence as a species can have genuine meaning and fulfillment. However vast the darkness, we must supply our own light.

- Stanley Kubrick [1]

Contents

List of Tables

List of Figures

Chapter 1

Introduction

Quantum field theory has proven to be one of the most successful and versatile frameworks in physics. It successfully combines the principles of special relativity with those of quantum physics to describes a whole range of interactions, such as quantum chromodynamics and electroweak interactions. It is not only limited to fundamental forces of nature, but can also be applied to effective models in solid state physics. There is a range of techniques available which allow for a consistent and systematic approach when calculating observables: perturbation theory, lattice simulations, Schwinger-Dyson equations and functional RG.

In this context the highly successful theory of general relativity proves to be a challenge, as it cannot be perturbatively quantised. In a perturbative expansion of the dimensionless Newton's coupling in four spacetime dimensions $g = G_N E^2$, where G_N is the dimensionful Newton's coupling and E denotes an energy scale, canonical power counting already suggests the perturbative non-renormalisability, as G_N has negative mass dimension -2. When examined in more detail it is found that the theory becomes perturbatively non-renormalisable at two loop level [3]. The presence of matter fields actually shifts the perturbative non-renormalisability already to the one loop level [4].

These results have raised the question whether gravity can exist as fundamental quantum field theory, and thereby inspired a whole range of approaches to gravity at high energies such as string theory [5] and loop quantum gravity [6]. In these approaches one has to make different assumptions about the fundamental nature of spacetime compared to classical general relativity which serves as the classical limit.

However there is compelling evidence that gravity can be meaningful within the quantum field theory framework when one makes use of non-perturbative methods. This is a conservative approach because it aims to understand gravity without further postulates about

its fundamental nature. First hints already arise at the perturbative level. If one treats the spacetime dimensionality as a continuous parameter, a perturbatively meaningful regime can be identified close to 2 dimensions in an ϵ expansion [7, 8, 9].

For small energies, gravity can be successfully studied via an effective field theory approach with a UV cutoff at the Plack scale [10] (for review see [11]).

Going beyond the Einstein-Hilbert action, there are stabilising effects for perturbation theory from higher derivative operators [12]. There can even be a fully perturbatively renormalisable theory of gravity including all fourth order derivative operators [13]. However, it cannot be a contender for a fundamental theory of gravity as it violates unitarity.

A breakthrough was achieved via Weinberg's seminal idea to go beyond perturbative renormalisability as criterium for a predictive quantum field theory [7]. It has inspired a whole body of work investigating the non-perturbative properties of gravity (cf. [14, 15, 16, 17, 18, 19, 20, 12, 21] for reviews). In order for a meaningful UV-behaviour of gravity to exist within the framework of quantum field theory, it must be governed by an interacting fixed point of the couplings that has only a finite number of relevant directions. Thereby gravity would be completely described by a finite number of parameters in the high energy limit. The interacting fixed point can be attained as the anomalous dimension can grow large for non-vanishing coupling values and thereby counterbalance the canonical dimension.

The main tool for this non-perturbative examination is the functional renormalisation group (further details in Chapter 2) as introduced by [22, 23] and its application to gravity [24]. It is rooted in the renormalisation group as introduced by Wilson [25, 26] and its application to a path integral description of quantum field theory. A momentum separation scale k is introduced to discriminate between high and low momentum modes. The high momentum modes are fully integrated out whereas the low momentum modes are suppressed. The infinitesimal change with respect to the separation scale k is then determined by integrating out only infinitesimal momentum shells around k. This is described by a flow equation for an effective average action Γ_k, a scale dependent version of the full quantum effective action. It leads to scale dependent correlation functions and couplings, which have the interpretation of encoding the physics at this particular momentum scale k. The effective average action contains the operators and couplings of the theory, and the flow equation describes the running with the renormalisation group scale k.

For gravity the theory space in terms of allowed operators in the running effective ac-

tion, Γ_k, is a priori only constrained by diffeomorphism invariance. Therefore an infinite number of operators with associated couplings are in principle allowed. At present date a calculation including all diffeomorphism invariant operators is not feasible. One of the main approximations within this analysis is to pick a finite amount or an infinite class of operators for which the RG-running in the framework of the functional renormalisation group can be calculated. The approximation is then justified a posteriori by showing the stability of its fixed point behaviour against the inclusion of further operators. The stability is still a question of ongoing research.
Strong evidence for the existence of a non-trivial fixed point exists within various approximation approaches [24, 27, 28, 29, 30, 31, 32, 33, 34, 35, 36, 37, 38, 39].
In Chapter 3 of this thesis we focus on a systematic study of a template action for quantum gravity, building on the work of [39, 40]. We investigate a class of operators known as ploynomial $f(R)$ gravity. It is of particular importance since it includes the Einstein Hilbert effective action as a subset and features generically an infinite set of operators with increasing mass dimension. Here we will investigate the UV fixed point properties under subsequent addition of higher polynomial orders in the $f(R)$ effective action.

As already noted matter can have a strong influence on the behaviour of perturbative gravity [4]. Therefore the question of matter implications to the asymptotic safety scenario [41, 42, 43, 44, 45, 46, 47, 48, 49, 50, 51, 35, 52] not only naturally arises but is also of great importance. In Chapter 4 we will extend the setup of Chapter 3 with the introduction of minimally coupled matter fields and investigate their impact on the fixed point and its properties.

In the final part of the thesis, Chapter 5, we consider phenomenological effects of the running Newton's coupling as predicted by asymptotic safety [32, 53, 54]. We examine the kinematic regime of eikonal scattering for graviton-mediated processes [55, 56] in spacetimes with compact and flat extra dimensions. These extra dimensions may facilitate a TeV-sized fundamental Planck mass [57] and can thereby move quantum gravity effects within the reach of current particle accelerators, in particular the LHC [58, 59, 60, 61, 62, 63].

Chapter 2

Functional renormalisation

In this chapter we will review the techniques necessary to calculate the beta-functions for our setup of gravity and introduce our notation and conventions. We will consider gravity within the framework of quantum field theory. As general relativity is perturbatively non-renormalisable [3, 4] (cf. Chapter 1), we will have to rely on non-perturbative approaches. Broadly applied techniques are functional renormalisation, Schwinger-Dyson equations and lattice methods. Here we will focus on the functional renormalisation group [22, 23] which employs a Wilson-type coarse graining procedure [25, 26]. Functional renormalisation is a powerful method and has proven its usefulness in a wide a range of applications to quantum chromodynamics, solid state physics and gravity. We will here focus on its application to gravity [24] and derive a flow equation for polynomial $f(R)$ gravity in the spirit of [34]. Generally we will follow the reviews in [64, 65, 18, 66, 67]. For an introductory overview to quantum field theory, we refer to the textbook [68].

2.1 Effective action

Any observable linked to a quantum field theory, eg. a scattering amplitude, can be calculated using n-point correlation functions of the underlying quantum fields:

$$\langle \varphi(x_1) \dots \varphi(x_n) \rangle \tag{2.1}$$

These n-point correlators can be expressed via the path integral formalism, using a weighted integral over all possible and allowed field configurations:

$$\langle \varphi(x_1) \dots \varphi(x_n) \rangle = \frac{\int \mathcal{D}\varphi \, \varphi(x_1) \dots \varphi(x_n) \, \exp(-S[\varphi])}{\int \mathcal{D}\varphi \, \exp(-S[\varphi])} \tag{2.2}$$

Here the underlying spacetime is Euclidean and $S[\varphi]$ is the action governing the physical theory. The functional integral in (2.2) is still not rigorously defined at this point and

generally requires further specification through a regularisation procedure to become well-defined. We will provide this in Section 2.2.

An elegant way of expressing the n-point correlation functions is via the generating functional $Z[J]$, which introduces a dependence on an external source term J:

$$Z[J] \equiv \exp(W[J]) = \int \mathcal{D}\varphi \, \exp\left(-S[\varphi] + \int J\,\varphi\right). \tag{2.3}$$

Derivatives of the generating functional, with respect to the source J at $J = 0$, yield n-point functions of the theory. The same is true for W, which gives n-point functions of connected diagrams. Either functional contains the information of the theory.

The source-dependent vacuum expectation value of the field φ is called the classical field ϕ and arises for the first derivative of W with respect to the source J:

$$\phi \equiv \frac{\delta W[J]}{\delta J} = \frac{1}{Z[0]}\frac{\delta Z[J]}{\delta J} = \langle\varphi\rangle_J. \tag{2.4}$$

It can be used to define yet another functional containing the full information of the theory via a Legendre transform of $W[J]$, the effective action Γ,

$$\Gamma[\xi] = \sup_J \int \xi\, J - W[J]. \tag{2.5}$$

The supremum value is attained if ξ is equal to the classical field $\phi = \delta W/\delta J$. Thereby we have

$$\Gamma[\phi] = \int \phi\, J - W[J] \tag{2.6}$$

as a convex functional in the classical field. It generates the one-particle irreducible correlation functions. The effective action can be viewed as the quantum counterpart of the classical action S since it satisfies an analogous equation of motion

$$\frac{\delta\Gamma[\phi]}{\delta\phi} = J. \tag{2.7}$$

And J is the source of the quantum fluctuations.The classical equations of motion do not exhibit such a source term.

The second functional derivative of the effective action, with respect to J, corresponds to the inverse exact propagator (2 point correlator) of the theory.

From the definition of the effective action (2.6) it is clear that it can be re-expressed via the insertion of (2.3) and (2.4) into the exponentiation of (2.6) and turned into a defining equation without any explicit dependence on the external source J:

$$\exp(-\Gamma[\phi]) = \int \mathcal{D}\chi \, \exp\left(-S[\phi+\chi] + \frac{\delta\Gamma[\phi]}{\delta\phi}\,\chi\right). \tag{2.8}$$

Here, a shift in the integration field $\chi = \varphi - \phi$ has been used. This integro-differential equation is the starting point for a vertex expansion of the the effective action

$$\Gamma[\phi] = \sum_{n=0}^{\infty} \frac{1}{n!} \int d^D x_1 \cdots d^D x_n \Gamma^{(n)}(x_1, \cdots, x_n)\, \phi(x_1) \cdots \phi(x_n), \tag{2.9}$$

where D denotes the dimensionality of the underlying spacetime. Subsequent insertion of (2.9) into (2.8) yields a series of equations to determine the vertex coefficients $\Gamma^{(n)}$ which correspond to the one particle irreducible proper vertices. These equations are the Dyson-Schwinger equations.

2.2 Renormalisation group

The effective average action $\Gamma_k[\phi]$ is a scale-dependent functional that interpolates between the bare action $S = \Gamma_{k\to\infty}$ and the full quantum effective action $\Gamma = \Gamma_{k=0}$. This functional can be viewed as a scale dependent version of the effective action (2.6) and is the central quantity within the framework of the functional renormalisation group. It includes a regularisation procedure and is therefore better defined than the generating functional (2.3). The momentum scale k discriminates between high momentum modes, $p^2 \gg k^2$, and low momentum modes, $p^2 \ll k^2$, of the field φ. The low momentum or IR modes will be suppressed, whereas the high momentum or UV modes will be integrated out. At the level of the scale-dependent generating functional $Z_k[J]$, this amounts to a momentum dependent mass term as a regulator $\mathcal{R}_k$:

$$Z_k[J] \equiv \exp(W_k[J]) = \int \mathcal{D}\varphi \, \exp\left(-S[\varphi] + \int J\,\varphi - \int \frac{1}{2}\,\varphi\,\mathcal{R}_k(-\partial^2)\,\varphi\right). \tag{2.10}$$

The specific shape of the regulator $\mathcal{R}_k$ is subject to constraints in its high and low momentum limits:

$$\mathcal{R}_k(p^2) \to \begin{cases} k^2 & p^2 \ll k^2 \\ 0 & p^2 \gg k^2 \end{cases}. \tag{2.11}$$

For a discussion of the fundamental properties this limiting behaviour is enough and knowledge of the specific shape is not needed.

In the limit of $k \to 0$, the whole regulator term vanishes from the generating functional $Z_k[J]$, and we fall back onto the scale independent generating functional $Z[J]$ (2.3). In the limit of $k \to \infty$, we encounter a heavy suppression of all modes. Therefore the integral will be dominated by a stationary point of the exponent.

For explicit calculations the shape of the regulator becomes very important as it has direct influence on the stability and convergence of the flow (2.13) [69, 70, 71, 72, 73].

The effective average action Γ_k is defined analogously to the effective action in (2.5) except for an additional regulator dependent term that ensures the UV limit $\Gamma_{k\to\infty} = S$:

$$\Gamma_k[\phi] = \left(\sup_J \int \phi\, J - W_k[J]\right) - \int \frac{1}{2}\,\phi\,\mathcal{R}_k(-\partial^2)\,\phi. \tag{2.12}$$

Again the supremum condition is satisfied for the now k-dependent field condition $\phi = \delta W_k[J]/\delta J$.

The effective average action can be interpreted as continuous interpolation between the bare action S and the full quantum effective action Γ. At a given scale k, it encodes the physics relevant for this energy scale as higher momenta/energies are integrated out and lower momenta/energies are suppressed. The effective average action, introduced in Section 2.2, allows for a continuous interpolation between the full quantum effective and the bare action. One can subsequently integrate out momentum shells to vary the renormalisation scale k. This evolution is governed by an exact, first order differential equation [22, 23]:

$$k\,\partial_k\,\Gamma_k[\phi] = \frac{1}{2}\mathrm{Tr}\left[\frac{k\,\partial_k\,\mathcal{R}_k}{\Gamma_k^{(2)} + \mathcal{R}_k}\right]. \tag{2.13}$$

This is the central equation of the exact functional renormalisation group (FRG). $\Gamma_k^{(2)}$ denotes the second functional derivative of Γ_k with respect to the field (Hessian). It can be directly derived from first principles without any approximations and is therefore exact. It exhibits a one-loop structure where it can be shown that $(\Gamma_k^{(2)} + \mathcal{R}_k)^{-1}$ is the connected 2-point function (propagator) of the theory.

The flow (2.13) has a very close relationship to the Callan -Symanzik equation ($\mathcal{R}_k \to k^2$) [74] and, via a Legendre transformation, to the Wilson-Polchinski equation [19, 75, 64]. In the local potential approximation the equivalence between the flow (2.13) and the Wilson-Polchinski equation is only exact for the optimised regulator. This was first demonstrated in [76], formallly shown in [77] and numerically confirmed in [78].

The flow equation (2.13) constitutes an a priori non-perturbative tool to examine quantum field theories. However, in the approximation of weak couplings, it reproduces standard perturbation theory to all loop orders [79, 80]. The main application of (2.13) lies in systematic approximations that go beyond the weak coupling limit such as the derivative expansion and the vertex expansion. Within these approaches, the stability and and convergence can be assessed and optimised via certain techniques [69, 70, 71, 72, 73]. Systematic uncertainties can be assessed as well [81].

In order to calculate the flow of Γ_k for a given theory of fields that respects certain symmetries and lives in a particular spacetime dimensionality, one has to consider all compatible operators of the theory. Assuming that there is a local functional basis, the effective average action is simply a sum over all compatible operators $\mathcal{O}_i$ dressed with their associated couplings g_i:

$$\Gamma_k[\phi] = \sum_i g_i \, \mathcal{O}_i. \tag{2.14}$$

Typically the number of compatible operators is infinite. Thus, any explicit calculation of the flow relies on the choice of a finite subset of operators which constitutes an approximation. Please note that this is a priori no perturbative approximation as no constraint on any coupling values being small is imposed at this point. This approximation constitutes a truncation of the theory space and can be justified by showing that the inclusion of further operators only leads to minor corrections in physical observables. In setups such as gravity, the approximation is usually justified a posteriori by demonstrating the minor corrections through explicit studies.

The introduction of an approximation to the flow equation (2.13) also leads to a non-trivial regulator dependence of the flow [82, 83, 84], which vanishes in the limit $k \to 0$, as this removes the regulator. Therefore some regulator choices might prove to be better suited for certain approximations than others [69, 70].

2.3 Gravitatonal renormalisation group

The flow equation (2.13) from Section 2.2 has various applications in different fields of theoretical physics such as quantum chromodynamics or solid state physics. We are particularly interested in a formulation for gravity. In this section we will introduce the basic ideas and terminology to construct a background field independent flow [24]. In the following Section 2.4 we give details to explicitly construct such a flow for an effective average action that encodes the gravitational dynamics as a function of the scalar curvature $f(R)$ [34]. The aim of this is to provide ourselves with all the necessary tools for the analysis in the subsequent Chapters 3 and 4.

The principal symmetry for general relativity is diffeomorphism invariance or general coordinate transformations. As the metric $\gamma_{\mu\nu}$ is taken as the carrier of the fundamental degrees of freedom, the path integral of the generating functional will be a functional integral with the measure $\mathcal{D}\gamma_{\mu\nu}$. A gauge fixing condition is now needed to eliminate

physically equivalent metric configurations from the path integral. This leads to a functional determinant in the path integral which can be reexpressed as an additional term in the action. In order to facilitate the transformation into an additional action term, new fields need to be introduced which violate the spin statistic theorem. The fields are not physical and referred to as Faddeev-Popov ghosts. They should be thought of as a mathematical trick and not as physical objects. Correspondingly the additional terms in the generating functional are called ghost terms.

In order to retain a notion of diffeomorphism invariance on the level of the action S, we employ the background field method [24, 73, 85, 86, 87], where the metric is decomposed into a fluctuation part $\tilde{\gamma}_{\mu\nu}$ and a background part $\bar{\gamma}_{\mu\nu}$:

$$\gamma_{\mu\nu} = \tilde{\gamma}_{\mu\nu} + \bar{\gamma}_{\mu\nu}. \tag{2.15}$$

The background is viewed as fixed and non-propagating. Its explicit form is a priori arbitrary and only needs to be specified later for an explicit evaluation (cf. Section 2.4, where a spherically symmetric background is chosen in (2.24) and (2.25)). Any field, including the fluctuating metric, is thought of as living on this background and transforming according to the coordinate transformations of the background metric. The generating functional Z_k has the structure

$$Z_k = \int \mathcal{D}\gamma_{\mu\nu}\, \mathcal{D}\bar{C}_\mu\, \mathcal{D}C_\mu\, \mathcal{D}b_\mu\, \exp\left(-S[\gamma] - S_{\rm gf}[\gamma] - S_{\rm gh}[\gamma, C, \bar{C}, b] - S_{\rm source} - S_{\rm reg}\right), \tag{2.16}$$

where $S_{\rm gf}$ represents the gauge fixing, $S_{\rm gh}$ the ghosts, $S_{\rm source}$ the source terms and $S_{\rm reg}$ the regulator terms. The ghost fields, arising from the Faddeev-Popov procedure, are an anti-commuting complex-conjugate pair C_μ and $\bar{C}_\mu$ and a commuting real ghost b_μ.

In analogy to the previously dicussed bare scalar field φ (Sections 2.1, 2.2), for gravity we have so far discussed a set of bare fields $\varphi = \{\gamma, C, \bar{C}, b\}$ following the bare action $S_{\rm bare} = S + S_{\rm gf} + S_{\rm gh}$. Now we switch to the effective average action Γ_k, which is a functional of the corresponding expectation values $\phi = \{g, z, \bar{z}, B\}$. It is defined as

$$\begin{aligned}&\exp(-\Gamma_k[\phi;\bar{g}])\\ &= \int \mathcal{D}\varphi\, \exp\left(-S_{\rm bare}[\gamma;\bar{g}] + \int (\varphi-\phi)\frac{\delta}{\delta\phi}\Gamma_k[\phi;\bar{g}]\right) - \frac{1}{2}\int (\varphi-\phi)\,\mathcal{R}_k[\bar{g}]\,(\varphi-\phi),\end{aligned} \tag{2.17}$$

where φ and ϕ are now understood as vectors of fields as defined above. The regulator term is again quadratic in the fields.

The flow equation for gravity then has the form

$$k\,\partial_k\,\Gamma_k[\phi;\bar{g}] = \frac{1}{2}\,\mathrm{STr}\left[\frac{k\,\partial_k\,\mathcal{R}_k[\bar{g}]}{\Gamma_k^{(2)}[\phi;\bar{g}]+\mathcal{R}_k[\bar{g}]}\right]. \tag{2.18}$$

The supertrace STr is understood as sum over all fields ϕ, a contraction over all indices and an integral over all momenta in momentum space.

The momenta in $\mathcal{R}_k$ are measured with respect to the background metric $\bar{g}$, eg. via $-\bar{\nabla}^2$, where $\bar{\nabla}$ is the background covariant derivative. This procedure leads to a flow equation for $\bar{g}$ [87, 49] similar to (2.18). We will identify the background metric $\bar{g}$ with the dynamical mean field metric g and thereby the background metric is dynamically adjusted along the flow. This is consistent with the interpretation that the metric constitutes both a background and a dynamical object at the same time.

There is also an alternative treatment available, where both the dynamics of the propagating and the background field are retained independently. For these so-called bi-metric approaches see [37, 88, 89, 90, 91]. Complementary approaches are presented in [92, 93, 94].

2.4 Quantum gravity

In this section we consider the application of the functional flow equation (2.18) to polynomial $f(R)$ gravity. We view it as a template action for quantum gravity because it includes the essential gravitational couplings, the cosmological constant and Newton's coupling, as well as infinitely many higher operators of increasing mass dimension.

Previous studies started out by considering the Einstein-Hilbert approximation which retains the terms that govern classical general relativity. It can be viewed as the subset of the $f(R)$ approximation where only terms up to linear order in R are considered. These studies [24, 41, 95, 29, 30, 96, 31, 32, 94] established a picture of a non-gaussian fixed point that governs the UV of gravity and exhibits a finite number of relevant directions. The Einstein-Hilbert approximation was also analysed for non-trivial IR fixed points [92, 93, 97, 98]. The results of the Einstein-Hilbert approximation proved to be remarkably stable under extensions of the Einstein-Hilbert picture, such as higher derivative operators [30, 33, 34, 99, 100, 101, 102, 39, 40] or quantum fluctuations in the ghost sector [36, 103, 104]. Conceptual extensions are the consideration of higher dimensions $d > 4$ [32, 53, 54] and the inclusion of matter fields [41, 42, 43, 44, 45, 46, 47, 48, 49, 50, 51, 35, 52]. Reviews can be found in [54, 21, 12, 20, 105, 17, 16].

Another direction is the subsequent addition of higher powers of the Ricci scalar to the Einstein-Hilbert action. This is known as polynomial $f(R)$ gravity [34, 99, 100]. So far

a picture of a three dimensional attractive surface at the UV fixed-point could be established up until order R^{34} [39, 40]. Here we will extend this picture until R^{70} (cf. Chapter 3).

Since we want to consider polynomial $F(R)$ gravity, we choose the ansatz

$$\Gamma_k = \int d^d x \sqrt{g}\, F(R) + S_{\rm gf} + S_{\rm gh}. \tag{2.19}$$

The expansion of $F(R)$ in powers of the scalar curvature R yields back the Einstein-Hilbert approximation when truncating after the linear term:

$$F(R) = \frac{\Lambda_k}{8\,\pi\,G_k} - \frac{R}{16\,\pi\,G_k} + \mathcal{O}(R^2). \tag{2.20}$$

The running cosmological constant Λ_k and the running Newton's constant G_k are the only couplings that are retained in this approximation. For our purpose we will do an expansion of $F(R)$ retaining N couplings

$$F(R) = \sum_{i=0}^{N-1} \tilde{\lambda}_i(k)\, R^i. \tag{2.21}$$

Comparison with (2.20) gives the translation between the two notations for $N = 2$:

$$\Lambda_k = -\frac{\tilde{\lambda}_0}{2\,\tilde{\lambda}_1}, \tag{2.22}$$

$$G_k = -\frac{1}{16\,\pi\,\tilde{\lambda}_1}. \tag{2.23}$$

We follow [34] for the derivation of the flow equation in d dimensions. Later we will set $d = 4$ to obtain explicit results in a classical dimensional setup without any extra-dimensions.

For our purpose, differentiating between powers of R in the flow, it suffices to assume a spherically symmetric background metric $\bar{g}_{\mu\nu}$. It is important to note that such a background cannot discriminate between tensor structures of the Riemann tensor and powers of the Ricci scalar of the same mass dimension. In principle any diffemorphism-invariant operator can be generated through the flow equation (2.18) dynamically along the flow. The choice of a spherically symmetric background projects all those Riemannian operators back onto their corresponding power of the Ricci scalar. The viability of such a procedure can be assessed by comparing it to more complicated setups where further operator defferentiation is retained. These studies [33, 99, 101, 102] indicate that the qualitative behaviour of the scalar operators is not altered.

The spherical symmetry leads to simplifed expression for the Riemann and Ricci tensor

of the background, as they become proportional to the Ricciscalar:

$$\bar{R}_{\mu\nu\rho\sigma} = \frac{\bar{R}}{d\,(d-1)}\,\left(\bar{g}_{\mu\rho}\,\bar{g}_{\nu\sigma} - \bar{g}_{\mu\sigma}\,\bar{g}_{\nu\rho}\right), \tag{2.24}$$

$$\bar{R}_{\mu\nu} = \bar{g}_{\mu\nu}\,\frac{\bar{R}}{d}. \tag{2.25}$$

The metric fluctuations $h_{\mu\nu} = g_{\mu\nu} - \bar{g}_{\mu\nu}$ are split up according to [106] into a transverse-traceless decomposition:

$$h_{\mu\nu} = h^T_{\mu\nu} + \bar{\nabla}_\mu\,\xi_\nu + \bar{\nabla}_\nu\,\xi_\mu + \bar{\nabla}_\mu\,\bar{\nabla}_\nu\,\sigma - \frac{1}{d}\,\bar{g}_{\mu\nu}\,\bar{\nabla}^2\,\sigma + \frac{1}{d}\,\bar{g}_{\mu\nu}\,h \tag{2.26}$$

$$h^T_{\mu\nu} = h^T_{\nu\mu} \tag{2.27}$$

$$h^{T\,\mu}_{\ \ \mu} = 0 \tag{2.28}$$

$$\bar{\nabla}_\nu\,h^{T\,\nu}_{\ \ \mu} = 0 \tag{2.29}$$

$$\bar{\nabla}_\mu\,\xi_\mu = 0 \tag{2.30}$$

The lowest two modes of σ and the lowest mode of ξ_μ are unphysical and will be excluded from the trace. The ghosts can be split up in transverse and scalar modes:

$$C_\mu = C^T_\mu + \bar{\nabla}_\mu\,\eta \tag{2.31}$$

$$\bar{C}_\mu = \bar{C}^T_\mu + \bar{\nabla}_\mu\,\bar{\eta} \tag{2.32}$$

$$b_\mu = b^T_\mu + \bar{\nabla}_\mu\,\theta \tag{2.33}$$

The lowest two mode of the scalar fields $\eta, \bar{\eta}$ and θ, and the lowest mode of the transverse vectors $C^T_\mu, \bar{C}^T_\mu$ and b^T_μ are unphysical and have to be excluded [34].

The decomposition of the fluctuation metric and the ghosts leads to a change of variables in the functional measure. The accompanying functional determinants can be re-expressed as an additional term in the bare action that originates from these variable transformations S_{trans}. The additional fields being introduced are anti-commuting complex scalars $\lambda, \bar{\lambda}$, a commuting real scalar ω, anti-commuting complex vectors $c^T, \bar{c}^T$, commuting real transverse vectors ζ^T, commuting complex scalars $s, \bar{s}$, anti-commuting complex scalars $\psi, \bar{\psi}$ and a commuting real scalar w. The transformation part of the action reads

$$\begin{aligned} S_{\text{trans}} = &\int d^dx\,\sqrt{\bar{g}}\,\left(\bar{\lambda}\,\mathcal{M}_\sigma\,\lambda + \omega\,\mathcal{M}_\sigma\,\omega + \bar{c}^T_\mu\,\mathcal{M}^{\mu\nu}_\xi\,c^T_\nu + \zeta^T_\mu\,\mathcal{M}^{\mu\nu}_\xi\,\zeta^T_\nu\right) \\ &+ \int d^dx\,\sqrt{\bar{g}}\,\left(\bar{s}\,\mathcal{M}_\eta\,s + \bar{\psi}\,\mathcal{M}_\theta\,\psi + w\,\mathcal{M}_\theta\,w\right) \end{aligned} \tag{2.34}$$

with the Jacobians from the transformation $\mathcal{M}_\varphi$

$$\mathcal{M}_\sigma = \left[\left(1 - \frac{1}{d}\right) \bar{\nabla}^2 \bar{\nabla}^2 + \frac{\bar{R}}{d} \bar{\nabla}^2\right]'' \tag{2.35}$$

$$\mathcal{M}_\xi = -2\,\bar{g}^{\mu\nu} \left[\bar{\nabla}^2 + \frac{\bar{R}}{d}\right]' \tag{2.36}$$

$$\mathcal{M}_\eta = \mathcal{M}_\theta = \left[-\bar{\nabla}^2\right]'' \tag{2.37}$$

where the number of primes indicates the number of lowest modes that have to be excluded from the trace. That number is inherited from the fields in the transformation.
The whole set of fields thereby becomes

$$\varphi = \left\{h^T, \xi, \sigma, h, C^T, \bar{C}^T, \eta, \bar{\eta}, b^T, \theta, \lambda, \bar{\lambda}, \omega, c^T, \bar{c}^T, \zeta^T, s, \bar{s}, \psi, \bar{\psi}, w\right\} \tag{2.38}$$

where every φ has a corresponding expectation value ϕ. The bare action S_{bare} consists of four terms:

$$S_{\text{bare}} = S + S_{\text{gf}} + S_{\text{gh}} + S_{\text{trans}}. \tag{2.39}$$

The gauge fixing, the ghosts and the transformation fields are treated classically, meaning that we approximate their Hessians of the effective average action $\Gamma_k^{(2)}$ simply by the Hessians of the classical action $S^{(2)}$.

2.4.1 Gauge fixing and ghosts

The gauge fixing term S_{gf} has the structure

$$S_{\text{gf}} = \frac{1}{2} \int d^d x\, F^\mu\, G_{\mu\nu}\, F^\nu, \tag{2.40}$$

where $F_\mu = l_\mu$ is the actual gauge fixing condition and $G_{\mu\nu}$ comes from performing a Gaussian functional integral over the functions l_μ centered around $l_\mu \equiv 0$ to smear out the delta distribution.
We choose a gauge fixing condition $F_\mu = 0$, which is linear in the full metric $\gamma_{\mu\nu}$, such that it simplifies to only act on the fluctuation part $F_\mu = \mathcal{F}_\mu^{\alpha\beta}\,\gamma_{\alpha\beta} = \mathcal{F}_\mu^{\alpha\beta}\,h_{\alpha\beta}$. We employ

$$\mathcal{F}_\mu^{\alpha\beta} = \delta_\mu^\beta\,\bar{\nabla}^\alpha - \frac{1+\rho}{d}\bar{g}^{\alpha\beta}\,\bar{\nabla}_\mu, \tag{2.41}$$

where ρ is a dimensionless parameter and thereby classifies a family of gauges.
The choice $\rho = \frac{d}{2} - 1$ is called harmonic gauge. We choose the so-called geometric gauge $\rho = 0$, as it simplifies our flow equation compared to the harmonic gauge [99].
The Gaussian tensor introduces two dimensionful gauge parameters α and β:

$$G_{\mu\nu} = \sqrt{\bar{g}}\bar{g}^{\mu\nu}\,\left(\alpha + \beta\,\bar{\nabla}^2\right). \tag{2.42}$$

Thereby the full gauge fixing term reads explicitly

$$S_{\rm gf} = \frac{1}{2}\int d^dx\,\sqrt{\bar{g}}\left[\alpha\left((\bar{\nabla}^\sigma\,h_{\sigma\mu})(\bar{\nabla}^\lambda\,h^\mu_\lambda) - \left(\frac{1+\rho}{d}\right)^2 h\bar{\nabla}^2\,h + \frac{2\,(1+\rho)}{d}\,h\,\bar{\nabla}_\mu\,\bar{\nabla}^\lambda\,h^\mu_\lambda\right)\right.$$
$$\left.+\beta\left((\bar{\nabla}^\sigma\,h_{\sigma\mu})\,\nabla^2\,(\bar{\nabla}^\lambda\,h^\mu_\lambda) - \left(\frac{1+\rho}{d}\right)^2 h\,\nabla_\mu\,\bar{\nabla}^2\,\nabla^\mu\,h + \frac{2\,(1+\rho)}{d}\,h\,\bar{\nabla}^\mu\,\nabla^2\,\bar{\nabla}^\lambda\,h_{\lambda\mu}\right)\right]. \tag{2.43}$$

The ghost term has the structure

$$S_{\rm gh} = \int d^dx\,\sqrt{\bar{g}}\,\bar{C}_\mu\,\bar{g}^{\mu\lambda}\,(\alpha+\beta\,\bar{\nabla}^2)\,M^\nu_\lambda\,C_\nu + \frac{1}{2}\int d^dx\,\sqrt{\bar{g}}\,b_\mu\,\bar{g}^{\mu\nu}\,(\alpha+\beta\,\bar{\nabla}^2)\,b_\nu, \tag{2.44}$$

where the Fadeev-Popov operator $M_{\mu\nu}$ is given as

$$\bar{g}^{\alpha\gamma}\,\bar{\nabla}_\gamma\,(\gamma_{\mu\nu}\,\nabla_\alpha + \gamma\alpha\nu\,\nabla_\mu) - \frac{2\,(1+\rho)}{d}\,\bar{g}^{\alpha\beta}\,\bar{\nabla}_\mu(\gamma_{\nu\beta}\,\nabla_\alpha). \tag{2.45}$$

Three gauge parameters α, β and ρ are retained which in general could be scale-dependent. In order to remove the running, a gauge needs to be chosen where $G_{\mu\nu} \to \infty$. Here, we choose $\alpha = \infty$ and $\beta = 0$ together with $\rho = 0$ [99]. This choice simplifes the flow equation drastically because it removes any mixing terms of σ and h and also only leaves the traces of h^T and h dependent of the function $F_k(R)$.

2.4.2 Second variation of Γ_k

The second variation of Γ_k is computed and afterwards it is evaluated on the spherical background $g_{\mu\nu} = \bar{g}_{\mu\nu}$. As a shorthand the bars of background quantities are now dropped. Due to the identification there is no ambiguity in this shorthand notation:

$$\frac{\delta^2}{\delta\phi_i\,\delta\phi_j}\,\Gamma_k \equiv \Gamma^{(2)}_{\phi_i\,\phi_j}\,\sqrt{g}\,\delta(x-y). \tag{2.46}$$

The Hessians $\Gamma^{(2)}_{\phi_i\,\phi_j}$ are usually diagonal, except for a mixing term for the expectation value of the σ and h fields. The gravitational Hessians are

$$\Gamma^{(2)}_{h^T h^T} = -\frac{1}{2}\,F(R) + F'(R)\,\left(\frac{1}{2}\,\nabla^2 + \frac{R\,(d-2)}{d\,(d-1)}\right) \tag{2.47}$$

$$\begin{aligned}\Gamma^{(2)}_{\xi\xi} = {} & F(R)\,\left(\nabla^2 + \frac{R'}{d\,F}(R)\,\left(\frac{2\,R}{d}\,\nabla^2 + \frac{2\,R^2}{d^2}\right) + \alpha\,\left(\nabla^4 + \frac{2\,R}{d}\,\nabla^2 + \frac{R^2}{d^2}\right)\right. \\ & \left. +\beta\,\left(\nabla^6 + \frac{2\,R}{d}\,\nabla^4 + \frac{R^2}{d^2}\,\nabla^2\right)\right)\end{aligned} \tag{2.48}$$

$$\begin{aligned}\Gamma^{(2)}_{\sigma\sigma} = {} & -\frac{1}{2}\,F(R)\,\left(\frac{d-1}{2}\,\nabla^4 + \frac{R}{d}\,\nabla^2\right) + F'(R)\,\left(\frac{R^2}{d^2}\nabla^2 + \frac{R}{2\,d}\,\nabla^4 - \frac{(d-1)\,(d-2)}{2\,d^2}\,\nabla^6\right) \\ & + F''(R)\,\left(\frac{(d-1)^2}{d^2}\,\nabla^8 + \frac{2\,(d-1)\,R}{d^2}\,\nabla^6 + \frac{R^2}{d^2}\right) \\ & - \alpha\,\left(\frac{(d-1)^2}{d^2}\,\nabla^6 + \frac{2\,(d-1)\,R}{d^2}\,\nabla^4 + \frac{R^2}{d^2}\,\nabla^2\right) \\ & - \beta\,\left(\frac{R^3}{d^3}\,\nabla^2 + \frac{(3\,d-2)\,R^2}{d^3}\,\nabla^4 + \frac{(1-4\,d+3\,d^2)\,R}{d^3}\,\nabla^6 + \frac{(d-1)^2}{d^2}\,\nabla^8\right)\end{aligned} \tag{2.49}$$

$$\begin{aligned}\Gamma^{(2)}_{\sigma h} = {} & F'(R)\,\left(\frac{(d-1)\,(d-2)}{2\,d^2}\,\nabla^4 + \frac{d-2}{2\,d^2}\,\nabla^2\,R\right) \\ & - F''(R)\,\left(\frac{(d-1)^2}{d^2}\,\nabla^6 + \frac{2\,(d-1)\,R}{d^2}\,\nabla^4 + \frac{R^2}{d^2}\,\nabla^2\right) + \alpha\,\rho\,\left(\frac{d-1}{d^2}\,\nabla^4 + \frac{R}{d^2}\,\nabla^2\right) \\ & + \beta\,\rho\,\left(\frac{d-1}{d^2}\,\nabla^6 + \frac{(2\,d-1)\,R}{d^3}\,\nabla^4 + \frac{R^2}{d^3}\,\nabla^2\right)\end{aligned} \tag{2.50}$$

$$\begin{aligned}\Gamma^{(2)}_{hh} = {} & F(R)\,\frac{d-2}{4\,d} + F'(R)\,\left(-\frac{(d-2)\,R}{d^2} - \frac{(d-1)\,(d-2)}{2\,d^2}\,\nabla^2\right) \\ & + F''(R)\,\left(\frac{R^2}{d^2} + \frac{2\,(d-1)}{d^2}\,\nabla^2\,R + \frac{(d-1)^2}{d^2}\,\nabla^4\right) \\ & - \frac{\rho^2}{d^2}\,\left(\alpha\,\nabla^2 + \beta\,\left(\nabla^4 + \nabla^2\,\frac{R}{d}\right)\right).\end{aligned} \tag{2.51}$$

The ghost Hessians are

$$\Gamma^{(2)}_{\bar{C}^T C^T} = \left(\alpha + \beta\,\nabla^2\right)\,\left(\nabla^2 + \frac{R}{d}\right) \tag{2.52}$$

$$\Gamma^{(2)}_{b^T b^T} = \alpha + \beta\,\nabla^2 \tag{2.53}$$

$$\Gamma^{(2)}_{\bar{\eta}\eta} = \left(\alpha + \beta\,\left(\nabla^2 + \frac{R}{d}\right)\right)\,\left(\frac{2\,(1+\rho)}{d}\nabla^4 - 2\,\nabla^4 - \frac{2\,R}{d}\,\nabla^2\right) \tag{2.54}$$

$$\Gamma^{(2)}_{\theta\theta} = -\left(\alpha + \beta\,\left(\nabla^2 + \frac{R}{d}\right)\right)\,\nabla^2. \tag{2.55}$$

The transformation field Hessians are

$$\Gamma^{(2)}_{\bar{c}^T c^T} = -2\left(\nabla^2 + \frac{R}{d}\right) \tag{2.56}$$

$$\Gamma^{(2)}_{\zeta^T \zeta^T} = -4\left(\nabla^2 + \frac{R}{d}\right) \tag{2.57}$$

$$\Gamma^{(2)}_{\bar{\lambda}\lambda} = \left(1 - \frac{1}{d}\right)\nabla^4 + \frac{R}{d}\nabla^2 \tag{2.58}$$

$$\Gamma^{(2)}_{\omega\omega} = 2\left(\left(1 - \frac{1}{d}\right)\nabla^4 + \frac{R}{d}\nabla^2\right) \tag{2.59}$$

$$\Gamma^{(2)}_{\bar{s}s} = \Gamma^{(2)}_{\bar{\psi}\psi} = \Gamma^{(2)}_{ww} = -\nabla^2. \tag{2.60}$$

All these second variations are the basis to compute the RHS of the flow equation (2.18) in Section 2.4.3.

2.4.3 Regulators

The regulator $\mathcal{R}_k$ is a part of the full inverse propagator $\tilde{\Gamma}^{(2)}_k = \Gamma^{(2)}_k + \mathcal{R}_k$. The second variation $\Gamma^{(2)}_k(\Delta)$ is viewed as dependent on a differential operator Δ:

$$\Gamma^{(2)}_k = \sum_n \mathcal{A}_n \Delta^n \tag{2.61}$$

The operator Δ has the general structure

$$\Delta = -\nabla^2 + E \tag{2.62}$$

with a potential term E. The potential term classifies the regulator. It can vanish (type I), depend on the scalar curvature R (type II) or can depend on the Ricci scalar R and the couplings (type III) [99]. We choose the regulator in such a way that it leads to the replacement

$$\tilde{\Gamma}^{(2)}_k = \Gamma^{(2)}_k(\Delta \to \Delta + R_k(\Delta)) \tag{2.63}$$

with the regulator shape function R_k. Thereby, the choice of Δ directly influences the way in which the IR modes are regulated. In contrast to [39, 40], we employ type I and type II regulators in order to improve the properties of the flow (cf. Section 3.1).
From condition (2.63) together with the general form of $\Gamma^{(2)}_k$ (2.61), we can write down the full inverse propagator

$$\Gamma^{(2)}_k + \mathcal{R}_k = \sum_n \mathcal{A}_n \left(\Delta + R_k\right)^n. \tag{2.64}$$

Using (2.64), we can solve for the full regulator term

$$\mathcal{R}_k = \sum_n \mathcal{A}_n \left(\left(\Delta + R_k\right)^n - \Delta^n\right). \tag{2.65}$$

The right-hand-side of the flow equation (2.18) also requires the logarithmic derivative $\partial_t \equiv k\,\partial_k$ of the regulator $\mathcal{R}_k$, which can be expressed using (2.65) as

$$\partial_t \mathcal{R}_k = \sum_n \left(\partial_t \mathcal{A}_n \left((\Delta + R_k)^n - \Delta^n\right) + \mathcal{A}_n\, n\,(\Delta + R_k)^{n-1}\,\partial_t R_k\right) \tag{2.66}$$

Now we can write the full flow equation with the traces on the right-hand-side:

$$\begin{aligned}
\partial_t \Gamma_k &= \mathcal{S}^{\text{gravity}} \\
&= \frac{1}{2}\,\mathrm{Tr}\left[\frac{\partial_t \mathcal{R}_k^{h^T h^T}}{\Gamma^{(2)}_{h^T h^T} + \mathcal{R}_k^{h^T h^T}}\right] + \frac{1}{2}\,\mathrm{Tr}'\left[\frac{\partial_t \mathcal{R}_k^{\xi\xi}}{\Gamma^{(2)}_{\xi\xi} + \mathcal{R}_k^{\xi}}\right] + \frac{1}{2}\,\mathrm{Tr}''\left[\frac{\partial_t \mathcal{R}_k^{\omega\omega}}{\Gamma^{(2)}_{\omega\omega} + \mathcal{R}_k^{\omega\omega}}\right] \\
&+ \frac{1}{2}\,\mathrm{Tr}'\left[\frac{\partial_t \mathcal{R}_k^{\zeta^T \zeta^T}}{\Gamma^{(2)}_{\zeta^T h^T} + \mathcal{R}_k^{\zeta^T \zeta^T}}\right] + \mathrm{Tr}''\left[\frac{\partial_t \mathcal{R}_k^{\bar{s}s}}{\Gamma^{(2)}_{\bar{s}s} + \mathcal{R}_k^{\bar{s}s}}\right] - \mathrm{Tr}''\left[\frac{\partial_t \mathcal{R}_k^{\bar{\lambda}\lambda}}{\Gamma^{(2)}_{\bar{\lambda}\lambda} + \mathcal{R}_k^{\bar{\lambda}\lambda}}\right] \\
&- \mathrm{Tr}''\left[\frac{\partial_t \mathcal{R}_k^{\bar{\eta}\eta}}{\Gamma^{(2)}_{\bar{\eta}\eta} + \mathcal{R}_k^{\bar{\eta}\eta}}\right] - \mathrm{Tr}'\left[\frac{\partial_t \mathcal{R}_k^{\bar{c}^T c^T}}{\Gamma^{(2)}_{\bar{c}^T c^T} + \mathcal{R}_k^{\bar{c}^T c^T}}\right] - \mathrm{Tr}'\left[\frac{\partial_t \mathcal{R}_k^{\bar{C}^T C^T}}{\Gamma^{(2)}_{\bar{C}^T C^T} + \mathcal{R}_k^{\bar{C}^T C^T}}\right] \\
&+ \frac{1}{2}\,\mathrm{Tr}''\left[\left(\tilde{\Gamma}^{(2)}_{hh}\,\tilde{\Gamma}^{(2)}_{\sigma\sigma} - \tilde{\Gamma}^{(2)}_{\sigma h}\,\tilde{\Gamma}^{(2)}_{\sigma h}\right)^{-1}\left(\tilde{\Gamma}^{(2)}_{hh}\,\partial_t \mathcal{R}_k^{\sigma\sigma} + \tilde{\Gamma}^{(2)}_{\sigma\sigma}\,\partial_t \mathcal{R}_k^{hh} - 2\,\tilde{\Gamma}^{(2)}_{\sigma h}\,\partial_t \mathcal{R}_k^{\sigma h}\right)\right] \\
&+ \frac{1}{2}\sum_{l=0}^{1} D_{l,0}\,\frac{\partial_t \mathcal{R}_k^{hh}(\lambda_{l,0})}{\Gamma^{(2)}_{hh}(\lambda_{l,0}) + \mathcal{R}_k^{hh}(\lambda_{l,0})} + \frac{1}{2}\,\mathrm{Tr}'\left[\frac{\partial_t \mathcal{R}_k^{b^T b^T}}{\Gamma^{(2)}_{b^T b^T} + \mathcal{R}_k^{b^T b^T}}\right] \\
&+ \frac{1}{2}\,\mathrm{Tr}''\left[\frac{\partial_t \mathcal{R}_k^{\theta\theta}}{\Gamma^{(2)}_{\theta\theta} + \mathcal{R}_k^{\theta\theta}}\right] - \mathrm{Tr}''\left[\frac{\partial_t \mathcal{R}_k^{\bar{\psi}\psi}}{\Gamma^{(2)}_{\bar{\psi}\psi} + \mathcal{R}_k^{\bar{\psi}\psi}}\right] + \frac{1}{2}\,\mathrm{Tr}''\left[\frac{\partial_t \mathcal{R}_k^{ww}}{\Gamma^{(2)}_{ww} + \mathcal{R}_k^{ww}}\right].
\end{aligned} \tag{2.67}$$

Due to the mixing of the σ and h modes, the full inverse propagator there corresponds to a matrix inversion. Because the lowest two modes of σ have to be excluded and there is no exclusion for h, we explicitly include the lowest two modes of h into the right-hand-side. The scalar eigenvalues of Δ are denoted by $\lambda_{l,0}$ with corresponding multiplicities $D_{l,0}$. Since we employ type I and type II cutoffs in (2.67), as we will explain in detail later (cf. Section 3.1), in principle each trace should be thought of as having their own individual Δ.

2.4.4 Trace evaluation

When evaluating the traces in the flow equation (2.67), we encounter in general a function W of a differential operator Δ:

$$\mathrm{Tr}\left[W(\Delta)\right] \tag{2.68}$$

In principle these traces could be computed with the eigenvalue spectrum of Δ, including the multiplicities of each eigenvalue. It turns out that it is more practical to utilise heat kernel methods for the trace computation. Therefore we have to reexpress $W(\Delta)$ via its

anti-Laplace transform $\tilde{W}(\tau)$

$$W(\Delta) = \int_0^\infty d\tau \, \exp(-\tau\,\Delta)\,\tilde{W}(\tau), \tag{2.69}$$

where the exponential $\exp(-\tau\,\Delta)$ is called the heat kernel. It has an asymptotic expansion which is used to expand the trace:

$$\begin{aligned}\mathrm{Tr}\,[W(\Delta)] &= \int_0^\infty d\tau\,\mathrm{Tr}\,[\exp(-\tau\,\Delta)]\;\tilde{W}(\tau),\\ &= V_d \sum_{n=0}^{\infty} b_{2\,n}\,Q_{d/2-n}(W).\end{aligned} \tag{2.70}$$

The b_{2n} are called heat-kernel coefficients and can be calculated for all the relevant fields (scalars, transverse vectors, transverse-traceless tensors) using recursion relations [107]. As we employ a spherical background, the heat kernel coefficients will be proportional to powers of the Ricci scalar R. The volume of the sphere V_d is given as

$$V_d = (4\,\pi)^{d/2}\,\frac{\Gamma(d/2)}{\Gamma(d)}\,\left(\frac{d\,(d-1)}{R}\right)^{d/2}. \tag{2.71}$$

The Q-functions encode the shape of W:

$$Q_m(W) = \int_0^\infty d\tau\,\tau^{-m}\,\tilde{W}(\tau). \tag{2.72}$$

The expression for Q_m can be related back to W instead of its anti-Laplace transform $\tilde{W}(\tau)$. Since we will later take $d = 4$, it suffices to consider integer values of m (cf. (2.70)):

$$Q_m(W) = \begin{cases} \frac{1}{\Gamma(m)} \int_0^\infty dz\,z^{m-1}\,W(z) & m > 0 \\ (-1)^{-m}\,W^{(-m)}(0) & m \leq 0 \end{cases}. \tag{2.73}$$

Due to the regulator implementation (cf. Section 2.4.3), the general shape function in our case is

$$W(\Delta) = \frac{1}{2}\,\frac{\sum_n \left(\partial_t \mathcal{A}_n\,((\Delta+R_k)^n - \Delta^n) + \mathcal{A}_n\,n\,(\Delta+R_k)^{n-1}\,\partial_t R_k\right)}{\sum_n \mathcal{A}_n\,(\Delta+R_k)^n}. \tag{2.74}$$

We choose the optimised cutoff [69, 70] for the regulator shape function R_k:

$$R_k(z) = (k^2 - z)\,\theta(k^2 - z), \tag{2.75}$$

and get

$$Q_m(W) = \begin{cases} \frac{1}{2\,\Gamma(m+1)}\,\frac{\sum_n k^{2n+2m}\left(\frac{n}{n+m}\,\partial_t\mathcal{A}_n + 2\,n\,\mathcal{A}_n\right)}{\sum_n \mathcal{A}_n\,k^{2n}} & m > 0 \\ \frac{1}{2}\,\frac{\sum_{n=1} k^{2n}(\partial_t\mathcal{A}_n + 2\,n\,\mathcal{A}_n)}{\sum_n \mathcal{A}_n\,k^{2n}} & m = 0 \\ \frac{(-1)^{-m+1}}{2}\,\frac{(-m)!\,\partial_t\mathcal{A}_{-m}}{\sum_n \mathcal{A}_n\,k^{2n}} & m \leq 0 \end{cases}. \tag{2.76}$$

Since for our particular gauge choice, all $\mathcal{A}_m = 0$ for $m < -2$ are zero, the heat kernel expansion naturally truncates without the imposition of any further approximation.

2.5 Beta functions and fixed points

In this section we introduce the basic concepts and notation to analyse the flow equation in the UV limit.

So far we have dealt with dimensionful quantities, such as couplings $\tilde{\lambda}_i$ (2.21), the Ricci scalar R to build up a polynomial $F(R)$. We will now switch to dimensionless quantities by rescaling with the RG scale k for further analysis. This will make the search for fixed points easier.

We define:

$$v_d \equiv k^d V_d \tag{2.77}$$

$$\lambda_i \equiv 16\,\pi\, k^{2\,i-d}\tilde{\lambda}_i \tag{2.78}$$

$$\rho \equiv k^{-2}\, R \tag{2.79}$$

$$f(\rho) \equiv 16\,\pi\, k^{-d}\, F(R). \tag{2.80}$$

The conventional factor of $16\,\pi$ generates a very simple relationship between the coupling λ_1 and the dimensionless Newton's constant (cf. (2.20)) The dimensionless Ricci scalar ρ is not to be confused with the gauge parameter ρ. In a context where there might be an ambiguity, we will denote the gauge parameter by $\rho = \rho_{\text{gauge}}$.

In dimensionless notation the left hand side of the flow equation has the structure

$$\partial_t f + d\, f - 2\,\rho\, f'. \tag{2.81}$$

We will later observe (cf. (3.5)) that the right hand side of the flow equation $I[f]$ for the mentioned dimensionality and gauge choices has homogenity degree 0 in f. Therefore any rescaling of f with a constant, merely leads to an overall constant factor on the left hand side of the flow equation.

The right hand side of the flow equation is given through (2.67) and will be explicitly calculated in Section 3.1. We review the flow equation and key results of [39, 40, 66, 67] in Section 2.6 in order to point out the differences to our treatment in Section 3.1.

We examine the flow equation (2.67) for its compatibility with the asymptotic safety scenario. For this to be realised, the effective average action has to approach a fixed point

action in the UV limit $k \to \infty$. This means that the dimensionless couplings $\lambda_i = k^{-d_i}\,\tilde{\lambda}_i$ exhibit a vanishing beta function $\beta_i = k\,\partial_k\,\lambda_i$, where $d_i = 2\,i - 4$ denotes the canonical mass dimension of $\tilde{\lambda}_i$. This implies that close to the UV- fixed-point the beta functions β_i are well-described by the linearised flow around the fixed points λ_i^*:

$$\beta_i = \sum_j M_{ij}\,(\lambda_j - \lambda_j^*) + \text{subleading}, \tag{2.82}$$

where $M_{ij} = \partial\beta_i/\partial\lambda_j|_*$ is called the stability matrix. The eigenvalues $-\theta_n$ and eigenvectors $V_{n,i}$ of M_{ij} determine the UV properties of the flow which has the form

$$\lambda_i - \lambda_i^* = \sum_n C_n V_{n,i} e^{-\theta_n t} + \text{subleading}. \tag{2.83}$$

A positive eigenvalue (real part) $-\theta_n$ corresponds to an irrelevant direction which is not part of the asymptotic safety scenario; their coefficients C_n are set to zero. A negative eigenvalue (real part) $-\theta_n$ corresponds to a relevant direction. Trajectories in these directions are renormalisable since they are forced into the fixed point as $k \to \infty$. The asymptotic safety scenario includes all attractive directions. If their number turns out to be finite, the theory is governed by a finite number of couplings and therefore predictive.

2.6 Previous $f(R)$ results

Polynomial $f(R)$ quantum gravity was studied up until order 6 [34, 100] and order 8 [99] in the Ricci scalar. The study in [108] pushed it to order 10, but did not feature an analysis of the critical behaviour at the fixed point. A global analysis of solutions $f(R)$ to the flow presented in [109] was undertaken in [110, 111]. In this section we review the flow equation and results presented in [39, 40, 66, 67] in more detail to highlight similarities and differences in our treatment (cf. Section 3.1).

The derivation of their flow equation follows the same conventions as presented in this chapter. The crucial difference is type of regulator used. They solely apply a type I regulator

$$\Delta = -\nabla^2 \tag{2.84}$$

on the right hand side of the flow equation (2.67). In contrast, we will employ a mixture of both type I and type II regulators. The treatment in [39, 40, 66, 67] leads to a flow equation of the form

$$\dot{f} - 2\,\rho\,f' + 4\,f = c\,I[f] = c\,\left(I_0[f] + I_1[f]\,\dot{f}' + I_2[f]\,\dot{f}''\right) \tag{2.85}$$

$$c = \frac{1}{24\,\pi} \tag{2.86}$$

A dot denotes a logarithmic derivative with respect to k, whereas a prime denotes a derivative with respect to ρ. The contributions to the right hand side $I[f]$ are given as:

$$I_0[f] = \frac{P_0^S}{D_0^S} + \frac{P_0^V}{D_0^V} + \frac{P_0^{S1}\, f' + P_0^{S2}\, f'' + P_0^{S3}\, f'''}{D^S} + \frac{P_0^{T1}\, f' + P_0^{T2}\, \rho\, f''}{D^T} \tag{2.87}$$

$$I_1[f] = \frac{P_1^S}{D^S} + \frac{P_1^T}{D^T} \tag{2.88}$$

$$I_2[f] = \frac{P_2^S}{D^S}. \tag{2.89}$$

The superscripts T (tensor), V (vector) and S (scalar) provide additional structural information about the type of field that generates the contribution P.
The denominators D (excluding D_0^S and D_0^V) are

$$D^S = 2\, f + (3 - 2\,\rho)\, f' + (3 - \rho)^2\, f'' \tag{2.90}$$

$$D^T = 3\, f - (\rho - 3)\, f' \tag{2.91}$$

The polynomials P_0 of $I_0[f]$ (excluding P_0^S and P_0^V) are

$$P_0^{S1} = \frac{37}{756}\,\rho^3 + \frac{29}{15}\,\rho^2 + 18\,\rho + 48 \tag{2.92}$$

$$P_0^{S2} = -\frac{37}{756}\,\rho^4 - \frac{29}{10}\,\rho^3 - \frac{121}{5}\,\rho^2 - 12\,\rho + 216 \tag{2.93}$$

$$P_0^{S3} = \frac{181}{1680}\,\rho^4 + \frac{29}{15}\,\rho^3 + \frac{91}{10}\,\rho^2 - 54 \tag{2.94}$$

$$P_0^{T1} = \frac{311}{756}\,\rho^3 - \frac{1}{3}\,\rho^2 - 90\,\rho + 240 \tag{2.95}$$

$$P_0^{T2} = -\frac{311}{756}\,\rho^3 + \frac{1}{6}\,\rho^2 + 30\,\rho - 60. \tag{2.96}$$

The polynomials P_1 of $I_1[f]$ are

$$P_1^S = \frac{37}{1512}\,\rho^3 + \frac{29}{60}\,\rho^2 + 3\,\rho + 6 \tag{2.97}$$

$$P_1^T = -\frac{181}{3360}\,\rho^4 - \frac{29}{30}\,\rho^3 - \frac{91}{20}\,\rho^2 + 27. \tag{2.98}$$

And finally the polynomial P_2 of $I_2[f]$ is

$$P_2^S = \frac{311}{1512}\,\rho^3 - \frac{1}{12}\,\rho^2 - 15\,\rho + 30. \tag{2.99}$$

The overall flow equation (2.85) has the same structure as our flow equation (3.5). The functions D^S, D^T, P_0^{S1}, P_0^{S2}, P_0^{S3}, P_0^{T1}, P_0^{T2}, P_1^S, P_1^T and P_2^S are the same functions as in our flow equation (cf. equations (3.10) to (3.21), excluding (3.12) and (3.13)). The difference lies in the explicit form of $I_0[f]$ which features two rational functions as f-

independent terms with

$$P_0^S = \frac{511}{30}\,\rho^2 - 12\,\rho - 36 \tag{2.100}$$

$$D_0^S = 3 - \rho \tag{2.101}$$

$$P_0^V = \frac{607}{15}\,\rho^2 - 24\,\rho - 144 \tag{2.102}$$

$$D_0^V = 4 - \rho. \tag{2.103}$$

This introduces two poles into the flow equation, namely at $\rho = 3$ from (2.101) and at $\rho = 4$ from (2.103). These poles potentially influence the physical properties of the flow and could limit the radius of convergence of a series expansion of $f(\rho)$. In our flow equation (3.5), the f-independent term is reduced to two polynomials via a different regulator choice (3.2) for certain modes. The denominators D_0^S and D_0^V are simply 1 and can be eliminated from our flow. The polynomials P_0^S and P_0^V are different function and given in (3.12) and (3.13).

The flow equation in [39, 40, 66, 67] has been analysed up to $N = 35$ in polynomial order. A stable fixed point pattern is found with three relevant directions. The irrelevant directions exhibit a behaviour very close to canonical scaling.

The polynomial expansion of $f(\rho)$ around $\rho = 0$ has a finite radius of convergence of [66]

$$\rho_c \approx 0.83 \pm 5\%. \tag{2.104}$$

This completes our summary of the tools necessary for our treatment of $f(R)$ gravity. In the next Chapter 3 we use those techniques to analyse a slightly different flow and push fixed point searches to even higher orders.

Chapter 3

Pure gravity in the $f(R)$ approximation

In this chapter we derive a flow equation for polynomial $f(R)$ gravity in four spacetime dimensions explicity, as outlined in Chapter 2. Our main motivation to introduce an improved flow for this template action of quantum gravity is the following:
It has been found in the past that the flow equation may develop poles for finite Ricci curvature at certain points in field space [39, 40, 66, 67]. One would expect for a fixed point solution to be finite for all real Ricci curvature values. In principle this can be achieved with the existing flows. But the occurrence of too many poles in the flow can lead to the absence of a globally defined fixed point solution [110]. The poles can be related to technical choices regarding the cutoff function. We exploit the freedom to choose a Wilsonian cutoff, in order to remove certain poles. The differential equation of the flow (cf. Section 2.6 equations (2.85) and (2.87)) develops poles in the dimensionless Ricci scalar ρ via D_0^S (2.101) and D_0^V (2.103). They have the location $\rho = 3$ and $\rho = 4$.
Our main achievement is an improved flow equation in which these explicit poles in the Ricci scalar are removed (cf. Section 3.1). We confirm and extend the picture of an interacting UV fixed point where higher order operators generate increasingly irrelevant directions.
For the analysis we developed and used a new code to efficiently compute the fixed point algebraically to the previously inaccessible order $N_{\max} = 71$. We numerically extend these findings up to $N_{\max} = 1001$.

3.1 Improved functional flow

We will now explicitly evaluate the terms on the right hand side of the flow equation in (2.67). First we state the second variations $\Gamma^{(2)}_{\phi_i\phi_i}$ with the cutoff choice $\Delta_{\phi_i\phi_i}$ and then the trace. The cutoff is always chosen to remove explicit poles in ρ for the traces compared to [39, 40, 66, 67]. The fields obtaining a different treatment are the gravitational scalar mode σ, the ghost scalar mode η, the auxiliary scalar modes λ and ω and the gravitational vector ξ. We will thereby be sensitive to potential effects of the system due to the (absence of) poles and determine their physical significance.

The different contributions to the right hand side of the flow equation are given explicitly in Appendix A. In this particular gauge, there are no contributions from the ghost b and all associated fields, namely b^T, θ, ψ, w.

The prerequisite of removing the explicts poles in ρ leads to type II regulator for the gravitational vector mode ξ (A.4) and to some scalar modes being regularised in a more involved manner (σ (A.7) and (A.8), η (A.17) and (A.18), λ (A.27) and (A.28), ω (A.34) and (A.35)). The key observation here is that the Hessians have a generic product structure

$$\Gamma^{(2)}_{xx} = c\,\left(-\nabla^2\right)\,\left(-\nabla^2-\frac{\rho}{3}\right)^n, \tag{3.1}$$

where c is a constant prefactor and the power n in our case takes integer values 1 and 2. We now define the regulator $\mathcal{R}^{xx}_k$ implicitly via the inverse propagator

$$\Gamma^{(2)}_{xx}+\mathcal{R}^{xx}_k = c\,\left[-\nabla^2+R_k(-\nabla^2)\right]\,\left[-\nabla^2-\frac{\rho}{3}+R_k(-\nabla^2-\frac{\rho}{3})\right]^n, \tag{3.2}$$

in which the same shape function R_k is used with two different arguments. Thereby the trace $\mathcal{S}_{xx}$ can be expressed as the sum of two traces:

$$\mathcal{S}_{xx} = \frac{1}{2}\,\mathrm{Tr}''\left[\frac{\partial_t\mathcal{R}^{xx}_k}{\Gamma^{(2)}_{xx}+\mathcal{R}^{xx}_k}\right] \tag{3.3}$$

$$= \frac{1}{2}\,\mathrm{Tr}''\left[\frac{\partial_t\,R_k(-\nabla^2)}{-\nabla^2+R_k(-\nabla^2)}\right] + \frac{1}{2}\,\mathrm{Tr}''\left[\frac{n\,\partial_t\,R_k(-\nabla^2-\frac{\rho}{3})}{-\nabla^2-\frac{\rho}{3}+R_k(-\nabla^2-\frac{\rho}{3})}\right]. \tag{3.4}$$

This ensures that the traces in question do not contribute any poles in ρ to the flow equation.

The full flow equation reads:

$$\dot{f}-2\,\rho\,f'+4\,f = c\,I[f] = c\,\left(I_0[f]+I_1[f]\,\dot{f}'+I_2[f]\,\dot{f}''\right) \tag{3.5}$$

$$c = \frac{1}{24\,\pi}. \tag{3.6}$$

A dot denotes a logarithmic derivative with respect to k, whereas a prime denotes a derivative with respect to ρ. The contributions to the right hand side $I[f]$ are given as:

$$I_0[f] = P_0^S + P_0^V + \frac{P_0^{S1}\, f' + P_0^{S2}\, f'' + P_0^{S3}\, f'''}{D^S} + \frac{P_0^{T1}\, f' + P_0^{T2}\, \rho\, f''}{D^T} \tag{3.7}$$

$$I_1[f] = \frac{P_1^S}{D^S} + \frac{P_1^T}{D^T} \tag{3.8}$$

$$I_2[f] = \frac{P_2^S}{D^S}. \tag{3.9}$$

The superscripts T (tensor), V (vector) and S (scalar) provide additional structural information about the type of field that generates the contribution P.

Please note again that the non-f-dependent contribution to I_0 consists just of two polynomials P_0^S and P_0^V and therefore does not contain poles in ρ, as in previous treatments (cf. Section 2.6). The denominators D are

$$D^S = 2\, f + (3 - 2\,\rho)\, f' + (3 - \rho)^2\, f'' \tag{3.10}$$

$$D^T = 3\, f - (\rho - 3)\, f'. \tag{3.11}$$

The polynomials P_0 of $I_0[f]$ are

$$P_0^S = \frac{271}{45}\,\rho^2 + -24\,\rho - 24 \tag{3.12}$$

$$P_0^V = \frac{191}{15}\,\rho^2 - 48\,\rho - 72 \tag{3.13}$$

$$P_0^{S1} = \frac{37}{756}\,\rho^3 + \frac{29}{15}\,\rho^2 + 18\,\rho + 48 \tag{3.14}$$

$$P_0^{S2} = -\frac{37}{756}\,\rho^4 - \frac{29}{10}\,\rho^3 - \frac{121}{5}\,\rho^2 - 12\,\rho + 216 \tag{3.15}$$

$$P_0^{S3} = \frac{181}{1680}\,\rho^4 + \frac{29}{15}\,\rho^3 + \frac{91}{10}\,\rho^2 - 54 \tag{3.16}$$

$$P_0^{T1} = \frac{311}{756}\,\rho^3 - \frac{1}{3}\,\rho^2 - 90\,\rho + 240 \tag{3.17}$$

$$P_0^{T2} = -\frac{311}{756}\,\rho^3 + \frac{1}{6}\,\rho^2 + 30\,\rho - 60. \tag{3.18}$$

The polynomials P_1 of $I_1[f]$ are

$$P_1^S = \frac{37}{1512}\,\rho^3 + \frac{29}{60}\,\rho^2 + 3\,\rho + 6 \tag{3.19}$$

$$P_1^T = -\frac{181}{3360}\,\rho^4 - \frac{29}{30}\,\rho^3 - \frac{91}{20}\,\rho^2 + 27. \tag{3.20}$$

And finally the polynomial P_2 of $I_2[f]$ is

$$P_2^S = \frac{311}{1512}\,\rho^3 - \frac{1}{12}\,\rho^2 - 15\,\rho + 30. \tag{3.21}$$

The explicit flow equation can now be analysed for fixed points and their critical behaviour (cf. Section 2.5) using the method presented in the following Section 3.2.

3.2 Bootstrap

The analysis of the flow equation (3.5) is carried out via a polynomial expansion of the function $f(\rho)$ around $\rho = 0$. The approximation is controlled by the highest power of ρ accounted for in the approximated flow.

The basic assumption behind this procedure is that all non-attractive couplings λ_i can be described by the weak-coupling limit, meaning that their critical behaviour at the fixed point is mainly described by their canonical mass dimension d_i and that any corrections due to interactions are small. The Gaussian scaling corresponds to an eigenvalue $-\theta_{G,i} = -d_i$. The corrections induced by a coupling are assumed to decrease with decreasing mass dimension d_i. Note that the mass dimensions are negative here. We cannot prove this assumption a priori, but it is consistent with the findings in [39, 40, 66, 67] tested up to polynomial order R^{34} which provides an a posteriori justification.
Since the so-far observed attractive directions in $f(R)$ theory appear in the R^2 approximation with no further directions appearing with the addition of higher order terms, the assumption motivates an iterative procedure of analysis: We study a polynomial gravitational effective action Γ_k that includes all powers of R up to a maximal order $N-1$, which includes N couplings, and therefore we approximate

$$f(\rho) \approx f^N(\rho) = \sum_{n=0}^{N-1} \lambda_n \rho^n. \tag{3.22}$$

For fixed N, the canonical mass dimension of the couplings λ_i is bounded by $d_i \geq -2(N-1)+4$. We can calculate the beta functions for a fixed N and analyse them for their fixed point properties, namely the number of attractive directions and the eigenvalues of the stability matrix. This procedure is then iterated by going from N to $N+1$. In each iteration one new coupling is accounted for that has a canonical mass dimension less than any other previously included coupling. We performed this analysis from $N = 2$ to $N = 71$ and thereby went significantly beyond the range of [39, 40, 66, 67].

At the heart of our subsequent calculation lies a recursion relation of the couplings at the fixed point. To obtain it, first we need to set all scale derivatives in (3.5) to 0. The fixed point equation then reads

$$4\, f(\rho) - 2\, \rho\, f'(\rho) = I_0[f] \tag{3.23}$$

with I_0 given in (3.7). This equation encodes all the information of the fixed point. In order to access it, the equation is rearranged such that we get rid of all denominators that

contain any ρ or f structure. We call this equation

$$A[f] \equiv D^S D^T \left(4 f(\rho) - 2\rho f'(\rho) - c I_0[f]\right) = 0. \tag{3.24}$$

Then we can take n derivatives with respect to ρ of the equation and evaluate it at $\rho = 0$. We observe that the resulting equation

$$A^{(n)}(f, f', \ldots, f^{(n+2)}) = 0 \tag{3.25}$$

depends in principle on all derivatives of f up to $f^{(n+2)}$. In particular it is linear in the highest derivative $f^{(n+2)}$. Therefore the equation can always be rearranged for this. Bearing in mind that $f^{(i)}(\rho = 0) = i!\,\lambda_i$ we obtain

$$\lambda_{n+2} = \tilde{X}_{n+2}(\lambda_0, \lambda_1, \ldots, \lambda_{n+1}). \tag{3.26}$$

Since there are also equations for λ_{n+1} down to λ_2, we can recursively simplify this equation to yield

$$\lambda_{n+2} = X_{n+2}(\lambda_0, \lambda_1). \tag{3.27}$$

This means that through the knowledge of the first two couplings at the fixed point, all other couplings in $f(\rho)$ are fixed. The challenge of this method is solving the recursion relation encoded in the functions $\tilde{X}_i$ to obtain X_i. A dedicated C++ program was developed to compute the X_i (cf. Section 3.3). The results are exact because the X_i can be expressed as rational functions in λ_0, λ_1 with integer coefficients. The efficiency and speed of this program makes it possible to go up to $N = 71$ and thereby double the order previously achieved [39, 40, 66, 67].

At a given approximation order N, we impose that the next two couplings, namely λ_N and λ_{N+1}, vanish:

$$\lambda_N = 0 = \lambda_{N+1}. \tag{3.28}$$

The boundary condition (3.28) fixes λ_0 and λ_1 and with them all other couplings at approximation order N. The condition (3.28) is solved using the functions X_N and X_{N+1} by numerically looking at the intersections of their nullclines. In a typical setup there are more than one intersection. The choice is made using consistency requirements.
Firstly the fixed point coordinates λ_0 and λ at the considered order should be close to the choice in the previous order. Secondly the fixed point coordinates should be stable over the orders. Sometimes there are solutions to the boundary condition that are close

to the fixed point coordinates from the previous order. But tracking this candidate over several orders shows that it is moving its location rapidly with the orders. Thirdly the critical behaviour should be close to the one of the previous order fixed point, in particular regarding the relevant eigenvalues. The combination of all of these three criteria allowed for a unique choice of a fixed point candidate among several other candidates that could be deemed spurious.

The boundary condition we impose is not unique. The choice of the boundary condition may influence the speed of coupling convergence over the approximation orders. It does not affect the coupling values in the limit $N \to \infty$.

The set of fixed point coordinates $\{\lambda_0, \ldots, \lambda_{N-1}\}$ at a given approximation order N is then used to analyse the fixed point for its scaling properties. The stability matrix $\mathcal{M}$ can be calculated from the flow equation (3.5). We define

$$B[f, \dot{f}] \equiv D^S \, D^T \, \left(\dot{f} - c \, I_1[f] \, \dot{f}' - c \, I_2[f] \, \dot{f}'' \right) \tag{3.29}$$

and use it to rewrite the flow equation in a way that gets rid of all denominators with a ρ or f structure:

$$A[f] + B[f, \dot{f}] = 0. \tag{3.30}$$

The term $B[f, \dot{f}]$ vanishes at the fixed point ($\dot{f}^{(i)} = 0$) and we would have equation (3.24) again. Then we take n derivatives with respect to ρ of this equation and evaluate at $\rho = 0$. This yields

$$A_n + \sum_{m=0}^{n+2} B_{nm} \, \beta_m = 0 \tag{3.31}$$

with $A_n = \partial_\rho^n A|_{\rho=0}$ and $\sum_{m=0}^{n+2} B_{nm} \, \beta_m = \partial_\rho^n B|_{\rho=0}$. Now we take the partial derivative with respect to coupling λ_j and evaluate at the fixed point

$$A^*_{nj} + B^*_{nm} M_{mj} = 0 \tag{3.32}$$

with $A^*_{nj} - \partial_{\lambda_j} A_n|_* \equiv \mathcal{A}$, $B^*_{nm} = B_{nm}|_* \equiv \mathcal{B}$ and $M_{mj} = \partial_{\lambda_j} \beta_m|_* \equiv \mathcal{M}$. Summation over double occurring indices is implied. This matrix equation can be solved for the stability matrix $\mathcal{M}$

$$\mathcal{M} = -\mathcal{B}^{-1} \cdot \mathcal{A} \tag{3.33}$$

The eigenvalues $-\theta$ of $\mathcal{M}$ are the negative critical exponents θ. The number of relevant directions should be finite in order to be compatible with the asymptotic safety conjecture. As a cross-check to the method of computing the stability matrix involving derivatives of the flow (3.32), we also employed an integral method a la [112], using orthogonal polynomials to project out the desired contributions. The results were found to be in complete agreement with (3.33).

3.3 Code

The main challenge on the technological side of systematically solving the fixed point equation (3.23), is finding solutions X_{n+2} (3.27) to the recursion relation (3.26).
The solutions are rational functions of the lowest two couplings λ_0 and λ_1:

$$\lambda_{n+2} = X_{n+2}(\lambda_0, \lambda_1) = \frac{P_{n+2}(\lambda_0, \lambda_1)}{Q_{n+2}(\lambda_0, \lambda_1)}, \tag{3.34}$$

where P and Q are polynomials. The terms $\tilde{X}_{n+2}$ are known from (3.25) have the structure

$$\lambda_{n+2} = \tilde{X}_{n+2}(\lambda_0, \cdots, \lambda_{n+1}) = \frac{\left(\sum_{i,j,k} a^{(3)}_{i,j,k}\, \lambda_i, \lambda_j\, \lambda_k\right) + \left(\sum_{i,j,k} a^{(2)}_{i,j}\, \lambda_i, \lambda_j\right) + \left(\sum_i a^{(1)}_i\, \lambda_i\right)}{\mathcal{D}_{n+2}(\lambda_0, \lambda_1)}, \tag{3.35}$$

where $\mathcal{D}_{n+2}$ is a polynomial that is at most quadratic in λ_0 and linear in λ_1. The summed over indices in (3.35) range from 0 to $n+1$. The coefficients a in (3.35) can be made integer by appropriate choice of the scaling factor c in the flow equations (3.5). Remember that a particular choice of c corresponds to a certain renormalisation of the couplings. Generally the coefficients do still depend on the number n of the coupling considered.

3.3.1 Algorithm

The designed *C++* program can solve any recursion relation that can be written as (3.35). The results P and Q are exact and contain no numerical approximation.

The recursion relation defined via $\lambda_{n+2} = \tilde{X}_{n+2}$ (3.26) can be solved by subsequently inserting the known λ_i into (3.35), starting at $n = 0$ and going up until the desired order. The denominators Q of the solution are determined by taking the denominators of the previously calculated λ_i and determining the smallest product possible that by multiplication makes the numerator in (3.35) a polynomial and multiplying it with the denominator

of(3.35). The numerator P of a particular solution is computed by carrying out the sums in the numerator of (3.35) explicitly and each part needs to be multiplied by the denominator Q of that solution, excluding the factor of $\mathcal{D}$. The computation of P is the limiting factor for solving this recursion relation because it needs the most operations.

3.3.2 Implementation

The polynomials P and Q of the solution are represented as connected lists with two indices, meaning that only non-zero coefficients are stored. This has two advantages. First, the allocated space for a polynomial is reduced, because otherwise a stored 0 takes up space as well. Second, the polynomial multiplication becomes faster since only non-trivial operations are carried out.

The polynomial coefficients of the solutions P and Q are large integers and will exceed the data range of any standard integer type as the recursion is carried out and polynomial coefficients are multiplied. Therefore we use a dynamical integer data type from the *GNU Multiple Precision Library* [113] that grows in size as the stored integer grows. Thereby always the exact result of an integer multiplication is stored and we obtain an exact solution to the recursion relation.

The algorithm can be parallelised due to the sum structure in the numerator of (3.35). The sums can be divided up into various subsums. Each subsum can be computed in a different thread and, once all are finished, they will be recombined to yield the full solution.
However, each subsum potentially requires knowledge of all the solutions λ_i of the previous orders. If all threads had shared access to one copy of the already computed solutions, clashes could occur where two threads try to access the same information during overlapping time intervals. This can be avoided either by introducing muticies that make threads wait while another thread is accessing a shared variable or by making full copies of the previous solutions for each individual thread. The first approach leads to slowed down computations as threads can become idle while they wait. The second approach does not have this problem but requires a substantial amount of memory that scales directly with the number of threads spawned. We employ the second approach as speed is paramount for us.
For the handling of parallel threads, the *boost Thread* library [114] is used.

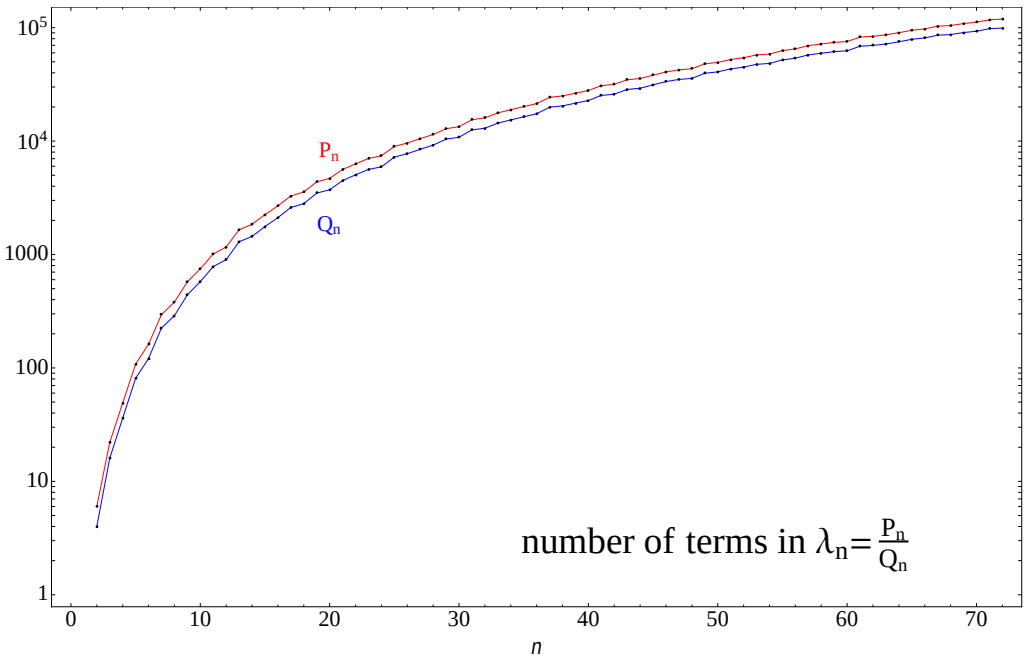

Figure 3.1: The number of non-vanishing monomials $\lambda_0^i \lambda_1^j$ in the polynomials P_n , Q_n is plotted against the index n of the corresponding coupling fixed point solution λ_n. The fixed point solutions grows in size with increasing order n.

3.3.3 Performance

The code was executed on the University of Sussex high performance cluster *apollo*. It solved the recursion relation up until λ_{72}. We used 40 threads in each iteration while focusing mainly on the splitting up of the sum in (3.35), featuring a product of three λs. Those required the most computational effort.

The computation took $\sim$ 46 days and used $\sim$ 959 days of CPU time, leading to an effective parallelisation factor of $\sim$ 20. The code allocated at most $\sim$ 100 GB of memory during its runtime at a single moment. The created output (files containing the Ps and Qs) has a size of $\sim$ 3.6 GB. In order to assess the size of the resulting polynomials P and Q, we provide a plot of the number of nonzero monomials in λ_n Figure 3.1 and a plot of the highest powers of λ_0 and λ_1 occuring in λ_n in Figure 3.2.

The output is loaded into *Mathematica* where it is checked and used for the analysis (cf. following Section 3.4).

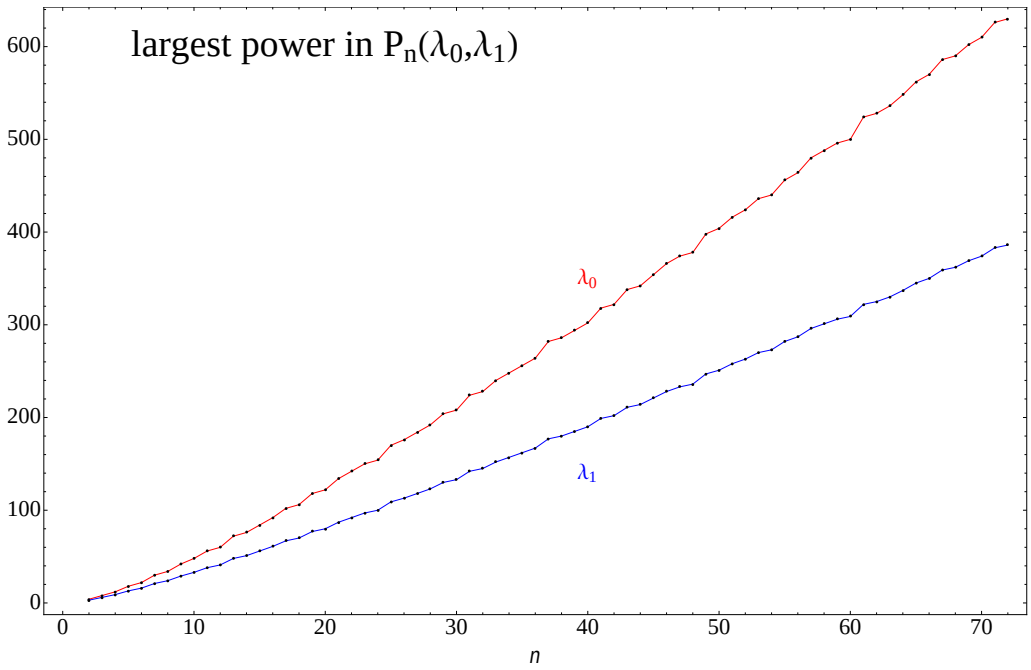

Figure 3.2: The largest power of λ_0, λ_1 occurring in the numerator P_n of the fixed point solution of λ_n is plotted against the index n. The degree of the polynomial P_n in both variables is increasing with n.

3.4 Results

In this section we present the results of our analysis of the flow equation (3.5), ranging up until order $N = 71$ in the polynomial approximation.

We present the calculated eigenvalues from $N = 2$ to $N = 71$ in Figure 3.3.
We find a stable fixed point in each order that can be connected back to the preceding orders in terms of convergence of the couplings λ_i^* and the eigenvalues $-\theta_n$. Numerical values of the fixed point coordinates, the relevant critical exponents and the smallest irrelevant eigenvalue for each approximation order is provided in Table 3.1. We find three attractive eigendirections in each order, where two of those constitute a complex-conjugate pair. This is in agreement with [39, 40, 66, 67] and extends the findings towards $N = 71$. We also note that the different treatment of the modes σ, η, λ and ω compared to [39, 40, 66, 67] made no difference to our qualitative results.
Complex conjugate pairs of eigenvalues also occur for repulsive directions. They are a signifier for degeneracies in the theory and could be lifted through extensions of the $f(R)$ theory where other invariants are also accounted for (eg. Weyl tensor) or through further improvement of the RG dynamics (eg. dynamical ghosts).

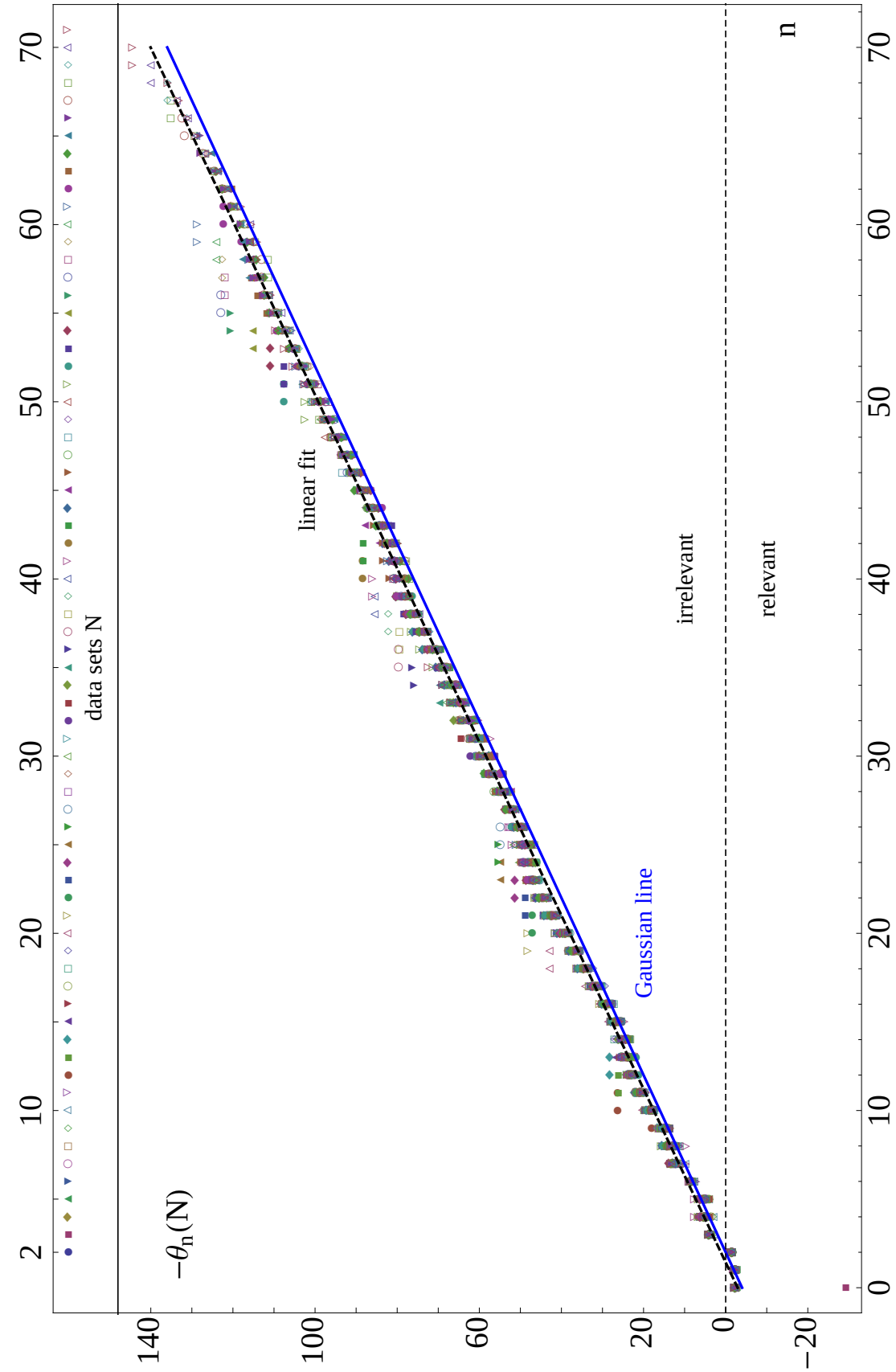

Figure 3.3: The sorted eigenvalues $-\theta_n$ (real part) are plotted for different polynomial approximations $f^N(\rho)$, for N ranging from 2 to 71. The solid blue line corresponds to the Gaussian values for the eigenvalues, whereas the black dashed line shows the linear fit function for the calculated eigenvalues. The irrelevant eigenvalues seem to exhibit a linear hierarchy close to Gaussian behaviour.

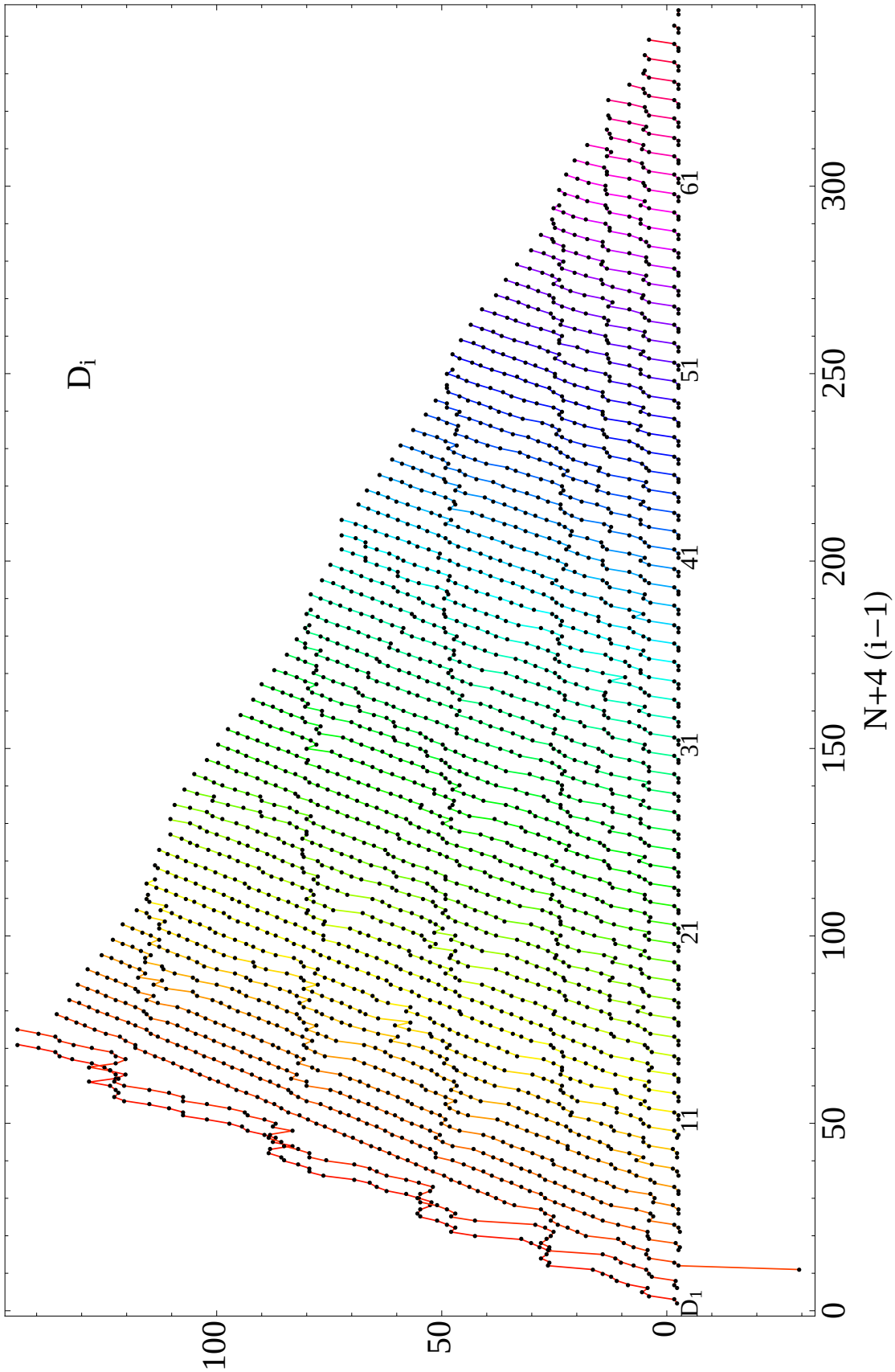

Figure 3.4: The ith largest eigenvalues D_i (real part) are plotted as a function of the approximation order N. For better visibility a horizontal shift of $4\,(i-1)$ is introduced. All D_i grow on average with the approximation order N, thereby supporting the bootstrap hypothesis.

N	λ	g	$\mathrm{Re}(\theta_0)$	$\mathrm{Im}(\theta_0)$	θ_2	θ_3
2	0.118673	0.943051	2.411	1.947		
3	0.101365	1.52932	1.632	1.868	29.30	
4	0.120840	0.967938	2.727	2.046	2.080	-3.863
5	0.113193	0.922501	2.856	2.244	1.602	-3.417
6	0.113725	0.925186	2.503	2.428	1.880	-3.921+4.814 i
7	0.111616	0.911629	2.467	2.218	1.539	-3.993
8	0.110467	0.902707	2.536	2.257	1.296	-3.864
9	0.112294	0.914044	2.359	2.371	1.532	-2.966+4.839 i
10	0.113302	0.920969	2.265	1.989	1.463	-2.668+8.457 i
11	0.113563	0.922230	2.446	2.044	1.299	-3.470
12	0.114132	0.927485	2.600	2.209	1.657	-3.826
13	0.113875	0.925648	2.621	2.284	1.664	-3.904
14	0.113907	0.925845	2.453	2.230	1.702	-3.922
15	0.113539	0.923394	2.514	2.188	1.593	-3.827
16	0.113521	0.923090	2.542	2.223	1.582	-3.843
17	0.113867	0.925244	2.452	2.265	1.670	-3.373+6.053 i
18	0.113877	0.925310	2.449	2.132	1.585	-3.768
19	0.113931	0.925554	2.518	2.161	1.562	-3.754
20	0.114081	0.926930	2.572	2.209	1.643	-3.822
21	0.114077	0.926839	2.565	2.267	1.681	-3.896
22	0.114053	0.926686	2.484	2.198	1.668	-3.856
23	0.113923	0.925801	2.528	2.189	1.620	-3.815
24	0.113938	0.925827	2.544	2.216	1.626	-3.838
25	0.114070	0.926654	2.475	2.237	1.679	-3.782+6.794 i
26	0.114043	0.926473	2.491	2.159	1.615	-3.788
27	0.114065	0.926564	2.529	2.181	1.609	-3.793
28	0.114157	0.927349	2.566	2.210	1.648	-3.824
29	0.114184	0.927497	2.533	2.255	1.694	-3.891
30	0.114141	0.927219	2.505	2.189	1.657	-3.831
31	0.114079	0.926789	2.536	2.191	1.633	-3.814
32	0.114096	0.926867	2.545	2.215	1.644	-3.838
33	0.114163	0.927285	2.480	2.221	1.681	-3.866
34	0.114133	0.927079	2.510	2.170	1.629	-3.797

35	0.114145	0.927126	2.534	2.188	1.628	-3.805
36	0.114202	0.927612	2.562	2.211	1.653	-3.826
37	0.114227	0.927760	2.516	2.241	1.695	-3.878
38	0.114188	0.927508	2.515	2.187	1.655	-3.822
39	0.114153	0.927262	2.540	2.193	1.641	-3.814
40	0.114169	0.927339	2.544	2.215	1.653	-3.838
41	0.114207	0.927578	2.537	2.022	1.539	-3.687
42	0.114180	0.927399	2.520	2.176	1.636	-3.801
43	0.114189	0.927432	2.537	2.192	1.638	-3.811
44	0.114238	0.927832	2.560	2.214	1.659	-3.830
45	0.114257	0.927947	2.503	2.222	1.691	-3.863
46	0.114221	0.927713	2.524	2.186	1.653	-3.816
47	0.114201	0.927566	2.543	2.195	1.646	-3.816
48	0.114216	0.927648	2.543	2.217	1.660	-3.840
49	0.114237	0.927778	2.490	2.195	1.672	-3.837
50	0.114215	0.927630	2.526	2.180	1.641	-3.804
51	0.114268	0.928026	2.547	2.195	1.656	-3.816
52	0.114260	0.927963	2.557	2.215	1.662	-3.832
53	0.114272	0.928039	2.503	2.210	1.685	-3.850
54	0.114243	0.927848	2.528	2.187	1.653	-3.814
55	0.114230	0.927750	2.544	2.196	1.649	-3.816
56	0.114244	0.927825	2.541	2.217	1.665	-3.841
57	0.114254	0.927891	2.498	2.189	1.667	-3.827
58	0.114237	0.927774	2.530	2.183	1.645	-3.806
59	0.114243	0.927800	2.540	2.197	1.649	-3.817
60	0.114269	0.927960	2.525	2.215	1.669	-3.843
61	0.114275	0.928001	2.503	2.174	1.653	-3.805
62	0.114260	0.927954	2.533	2.188	1.653	-3.813
63	0.114253	0.927896	2.546	2.198	1.652	-3.818
64	0.114266	0.927974	2.537	2.220	1.671	-3.846
65	0.114268	0.927985	2.507	2.184	1.661	-3.819
66	0.114255	0.927896	2.534	2.185	1.647	-3.808
67	0.114261	0.927924	2.542	2.199	1.652	-3.820
68	0.114282	0.928054	2.522	2.215	1.673	-3.844

69	0.114283	0.928055	2.510	2.175	1.652	-3.804
70	0.114280	0.928030	2.535	2.184	1.645	-3.804
71	0.114296	0.928123	2.537	2.199	1.655	-3.820

Table 3.1: The fixed point coordinates λ and g, the relevant critical exponents θ_0 and θ_2, and the first irrelevant critical exponents θ_3 are given for each approximation order N. The relevant direction θ_1 is the complex conjugate of θ_0

We also test the hypothesis of near-Gaussianity which was found in [39, 40, 66, 67]. We perform a fit to the linear function

$$\theta_n \approx a\, n - b. \tag{3.36}$$

In the pure Gaussian case the values would read $a_G = 2$ and $b_G = 4$. We use the data sets from $N = 11$ to $N = 71$ where we always exclude the largest two eigenvalues of each set as they can exhibit a degeneracy due to the truncation of the series and therefore exhibit a larger deviation from the next order as a truncation artefact. We find:

$$a = 2.042 \pm 0.002 \tag{3.37}$$

$$b = 2.91 \pm 0.05. \tag{3.38}$$

The slope a is very close to the Gaussian value whereas the constant b exhibits a significant deviation to its Gaussian value. This is also visible in Figure 3.3 where the vast majority of the points lies above the Gaussian line.

The fit gives strong evidence for a linear growth of the eigenvalues, especially since the error bar on the slope a is less than 0.1%.

The same fit as in (3.36) was carried out in [39, 40] for fixed point data up until $N = 35$. They found $a = 2.17 \pm 5\%$ and $b = 4.06 \pm 10\%$. While the corrections from the higher orders to the slope a move it closer to Gaussian value, the constant b moves further out. It still retains a weak dependence on the approximation order N.

Another confirmation of the growth of the eigenvalues can be obtained by considering the ith largest eigenvalue (real part) of a given approximation order

$$D_i(N) = -\theta_{N-i}(N), \tag{3.39}$$

if $-\theta_n(N)$ are the sorted eigenvalues with increasing real part. The bootstrap hypothesis (cf. Section 3.2) is supported, if the D_i turn out to be increasing function of the approximation order. The on-average-growth of the D_i can be observed in Figure 3.4, thereby providing strong evidence for the continued growth of the eigenvalues. Please note that for $N = 3$ Table 3.1 and Figure 3.8 differ in $-\theta_{0,1}$, $-\theta_2$ from strict definition of the $-\theta_n(N)$ having increasing real part with n. There $-\theta_{0,1}$ feature the relevant complex conjugate and $-\theta_2$ features the real relevant eigenvalue. At $N = 3$ the magnitude of the real relevant one is larger than the complex conjugate pair and therefore it becomes the smallest eigenvalue of the spectrum.
Extrapolation of these results suggests that higher invariants in the Ricci scalar R do not generate additional attractive directions but only repulsive ones with linearly increasing magnitude (cf. Section 3.7).

3.5 Convergence

In order to assess the reliability of our results, we investigate the convergence of the couplings λ_n and the eigenvalues $-\theta_n$ with increasing approximation order N. The convergence of the couplings is displayed in Figure 3.5. We observe the relative error for each individual coupling approaching 0 with increasing approximation order and thereby supporting the bootstrap approach. This is best visible for low order couplings because they are present in most of the approximation orders and have the most data points. A high order coupling compared to the studies $N_{\max} = 71$ will not lead to a visible convergence pattern yet. However from the behaviour of the lower order couplings, it is expected that they will exhibit a similar convergence pattern if more orders were taken into account.
The relative error becomes a misleading indicator of convergence when the value of a coupling at $N_{\max}$ is close to 0, as this leads to large relative errors even for small deviations. This is why λ_{53} was omitted in Figure 3.5. Further examples for this behaviour are λ_6 and λ_{10}. These couplings have already stabilised over many more orders compared to λ_{53}, so the relative error is already tamed for the higher approximation orders. It is largest at very low approximation orders (cf. Figure 3.5).

When looking at the speed of convergence, a more detailed look at the relative error is necessary. The convergence for λ_0, λ_1 and λ_2 are given in Figure 3.6. From Figure 3.6 it is clear that asymptotically roughly one digit precision is gained every 50 approximation orders for λ_0. For λ_1 is converging faster and gaining roughly one digit precision every 40

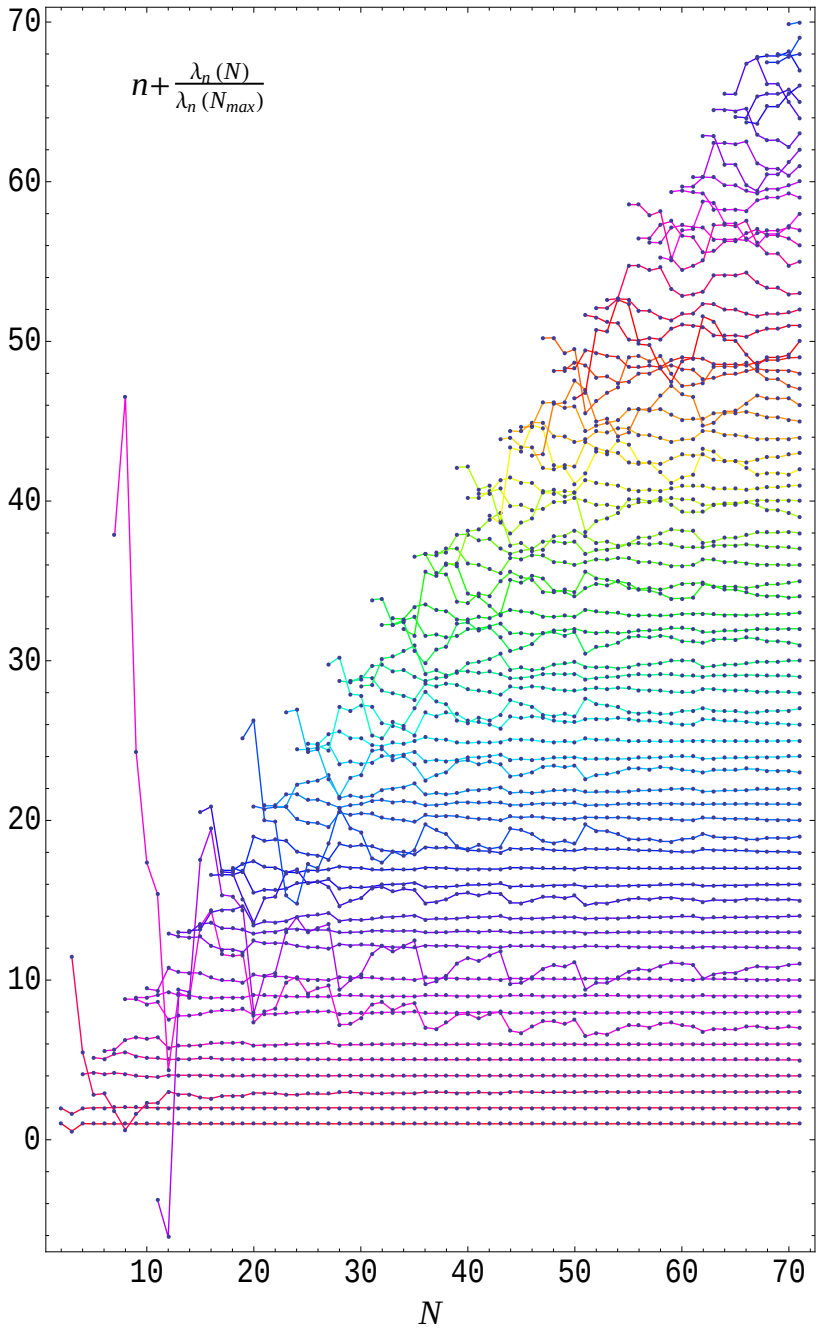

Figure 3.5: The individual couplings λ_n at each approximation order are compared against its value at the highest approximation order $N_{\max} = 71$, using the relative error $\lambda_n(N)/\lambda_n(N_{max}) - 1$. For better visibility each relative error line gets an additional offset $n + 1$. Here λ_{53} was omitted for better visibility, as $\lambda_{53}(71) \approx 0$. All couplings exhibit a convergence pattern over the approximation orders.

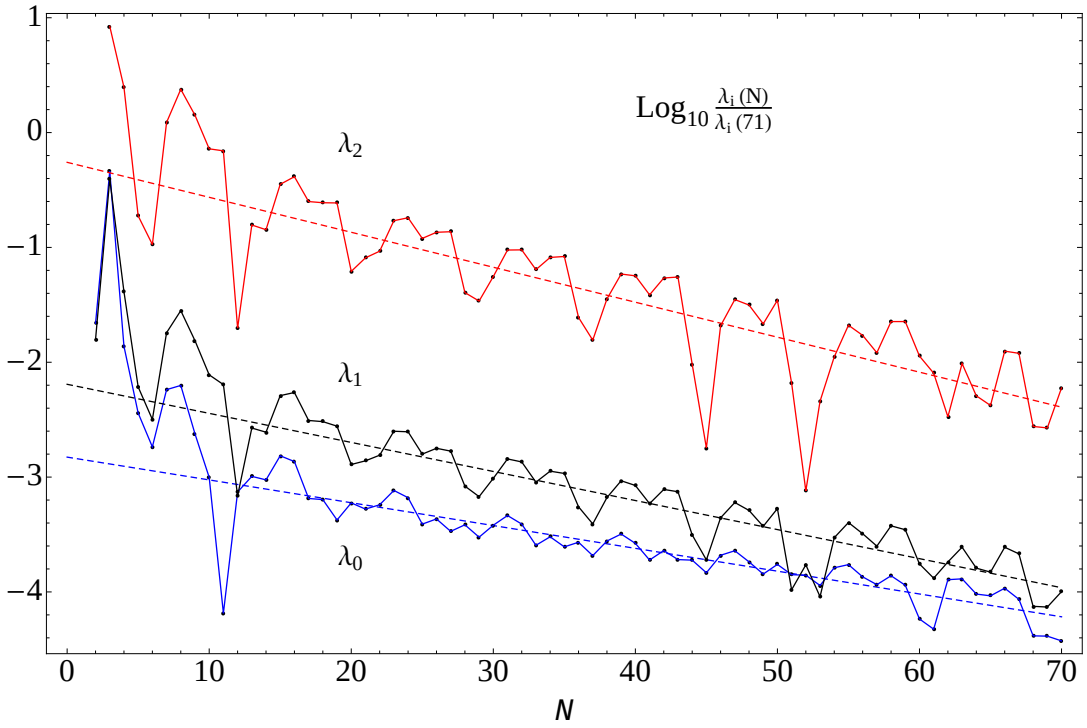

Figure 3.6: The relative errors of $\lambda_i(N)$ are given compared to $\lambda_i(N_{\max} = 71)$. The asymptotic speed of convergence is denoted by a dashed line for each coupling.

orders, although it is starting out at a lower precision. Interestingly, λ_2 still has the fastest convergence rate with roughly one digit precision gained every 33 orders. However, this behaviour cannot persist as λ_2 is a function of λ_0 and λ_1 and therefore it cannot exceed the precision of those.

The couplings λ_n exhibit an eightfold periodicity sign pattern from $n = 4$ onwards. It can be seen from the coupling values at the highest approximation order $N_{\max} = 71$ in Table 3.2. The source of this sign pattern is a complex conjugate pair of singularities in complex ρ plane close to the origin. The distance from the origin limits the radius of convergence of our polynomial expansion. One cannot expect to observe the sign pattern rigorously for high order couplings larger than λ_{60} since they have not gone through enough orders to settle in yet. However there are two settled-in couplings that break the sign pattern, namely λ_{10} and λ_{53}. Their values lie remarkably close to 0, especially compared to neighbouring couplings. Therefore, there is still room within the error of the coupling to change sign according to the periodicity pattern. Even a limiting value with the current sign would be ok and implies that the oscillation angle of the couplings is close to but not quite $\pi/4$.

λ_0	λ_1	λ_2	λ_3				
0.2463	-1.077	0.008486	-0.4795				
λ_4	λ_5	λ_6	λ_7	λ_8	λ_9	λ_{10}	λ_{11}
-0.3755	-0.2271	0.005958	0.1957	0.2648	0.2017	0.009851	-0.2364
λ_{12}	λ_{13}	λ_{14}	λ_{15}	λ_{16}	λ_{17}	λ_{18}	λ_{19}
-0.3643	-0.2492	0.05674	0.3575	0.4637	0.3114	-0.05698	-0.5134
λ_{20}	λ_{21}	λ_{22}	λ_{23}	λ_{24}	λ_{25}	λ_{26}	λ_{27}
-0.7805	-0.5397	0.2105	0.9892	1.200	0.6528	-0.3836	-1.476
λ_{28}	λ_{29}	λ_{30}	λ_{31}	λ_{32}	λ_{33}	λ_{34}	λ_{35}
-2.044	-1.334	0.8319	3.140	3.519	1.324	-1.954	-4.499
λ_{36}	λ_{37}	λ_{38}	λ_{39}	λ_{40}	λ_{41}	λ_{42}	λ_{43}
-5.406	-3.483	2.549	10.11	11.81	3.304	-9.369	-16.08
λ_{44}	λ_{45}	λ_{46}	λ_{47}	λ_{48}	λ_{49}	λ_{50}	λ_{51}
-14.38	-7.034	8.447	31.41	40.34	10.42	-41.43	-62.59
λ_{52}	λ_{53}	λ_{54}	λ_{55}	λ_{56}	λ_{57}	λ_{58}	λ_{59}
-35.54	0.1220	26.79	80.35	136.2	64.82	-155.2	-284.9
λ_{60}	λ_{61}	λ_{62}	λ_{63}	λ_{64}	λ_{65}	λ_{66}	λ_{67}
-123.9	128.2	168.0	144.5	340.1	354.3	-408.7	-1253.
λ_{68}	λ_{69}	λ_{70}					
-685.5	925.0	1254.					

Table 3.2: The couplings λ_n at the highest approximation order $N_{\max} = 71$.

An estimate of the radius of convergence of the polynomial expansion can be obtained by looking at the growth rate of the couplings

$$\rho_c = \left(\frac{\lambda_n}{\lambda_{n+m}} \right)^{1/m} \tag{3.40}$$

The precise value of the estimate depends now on the explicit choices of n, m, the approximation order N and the data range over which an average is taken. m should be an integer multiple of 8, since we observe an eightfold periodicity sign pattern in the couplings $(++++----)$. We find

$$\rho_c = 0.878 \tag{3.41}$$

as the mean value over all possible radii, where we excluded the lowest 5 and highest 10 couplings of each approximation order N.

The eigenvalues also exhibit a convergence pattern with the approximation order. This is presented in Figure 3.7 and a more detailed look at the relevant eigenvalues in Figure 3.8. The convergence of the eigenvalues is slower than the convergence of the couplings

3.6 Periodicity and cycle averages

The eightfold periodicity pattern was already observed in the previous section, as being present among the couplings at a given approximation order N (cf. Table 3.2). Its origin was identified as a complex pole in the full function $f(\rho)$.
Analysing the convergence patterns of the couplings (cf. Figure 3.6 for best visibility) and of the eigenvalues (cf. 3.8 for best visibility), it becomes apparent that there is also an eightfold periodicity pattern within the convergence over the approximation orders N. Such an eightfold periodicity pattern was also found in critical scalar field theories [112]. The source of this pattern can be traced back to our boundary condition (3.28), which forces the highest two couplings λ_N and λ_{N+1} of a given approximation order to vanish. Thereby, these couplings break the periodicity pattern found at a given order N (cf. Table 3.2). With the variation of the approximation order, the position of the breaking is shifted through the eightfold cycle, and this is reflected in the convergence pattern.

In order to minimise the dependence of couplings and eigenvalues on the periodicity pattern, we introduce an average over the highest eightfold cycle in the approximation order N. The average of a quantity x is denoted by $\langle x \rangle$ and defined as

$$\langle x \rangle = \frac{1}{8} \sum_{N=N_{\max}-7}^{N_{\max}} x(N) \tag{3.42}$$

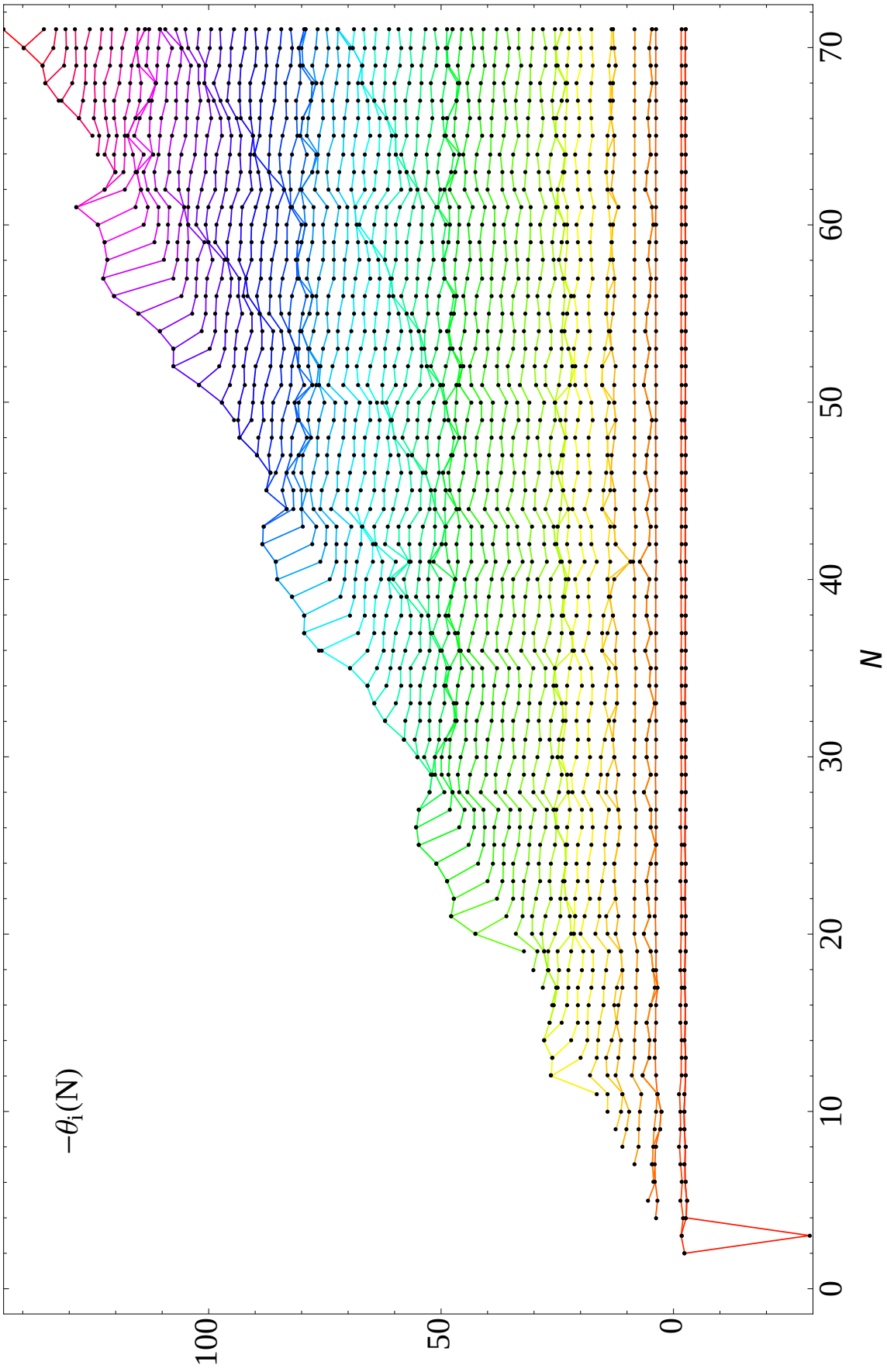

Figure 3.7: The real part of all eigenvalues $-\theta_i(N)$ is plotted against the approximation order N up until $N_{\max} = 71$. The index i denotes the ith lowest eigenvalue. From left to right the fluctuations of the eigenvalues get smaller, showing convergence.

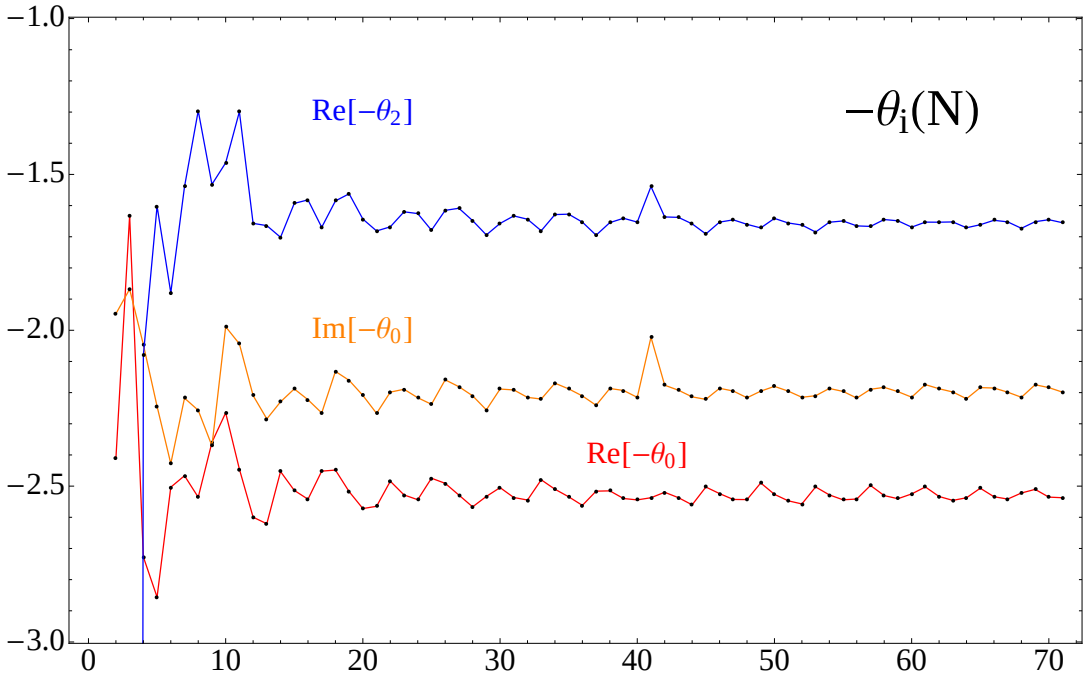

Figure 3.8: The real part of all eigenvalues $-\theta_i(N)$ is plotted against the approximation order N up until $N_{\max} = 71$. This is a close up for the relevant eigenvalues, including the imaginary part of the complex conjugate pair. From left to right the fluctuations of the eigenvalues get smaller, showing convergence.

For the first seven couplings the averages are:

$$\langle \lambda_0 \rangle = 0.246279 \pm 0.0038\% \tag{3.43}$$

$$\langle \lambda_1 \rangle = -1.07758 \pm 0.0081\% \tag{3.44}$$

$$\langle \lambda_2 \rangle = 0.008438 \pm 0.45\% \tag{3.45}$$

$$\langle \lambda_3 \rangle = -0.4811 \pm 0.22\% \tag{3.46}$$

$$\langle \lambda_4 \rangle = -0.3764 \pm 0.15\% \tag{3.47}$$

$$\langle \lambda_5 \rangle = -0.2245 \pm 0.77\% \tag{3.48}$$

$$\langle \lambda_6 \rangle = 0.00598 \pm 7.9\%. \tag{3.49}$$

The first two can be easily translated into averages for the dimensionless Newton's coupling and the dimensionless cosmological constant

$$\langle g \rangle = 0.928005 \pm 0.0081\% \tag{3.50}$$

$$\langle \lambda \rangle = 0.10605 \pm 0.020\%. \tag{3.51}$$

And for the relevant eigenvalues we obtain:

$$\langle -\mathrm{Re}\, \theta_0 \rangle = -2.528 \pm 0.53\% \tag{3.52}$$

$$\langle -\mathrm{Im}\, \theta_0 \rangle = -2.195 \pm 0.73\% \tag{3.53}$$

$$\langle -\theta_2 \rangle = -1.657 \pm 0.63\% \tag{3.54}$$

. We can also construct scale-invariant quantities out of the couplings which do not depend on rescaling of the metric. The most important one is $g\,\lambda$, as it has the interpretation of a measure for the strength of the gravitational coupling [115]

$$\langle g\,\lambda \rangle = 0.106047 \pm 0.020\%. \tag{3.55}$$

We also observe

$$\langle g\,\lambda \rangle = \langle g \rangle \cdot \langle \lambda \rangle \tag{3.56}$$

to a precision of $10^{-7}\%$ This is a remarkable agreement, well within the error bars of (3.55),(3.50) and (3.51). It provides strong evidence that the dependence on the periodicity pattern is indeed nearly removed through the cycle averages.

This observation motivates a different approach to the subsequent computation of the fixed point, compared to the boundary condition in (3.28). We present and examine this approach in the following Section 3.7.

3.7 High range

In this section we provide a different method for the analysis of the fixed point properties to very high orders in the Ricci scalar, which benefits from the previous findings, in particular the cycle averages computed in Section 3.6.

Previously the fixed point was determined via algebraic expressions of the couplings λ_n. It proved to be very demanding regarding the computational power needed (cf. Section 3.3.3). Here we invert the strategy and numerically compute all higher couplings λ_n by choosing suitable initial conditions for λ_0 and λ_1. We use the cycle averages $\langle\lambda_0\rangle$ (3.43) and $\langle\lambda_1\rangle$ (3.44) as the fixed point location. Previously, the boundary condition (3.28) was used to determine the fixed point coordinates λ_0 and λ_1. Using this approach we can go to substantially higher orders as solving the recursion relation (3.26) algebraically is no longer a limiting factor. The computational effort lies now mainly in the computation of the stability matrix (3.33). Exemplarily we go to $N_{\max} = 1000$.

The challenge of this method is the choice of the initial conditions. The fixed point needs to lead to an $f(\rho)$ with a finite radius of convergence and to a meaningful eigenvalue spectrum.

The analysis in the previous Section 3.6 provides a good starting point because the cycle averages aim to remove the dependence on the boundary condition of our polynomial analysis and can be viewed as a best estimate for the fixed point.

3.7.1 Implementation

The code for solving the recursion relation (3.26) and computing the eigenvalue spectrum is written in *Mathematica*. The time-intense operation is the computation of the stability matrix as it grows quadratically with the approximation order N. Since all the entries of the stability matrix, or more precisely the entries matrices A and B that are used to obtain the stability matrix via (3.33), can be calculated independently, it can be parallelised using bulit-in *Mathematica* funcitons. The code is executed on the University of Sussex high performance cluster *apollo* using 40 nodes. The overall runtime for one set of initial conditions is $\sim$ 25 hours using a CPU time of roughly $\sim$ 393 hours which leads to a parallelisation factor of ~ 16.

3.7.2 Results

The resulting coupling spectrum for the best fixed point estimate is presented in Figure 3.9. It is conceivable that the couplings follow the asymptotic behaviour

$$\lambda_n \approx a\, \sin(b\, n + c)\, \rho_c^{-n} \tag{3.57}$$

with parameters a, b, c and the radius of convergence ρ_c. The ansatz in (3.57) mimics the periodicity pattern with the phase b and the initial phase shift c. The amplitude a controls the overall magnitude of the couplings. We can use (3.57) as a starting point for a coupling analysis in our data. In order to stabilise a fit to this equation, we take the logarithm of the absolute value of this equation:

$$\log(\lambda_n) \approx \log(a) + \log(\sin(b\, n + c)) - n\, \log(\rho_c). \tag{3.58}$$

This is a linear function in the fit parameter n apart from the $\log(\sin(b\, n + c))$ term. It has the potential to spoil the linear fit, if there are many values were the sine is close to 0, and therefore the logarithm grows large. Assuming a purely linear behaviour $\log(\lambda_n) \approx \alpha\, n + \beta$, we actually observe the fit to describe the growth rate of $\log(\lambda)$ very well. We find a radius of convergence of

$$\rho_c = 0.7804 \pm 0.0001. \tag{3.59}$$

This is below than the one obtained in Section 3.4 equation (3.41) for the boundary condition, $\lambda_N = \lambda_{N+1} = 0$, which was 0.878.
We observe three relevant eigenvalues

$$-\theta_{0,1} = -2.5597 \pm 2.1808\ i \tag{3.60}$$

$$-\theta_2 = -1.6522 \tag{3.61}$$

and a whole spectrum of irrelevant eigenvalues presented in Figure 3.10 The irrelevant eigenvalues are tested for their near Gaussianity and fitted to the linear function $a\, n - b$. We obtain

$$a = 1.99992 \pm 0.00003, \tag{3.62}$$

$$b = 1.67 \pm 0.02. \tag{3.63}$$

The slope a is extremely close to its Gaussian value of 2, whereas the constant b significantly deviates from the Gaussian value of 4. This provides strong evidence for the linear growth of the irrelevant eigenvalues and suggests that we are in the region of a physically

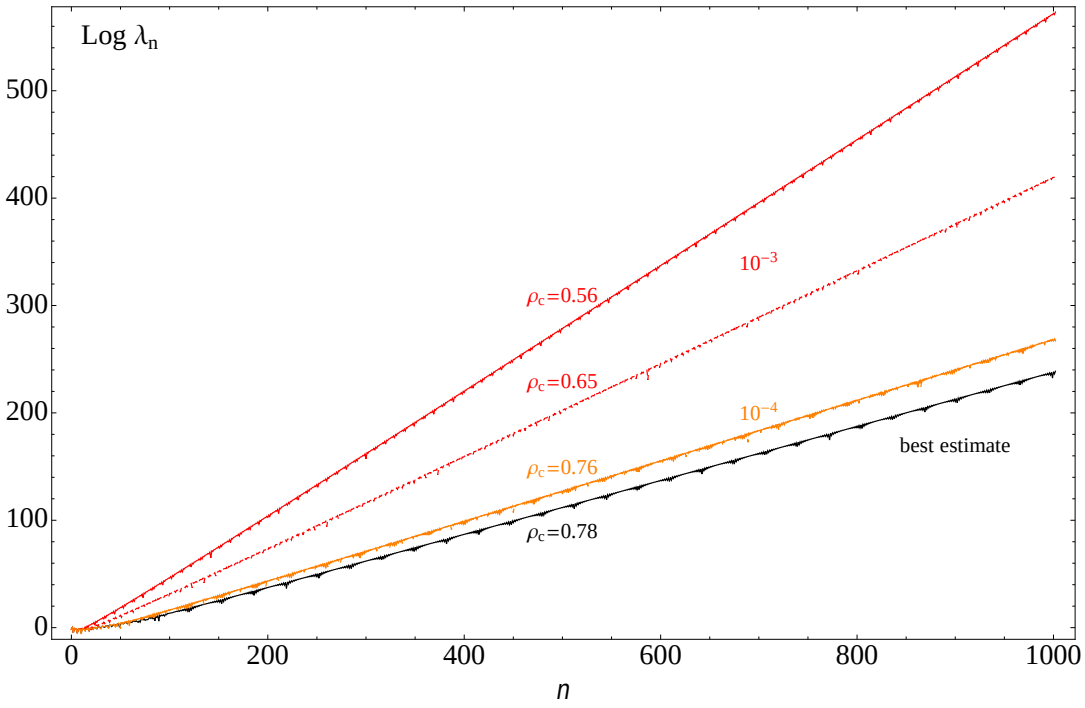

Figure 3.9: The spectrum of the logarithm of the absolute value of λ_n is presented at $N = 1001$. The black line represents the best estimate whereas the orange (red) lines show the results for a on the level of 10^{-4} (10^{-3}) differing initial condition. The split of the orange lines is not visible and they lead effectively to the same behaviour. For each study the resulting radius of convergence of $f(\rho)$ is given as well. The best estimate exhibits the largest radius of convergence.

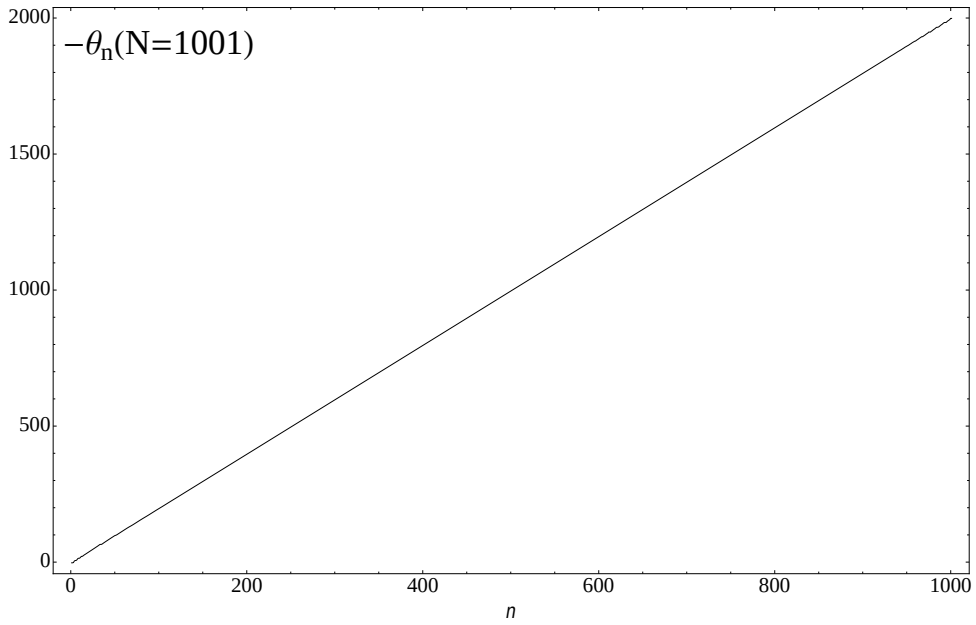

Figure 3.10: The spectrum of the real part of all eigenvalues at $N = 1001$ for the best estimate. It shows a linear growth of the irrelevant eigenvalues confirming the picture from the $N = 71$ study.

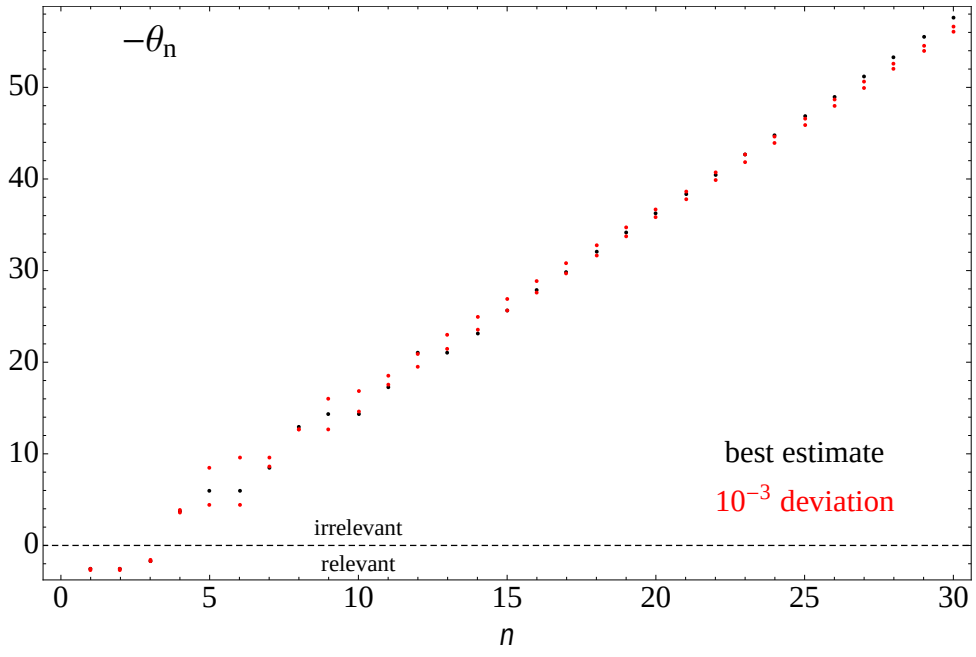

Figure 3.11: The more detailed spectrum of the real part of the first 30 eigenvalues at $N = 1001$ for the best estimate (black) and the two studies with 10^{-3} deviation (red). It is noteworthy that deviations here are small compared to the difference in the couplings in Figure 3.9.

meaningful fixed point candidate.

We also test this best estimate result for its stability against variations of the initial condition. We introduce variations of the initial condition of the form

$$\lambda_0|_{\text{initial}} = \langle\lambda_0\rangle \left(1 \mp 10^{-m}\right) \tag{3.64}$$

$$\lambda_1|_{\text{initial}} = \langle\lambda_1\rangle \left(1 \pm 10^{-m}\right). \tag{3.65}$$

Note the opposite signs in the variation between $\lambda_0|_{\text{initial}}$ and $\lambda_1|_{\text{initial}}$. It ensures that in the different fixed point basis with the cosmological constant λ and Newton's coupling g, the cosmological constant is not left unchanged, as it depends on the ratio λ_0/λ_1.
The effects of different deviations m on the coupling spectrum are presented in Figure 3.9. For $m = -5$ the resulting spectrum would be so close to the best estimate that it cannot be distinguished in the plot and was therefore omitted from Figure 3.9. Variations of 10^{-4} already show a visible deviation from the best estimate and exhibit a smaller radius of convergence 0.76. Both variations of 10^{-4} generate a coupling spectrum that nearly lies on top of each other and therefore they cannot be distinguished in Figure 3.9. For the 10^{-3} variations the splitting becomes visible. Both exhibit a significantly smaller radius of convergence than the best estimate.

We also cross-checked the numerical precision by which the generated $f(\rho) = \sum \lambda_n \rho^n$ satisfies the fixed point equation (3.23). All studies solve the fixed point condition numerically within their radius of convergence $\rho < \rho_c$. The precision depends on the distance from the origin $\rho = 0$ at which the solution is exact by construction.

Despite these differences in the coupling spectrum, the eigenvalue spectrum is remarkably stable such that differences are only visible in a zoom-in plot 3.11 where one one compares the best estimate eigenvalues to the 10^{-3} variations. The occurrence of three relevant directions is not altered, and the eigenvalues only exhibit small numerical differences.

Thereby variations of the initial condition mainly influence the coupling spectrum and thereby the radius of convergence of our polynomial approximation. Variations of 10^{-4}, which correspond to the conservative error bars on our fixed points coordinates (cf. Figure 3.6), still lead to a radius of convergence that is comparable to the best estimate.

3.8 Summary

We have analysed a new RG flow of a template theory of quantum gravity which we wrote as a polynomial $f(R)$ in the Ricci scalar. The new flow removed explicit poles in the dimensionless Ricci scalar ρ present in previous approximations (cf. Section 2.6). Interestingly, we found that the poles at $\rho = 3$ and $\rho = 4$ make only a small quantitative impact on the results and we are consistent with previous findings.

A new code was developed that made it possible to examine approximation orders up to $N = 71$, which is more than double the order previously accessible. The existence of three relevant directions at the UV fixed point could be confirmed. The claim of linear growth of the irrelevant eigenvalues with subsequent extension of the approximation order is substantiated.

The stability and precision of our results motivated an extrapolation approach where we analysed the flow equation in the vicinity of our explicitly found fixed point solution at $N = 71$ up to $N = 1001$. We found consistency with the coupling and eigenvalue spectrum of our explicit results within their error bars.

All results are consistent with the bootstrap approach. A new operator with a higher mass dimension generates a new eigendirection at the fixed point that has a larger irrelevant scaling exponent than all other operators previously accounted for. This constitutes evidence that a stable and physically meaningful fixed point has been identified.

It would now be interesting to extend the polynomial solution to larger field values in ρ beyond the radius of convergence. In principle this can be done up to $\rho = 2$ following the method presented in [66] and maybe even extended further due to the absence of poles at $\rho = 3, 4$ in the improved flow.

Going beyond the previously studied order 35 in $f(R)$ gravity has provided us with further insights into the structure of a polynomial fixed point solution. However this does not imply that the system is fully understood and one can stop here. Although we have strong evidence to believe that even higher operators than the ones considered here will further validate the established picture, we cannot be absolutely sure due to the non-perturbative nature of the flow equation where there is apriori no ordering principle for the relevance of gravitational operators. From this it becomes clear that the numerical analysis is the first important step on the way to understanding polynomial $f(R)$ gravity and needs to supplemented by more analytical analysis in future work. The goal is to understand the

significance of any power of the Ricci scalar without an individual explicit numerical computation.

This concludes the considerations of flow equations featuring pure $f(R)$ gravity. In the next Chapter 4, we consider the interplay of $f(R)$ quantum gravity with minimally coupled matter fields.

Chapter 4

Minimal matter in the $f(R)$ approximation

In this chapter we want to extend our findings from pure $f(R)$ quantum gravity (cf. Chapter 3) further by introducing matter fields. The matter is treated as non-selfinteracting and having no scale dependence. It will influence the renormalisation group of the gravitational couplings due to its presence (cf. Section 4.2). We address the question of how different matter types, namely scalars, fermions and vectors, influence the existence and properties of a gravitational UV fixed point (cf. Sections 4.3 and 4.4). We put particular emphasis on the examination of effects on higher scalar curvature invariants beyond the Einstein-Hilbert approximation (cf. Section 4.4). Already in pure $f(R)$ gravity, the introduction of the R^2 operator leads to a third relevant direction at the UV fixed point (cf. Table 3.1).

4.1 Introduction

It is a well-known fact that the renormalisation group of Yang-Mills theory with a $SU(N_c)$ symmetry group exhibits a non-interacting UV fixed point [116, 117]. This behaviour is called asymptotic freedom.

However matter fields can drastically influence the RG behaviour of Yang-Mills theory. On the level of the one-loop beta function, it enters as

$$\beta(g) = -\left(\frac{11}{3}N_c - \frac{2}{3}N_F\right)\frac{g^3}{16\pi^2} + \mathcal{O}\left(g^5\right), \tag{4.1}$$

where N_c is the number of colours and N_F is the number of fermions in the theory. In order to have asymptotic freedom, the dominant contribution to the beta function needs to be

negative. However as the fermions contribute with the opposite sign, there is maximally allowed number of fields that is compatible with asymptotic freedom $N_{F,\text{critical}} = \frac{11}{2} N_c$. So the overall physical behaviour is strongly influenced by the presence of matter fields. The generalisation of a non-interacting UV fixed point in asymptotic freedom is an interacting UV fixed point in the asymptotic safety scenario [7].

As generally discussed in Section 2.5, one of the main features of the asymptotic safety scenario for gravity [14, 15, 16, 17, 18, 19, 20, 12, 21] is the existence of a non-trivial fixed point for the dimensionless Newton's coupling g. The corresponding beta function has the structure

$$\beta_g = (2 + \eta)\, g, \tag{4.2}$$

where η is the anomalous dimension. For a non-gaussian fixed point $\eta^* = -2$ is required. In a one loop expansion of η, minimally coupled scalar, fermionic and vector matter fields couple as [52]

$$\eta = -\left(22 - n_{\text{scalar}} - 2\, n_{\text{fermion}} + 4\, n_{\text{vector}}\right) \frac{g}{6\,\pi} + \mathcal{O}(g^2), \tag{4.3}$$

where n_{scalar}, n_{fermion}, n_{vector} refer to the number of scalar, fermion and vector fields respectively. The magnitude of the constant term -22 depends on the gauge parameters and the specific regulators used. The key observation is that the scalar fields (together with the fermions) contribute with the opposite sign at one loop level. This immediately leads to the question whether the fixed point might be spoiled through the presence of matter fields. Here we would like to address this question and focus on minimally coupled scalar, fermion and vector matter, going beyond the perturbative treatment.

Recently a conceptually very interesting discovery was made for non-abelian gauge theories coupled to scalar and fermionic matter [118, 119]. Asymptotic safety occurred only in the presence of matter fields. This leads to the question, whether matter fields coupled to gravity can generate new interacting fixed points that are not present at pure gravity.

4.2 Matter fields

We are again interested in the renormalisation group evolution of the gravitational couplings λ_n in polynomial $f(R)$ gravity (cf. Section 2.4). Here the renormalisation group is driven by the metric field, and scalar, fermionic and vector fields.

The pure gravity part uses polynomial $f(R)$ gravity for which we already developed procedure of functional renormalisation in Chapter 2. Each power of the Ricci scalar R^n

comes with its own dimensionless coupling λ_n. An approximation of order N includes all monomials up to R^{N-1}.

The matter part contains no self interactions of the fields $\phi_i, \psi_i, A_{i,\mu}$. The new parameters that have been introduced are the number of scalar fields n_S, the number of fermions n_D and the number of the Maxwell vectors n_M.

The combined effective average action has the form:

$$\Gamma_k = \Gamma_k|_{\text{pure gravity}} + \sum_{i=1}^{n_S} \Gamma_i^S + \sum_{i=1}^{n_D} \Gamma_i^D + \sum_{i=1}^{n_M} \Gamma_i^M \tag{4.4}$$

$$\Gamma_k|_{\text{pure gravity}} = \int d^4x\,\sqrt{g}\,\frac{1}{16\,\pi}\,f(R) = \sum_{n=0}^{N-1} \lambda_n\,k^{-2\,n+4}\,\frac{1}{16\,\pi}\int dx^4\,\sqrt{g}\,R^n \tag{4.5}$$

$$\Gamma_i^S = \int d^4x\,\sqrt{g}\,\frac{1}{2}\nabla_\mu\,\phi_i\nabla^\mu\,\phi_i \tag{4.6}$$

$$\Gamma_i^D = \int d^4x\,\sqrt{g}\,\bar{\psi}_i\,\not{D}\,\psi_i \tag{4.7}$$

$$\Gamma_i^M = \int d^4x\,\sqrt{g}\,\left(\frac{1}{4}\,F_i^{\mu\nu}\,F_{i,\mu\nu} + \frac{1}{2}(\nabla^\mu A_{i,\mu})^2 - \bar{c}_{A_i}\,\Box\,c_{A_i}\right). \tag{4.8}$$

The Maxwell vectors are considered in Lorenz gauge and c_{A_i}, $\bar{c}_{A_i}$ are the corresponding ghosts.

The evolution of Γ_k (4.4) is again described via the flow equation of the functional renormalisation group (2.13). The matter parts of the action contribute on the right hand side of the flow equation only since we do not take them to be dynamical. The right hand side of the flow equation decouples into a contribution from pure gravity $\mathcal{S}^{\text{gravity}}$ (2.67) and contributions from the matter fields $\mathcal{S}^{\text{matter}}$:

$$\partial_t\Gamma_k = \mathcal{S}^{\text{gravity}} + \mathcal{S}^{\text{matter}}. \tag{4.9}$$

In the absence of matter fields, $\mathcal{S}^{\text{matter}} = 0$, the flow (4.9) falls back to the pure gravity flow discussed extensively in Chapter 3. The matter contribution consist of four traces, corresponding to the scalars, fermions, vectors and the vector ghosts:

$$\begin{aligned}\mathcal{S}^{\text{matter}} = {} & n_S\,\frac{1}{2}\,\text{Tr}\left[\frac{\partial_t\mathcal{R}_k^{\phi\phi}}{\Gamma^{(2)}_{\phi\phi} + \mathcal{R}_k^{\phi\phi}}\right] - n_D\,\text{Tr}\left[\frac{\partial_t\mathcal{R}_k^{\psi\psi}}{\Gamma^{(2)}_{\psi\psi} + \mathcal{R}_k^{\psi\psi}}\right] \\ & + n_M\,\frac{1}{2}\,\text{Tr}\left[\frac{\partial_t\mathcal{R}_k^{AA}}{\Gamma^{(2)}_{AA} + \mathcal{R}_k^{AA}}\right] - n_M\,\text{Tr}\left[\frac{\partial_t\mathcal{R}_k^{\bar{c}_A c_A}}{\Gamma^{(2)}_{\bar{c}_A c_A} + \mathcal{R}_k^{\bar{c}_A c_A}}\right].\end{aligned} \tag{4.10}$$

The matter traces in (4.10) contribute with different signs. The positive sign in front of the scalar and vector fields reflects their bosonic nature, whereas the negative sign in front of the fermions and vector ghosts is a reflection of their fermionic nature.

The scalars and Maxwell ghosts employ a type I cutoff and the fermions and Maxwell

fields a type II cutoff (for cutoff types see Section 3.1). Recall that $\rho = R/k^2$ is the dimensionless Ricci scalar

The scalar fields (treatment in [41, 42, 44])

$$\Delta_{\phi\phi} = -\nabla^2 \tag{4.11}$$

$$\Gamma^{(2)}_{\phi\phi} = \Delta_{\phi\phi} \tag{4.12}$$

$$\frac{1}{2}\,\mathrm{Tr}\left[\frac{\partial_t \mathcal{R}^{\phi\phi}_k}{\Gamma^{(2)}_{\phi\phi} + \mathcal{R}^{\phi\phi}_k}\right] = \frac{29\,\rho^2 + 360\,\rho + 1080}{34560\,\pi^2}\,. \tag{4.13}$$

The cutoff treatment of fermions is discussed in detail in [120], and we employ a type II cutoff to correctly implement the renormalisation of the Dirac operator:

$$\Gamma^{(2)}_{\psi\psi} = -\not{D} \tag{4.14}$$

$$\not{D} + \mathcal{R}^{\psi\psi}_k = \not{D} + (k - \not{D})\,\theta(k^2 - \not{D}^2) \tag{4.15}$$

$$\Delta_{\psi\psi} = \not{D}^2 = -\nabla^2 + \frac{\rho}{4} \tag{4.16}$$

$$\begin{aligned}\mathrm{Tr}\left[\frac{\partial_t \mathcal{R}^{\psi\psi}_k}{\Gamma^{(2)}_{\psi\psi} + \mathcal{R}^{\psi\psi}_k}\right] &= -\frac{1}{2}\,\partial_t\,\mathrm{Tr}\left[\log\left(\not{D} + \mathcal{R}^{\psi\psi}_k\right)^2\right] \\ &= -\frac{1}{2}\,\mathrm{Tr}\left[\frac{\partial_t\, R_k(\not{D}^2)}{\not{D}^2 + R_k(\not{D}^2)}\right] \qquad (4.17)\\ &= \frac{11\,\rho^2 - 720\,\rho + 4320}{34560\,\pi^2}\,. \qquad (4.18)\end{aligned}$$

The Maxwell fields [121] (review in [44])

$$\Delta_{AA} = -\nabla^2 + \frac{\rho}{4} \tag{4.19}$$

$$\Gamma^{(2)}_{AA} = \Delta_{AA} \tag{4.20}$$

$$\frac{1}{2}\,\mathrm{Tr}\left[\frac{\partial_t \mathcal{R}^{AA}_k}{\Gamma^{(2)}_{AA} + \mathcal{R}^{AA}_k}\right] = \frac{-\rho^2 - 180\,\rho + 1080}{8640\,\pi^2}\,. \tag{4.21}$$

The Maxwell ghosts

$$\Delta_{\bar{c}_A c_A} = -\nabla^2 \tag{4.22}$$

$$\Gamma^{(2)}_{\bar{c}_A c_A} = -\Delta_{\bar{c}_A c_A} \tag{4.23}$$

$$\mathrm{Tr}\left[\frac{\partial_t \mathcal{R}^{\bar{c}_A c_A}_k}{\Gamma^{(2)}_{\bar{c}_A c_A} + \mathcal{R}^{\bar{c}_A c_A}_k}\right] = \frac{-29\,\rho^2 - 360\,\rho - 1080}{17280\,\pi^2}\,. \tag{4.24}$$

The matter terms appearing on the right hand side of the flow (4.9) have the structure of a polynomial in the Ricci scalar of order 2, which is the same as the terms P_0^S (3.12) and P_0^V (3.13) in $I_0[f]$ (3.7) in the pure gravity flow equation (3.5). Thereby the matter flow

equation retains its structure known from pure gravity (3.5)

$$\dot{f} - 2\,\rho\,f' + 4\,f = c\,I[f] = c\,\left(I_0[f] + I_1[f]\,\dot{f}' + I_2[f]\,\dot{f}''\right) \tag{4.25}$$
$$c = \frac{1}{24\,\pi}$$

and the matter fields simply introduce a new term P_0^M into $I_0[f]$:

$$I_0[f] = P_0^S + P_0^V + P_0^M + \frac{P_0^{S1}\,f' + P_0^{S2}\,f'' + P_0^{S3}\,f'''}{D^S} + \frac{P_0^{T1}\,f' + P_0^{T2}\,\rho\,f''}{D^T} \tag{4.26}$$

$$P_0^M = 24\,(n_S - 4\,n_D + 2\,n_M) + 8\,(n_S + 2\,n_D - 4n_M)\,\rho + \frac{1}{45}\,(29\,n_S\, - 11\,n_D - 62\,n_M)\,\rho^2 \tag{4.27}$$

All other terms retain their values (3.8) to (3.21) known from the pure gravity flow in chapter 3. Therefore on the level of the flow equation the introduction of matter fields compared to pure gravity simply leads to the replacement

$$I_0[f] \to I_0[f] + P_0^M. \tag{4.28}$$

We can already observe at this point that the minimal matter fields under consideration only couple into the equation up to ρ^2. However, we would like to stress that the system will still be subject to corrections beyond the ρ^2 approximation to $f(\rho)$.

4.3 Einstein-Hilbert gravity with matter

In the Einstein-Hilbert approximation to the effective average action, the beta functions including non-selfinteracting and minimally coupled matter can be given analytically. The beta functions can be found via the flow equations (4.25) and its first derivative with respect to ρ at $\rho = 0$, neglecting the influence of higher couplings and their corresponding beta functions. We present them here in the coupling basis of the cosmological constant λ and Newton's coupling g:

$$\beta_\lambda = (-2 + \eta)\,\lambda + (a_1 - \eta\,a_2)\,g \tag{4.29}$$

$$\beta_g = (2 + \eta)\,g \tag{4.30}$$

$$\eta = \frac{g\,b_1}{1 + g\,b_2}\ . \tag{4.31}$$

The fluctuation integrals a_1, a_2, b_1 and b_2 only depend on λ:

$$a_1(\lambda) = \frac{1}{4\,\pi}\left[n_S - 4\,n_D + 2\,n_M - 4 + \frac{5}{1-2\,\lambda} + \frac{1}{1-\frac{4}{3}\,\lambda}\right] \tag{4.32}$$

$$a_2(\lambda) = \frac{1}{24\,\pi}\left[\frac{5}{1-2\,\lambda} + \frac{1}{1-\frac{4}{3}\,\lambda}\right] \tag{4.33}$$

$$b_1(\lambda) = \frac{1}{6\,\pi}\left[n_S + 2\,n_D - 4\,n_M - 9 - \frac{10}{(1-2\,\lambda)^2} - \frac{5}{1-2\,\lambda} + \frac{1}{1-\frac{4}{3}\,\lambda}\right] \tag{4.34}$$

$$b_2(\lambda) = \frac{1}{12\,\pi}\left[-\frac{10}{3\,(1-2\,\lambda)^2} - \frac{5}{2\,(1-2\,\lambda)} + \frac{1}{2\,(1-\frac{4}{3}\,\lambda)}\right] . \tag{4.35}$$

At the non-trivial fixed point, the beta functions have to vanish, hence $\eta^* = -2$ for $\beta_g = 0$ and $\beta_\lambda = 0$. The fixed point for g is at

$$g^* = \frac{-2}{b_1(\lambda^*) + 2\,b_2(\lambda^*)} , \tag{4.36}$$

and depends on the fixed point location of $\lambda*$. The fixed point value λ^* is given implicitly via a solution to the equation

$$-4\,\lambda^* - 2\,\frac{a_1(\lambda^*) + 2\,a_2(\lambda^*)}{b_1(\lambda^*) + 2\,b_2(\lambda^*)}\,g = 0 . \tag{4.37}$$

For a stable gravitational interaction we require $g^* > 0$, hence at the fixed point we require

$$b_1(\lambda^*) + 2\,b_2(\lambda^*) < 0 . \tag{4.38}$$

Since the flow exhibits a singularity line at $\lambda = \frac{1}{2}$ (cf. (4.32) to (4.35)) and a physically realised RG-trajectory should pass by the Gaussian fixed point, we require $\lambda^* < \frac{1}{2}$. This implies $b_2 < 0$ and $a_2 > 0$.

Once we have a fixed point candidate, we can calculate the stability matrix M at this point. M is a 2×2 matrix:

$$M_{ij} = \left.\frac{\partial \beta_i}{\partial g_j}\right|_* \tag{4.39}$$

$$g_i = \{\lambda, g\} . \tag{4.40}$$

The eigenvalue spectrum of M yields the critical behaviour at the fixed point (cf Section 2.5).

4.3.1 Perturbation theory

An expansion of β_λ (4.29) and β_g (4.30) is made in the small coupling limit to leading order. This approximation does not account for any threshold effects, in particular poles

in the threshold functions. The resulting beta functions exhibit an interacting UV fixed point which can be given analytically

$$g^*|_{\text{perturbative}} = \frac{12\,\pi}{23 - n_S - 2\,n_D + 4\,n_M}\ , \tag{4.41}$$

$$\lambda^*|_{\text{perturbative}} = -\frac{12\,(30 - n_S + 4\,n_D - 2n_M)}{23 - n_S - 2\,n_D + 4\,n_M}\ . \tag{4.42}$$

The fixed point value of g (4.41) is positive for pure gravity. Through the introduction of matter fields, it has the potential to go into a pole and change its sign. This is due to the negative sign of the scalars and fermions. The vectors stay clear of this behaviour and exhibit a meaningful behaviour for any positive value of n_M.

At the fixed point, the stability matrix can be calculated analytically in this perturbative approximation. The eigenvalues can be read of the matrix directly as M_{21} vanishes:

$$-\theta_\lambda = -4 \tag{4.43}$$

$$-\theta_g = -2 \tag{4.44}$$

The eigenvalues do not depend on the matter content and represent the canonical scaling behaviour.

4.3.2 Non-perturbative analysis

The solution to the full Einstein-Hilbert beta functions in (4.29) and (4.30), boils down to solving an equation for λ (4.37). Assuming that we stay clear of the poles in the fluctuation integrals (cf. (4.32) to (4.35)), this is equivalent to solving a third order polynomial in λ. It can have one, two or three distinct real solutions.
In order to determine regimes and constraints of a physically meaningful fixed point solution, we follow a more pragmatic strategy. We define two functions $A(\lambda)$ and $B(\lambda)$:

$$A(\lambda) = -\frac{1}{2}\,(a_1 + 2\,a_2)\ , \tag{4.45}$$

$$B(\lambda) = \lambda\,(b_1 + 2\,b_2)\ . \tag{4.46}$$

These two functions can be used to reformulate the fixed point condition (4.37), as

$$A(\lambda^*) \stackrel{!}{=} B(\lambda^*)\ . \tag{4.47}$$

The fixed point value of λ can then be used to obtain $g*$ (4.36):

$$g^* = -2\,\frac{\lambda^*}{B(\lambda^*)}\ . \tag{4.48}$$

Since we require a positive Newton's coupling (4.48), the sign of B (and thereby A) at the crossing (4.47) has to be the opposite to that of λ^*. If the crossing occurs with the same sign, g^* would turn out negative.

We introduce now some further properties of A and B, which will prove useful in our forthcoming analysis. In the vicinity of $\lambda = \frac{1}{2}$, the poles of the threshold functions determine the asymptotic behaviour as

$$A(\lambda) \sim -\frac{1}{(1-2\,\lambda)^2} \to -\infty \tag{4.49}$$

$$B(\lambda) \sim -\frac{1}{1-2\,\lambda} \to -\infty \,. \tag{4.50}$$

In order to have a physically meaningful fixed point, A and B have to cross at least once in the interval from $-\infty$ to $1/2$ in λ (cf. (4.47)). We define

$$A_0 \equiv A(\lambda = 0) = -\frac{4 + n_S - 4\,n_D + 2\,n_M}{8\,\pi} \,, \tag{4.51}$$

$$B_0' \equiv \left.\frac{\partial B}{\partial \lambda}\right|_{\lambda=0} = \frac{-\frac{85}{3} + n_S + 2\,n_D - 4\,n_M}{6\,\pi} \,. \tag{4.52}$$

The asymptotic behaviour (4.49) and (4.50), together with A_0 (4.51) and B_0' (4.52) provide information about the shape of the functions A and B. In contrast to the asymptotic behaviour, the shape around $\lambda = 0$ depends on the matter content. The existence of a fixed point is linked to these quantities allowing for an intersection of A and B, which leads to physically meaningful scenario.

In addition to having a mere crossing of A and B, we also require a continuous deformation of the fixed point position with respect to the number of matter fields. Thereby we promote the number of matter fields n_S, n_D, n_M to continuous parameters. As a starting point we use the well-established pure gravity fixed point (cf. Table 3.1) and require its recovery in the limit

$$n_S \to 0, \quad n_D \to 0, \quad n_M \to 0 \,. \tag{4.53}$$

This can lead to constellations where there is a fixed point candidate in the required range of λ. But it is not continuously connected to the pure gravity fixed point. The interpretation of such an occurrence depends on further details of the situation and is discussed in Section 4.4.

4.3.3 Pure gravity

The pure gravity fixed point was already studied in Chapter 3 and explicitly given in Table 3.1. Here we recall its properties and apply our terminology of A and B (cf. Section

4.3.2).

The fixed point candidate in the absence of matter fields exists at

$$\lambda^* = 0.119 \tag{4.54}$$

$$g^* = 0.943\ . \tag{4.55}$$

The fixed point condition (4.47) is plotted in Figure 4.1. The pure gravity case is characterised by

$$A_0 < 0 \tag{4.56}$$

$$B_0' < 0\ . \tag{4.57}$$

Note that A_0 starting out below $B_0 = 0$ is the crucial condition for the existence of an intersection and therefore the fixed point. The function B has a negative slope B_0' at the origin and approaches the singularity at $\lambda = 1/2$ faster than A (cf. equations (4.49) and (4.50)), so the initial ordering of A and B at $\lambda = 0$ guarantees a crossing due to the negative slope of B at the origin and the singularity. In conclusion we have two effects that work in favour of a crossing. We will later see that only one of them is necessary to ensure a crossing.

The stability matrix M can be evaluated numerically at this fixed point in order to calculate the eigenvalues $-\theta$:

$$-\theta_{0,1} = -2.411 \pm 1.947\, i\ . \tag{4.58}$$

The eigenvalues have a negative real part which means that they correspond to relevant directions. The eigenvalues constitute a complex conjugate pair. This can be a signifier for degeneracies in the theory at this level of approximation. These degeneracies might be lifted through the introduction of further pure gravity operators or through the introduction of matter fields, as we will see later.

4.3.4 Scalars

Real scalar matter enters the beta functions in the fluctuation integrals a_1 and b_1. It alters the starting points of A and B, as shown exemplary in Figure 4.1:

A_0 is moved towards more negative values (cf. equation (4.51)). The slope B_0' turns around from being negative to being increasingly positive (cf. equation (4.52)). However the ordering between A and B at $\lambda = 0$ stays the same compared to the pure gravity case. This means that the behaviour in the vicinity of the singularity at $\lambda = 1/2$ ensures

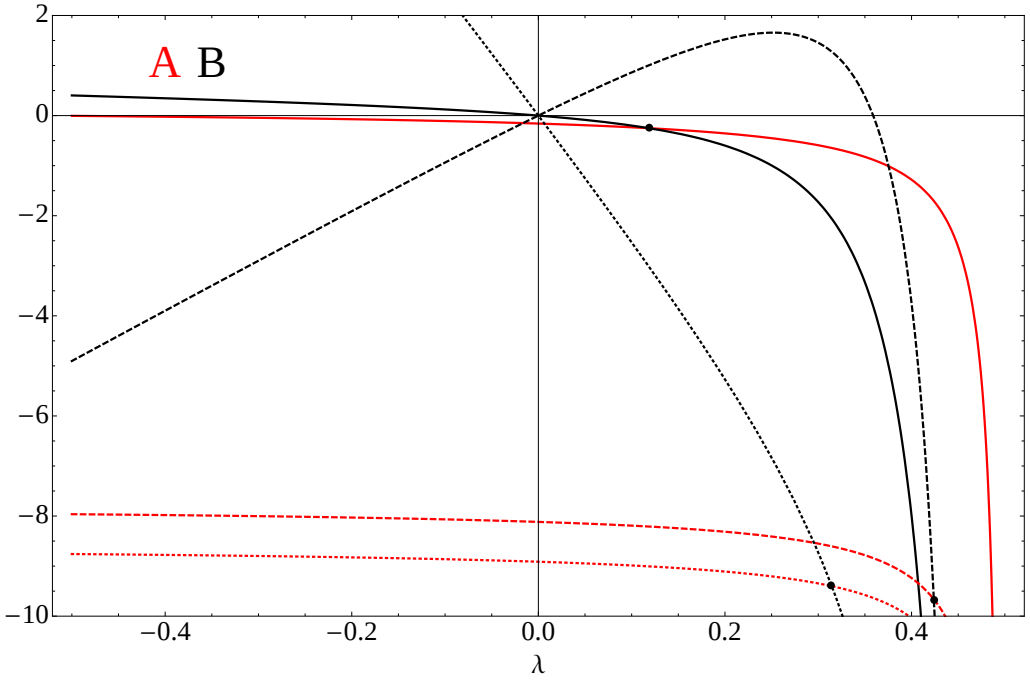

Figure 4.1: The functions $A(\lambda)$ (red) and $B(\lambda)$ (black) are plotted against λ. The solid lines represent the pure gravity case, the dashed lines represent the large n_S limit and the dotted lines represent the large n_M limit. The intersection of a black and red line of the same type denotes a fixed point candidate for the corresponding case.

a crossing and therefore a fixed point candidate.

The identified fixed point coordinates λ and g are plotted in Figure 4.9 and 4.10 . The eigenvalue spectrum is given in Figure 4.2.

The limit of

$$n_S \to \infty \tag{4.59}$$

neglects the graviton fluctuations and the RG evolution is driven through the scalar matter fields. It is characterised by

$$A_0 < 0 \tag{4.60}$$

$$B_0' > 0 \ . \tag{4.61}$$

In this limit of the fixed point can be found analytically:

$$\lambda^* = \frac{1}{2}\left(1 - \frac{4}{\sqrt{3\,n_S}}\right) + \mathcal{O}\left(\frac{1}{n_S}\right) \tag{4.62}$$

$$g^* = \frac{8\,\pi}{n_S} - 24\,\frac{\sqrt{3}\,\pi}{\sqrt{n_S^3}} + \mathcal{O}\left(\frac{1}{n_S^2}\right) \ . \tag{4.63}$$

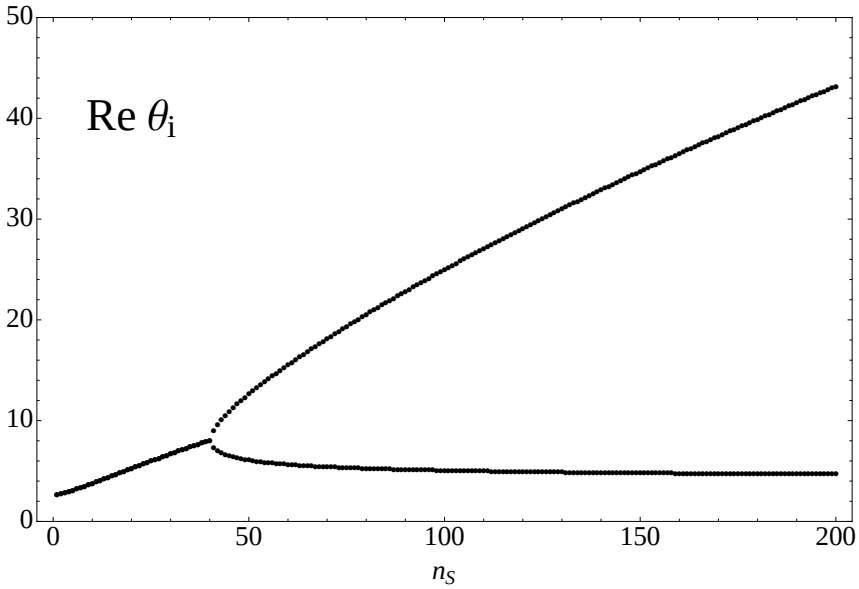

Figure 4.2: The critical exponents θ_i are plotted against the number of scalar fields n_S for the Einstein-Hilbert approximation. The complex conjugate pair bifurcates into two real critical exponents. One grows unboundedly with n_S.

The fixed point moves towards the singularity line at $\lambda = 1/2$. Strictly speaking the pole of the beta function is never reached and the flow stays finite. However, the pole is introduced into the beta functions due to gravitational fluctuations, as it is still present in the absence of matter fields(cf. (4.32) to (4.35)). This implies that, although we are in a limit of many matter fields, we still retain gravitational contributions in the flow. The situation is different in the many vector limit (cf. Section 4.3.6).

Newton's coupling g^* becomes parametically weak $\propto 1/n_S$ due to the presence of many matter fields. This is not unexpected and in fact a well-known behaviour from large N limits in QFT (review in [122]). For this reason one might expect classical scaling exponents.

In order to calculate the eigenvalues, we need the stability matrix in the limit (4.59) at the fixed point:

$$M_{11} = \left.\frac{\partial \beta_\lambda}{\partial \lambda}\right|_* = -\frac{20}{7}\sqrt{3\,n_S} + \frac{5953}{98} + \mathcal{O}\left(\frac{1}{\sqrt{n_S}}\right) \tag{4.64}$$

$$M_{12} = \left.\frac{\partial \beta_\lambda}{\partial g}\right|_* = \frac{1}{28\,\pi}\,n_S + \frac{349\,\sqrt{n_S}}{98\,\sqrt{3}\,\pi} + \mathcal{O}\,(1) \tag{4.65}$$

$$M_{21} = \left.\frac{\partial \beta_g}{\partial \lambda}\right|_* = -\frac{320\,\pi}{7}\sqrt{\frac{3}{n_S}} + \frac{52440\,\pi}{49\,n_S} + \mathcal{O}\left(\frac{1}{n_S^{3/2}}\right) \tag{4.66}$$

$$M_{22} = \left.\frac{\partial \beta_g}{\partial g}\right|_* = -\frac{24}{7} + \frac{1038\,\sqrt{3}}{49\,\sqrt{n_S}} + \mathcal{O}\left(\frac{1}{n_S}\right)\ . \tag{4.67}$$

Please note that although M_{21} goes to 0 in this limit, it is still crucial for the eigenvalues. When it enters the determinant of M, it is multiplied with M_{12} which yields a term growing with $\sqrt{n_S}$. The eigenvalues $-\theta$ are found to be:

$$-\theta_0 = -\frac{20}{7}\sqrt{3\,n_S} + \frac{6009}{98} + \mathcal{O}\left(\frac{1}{\sqrt{n_S}}\right) \tag{4.68}$$

$$-\theta_1 = -4 + \frac{7}{\sqrt{3\,n_S}} + \mathcal{O}\left(\frac{1}{n_S}\right) . \tag{4.69}$$

Both eigenvalues correspond to relevant directions. They are both real, meaning that the degeneracy of the pure gravity fixed point has been lifted. One of the eigenvalues, θ_1, is ultimately constant and approaches -4. It receives its main contribution ~ -3.4 from g (4.67). The other eigenvalue, θ_0, grows in magnitude unboundedly with $\sqrt{n_S}$. This is driven by λ (cf. (4.64)). We observe huge quantum corrections in this direction. We consider this to be an indicator towards the limit of validity of our approximation method. Essentially the fixed point in this limit is controlled by the singularity at $\lambda = 1/2$, and the large eigenvalue might be a remnant of this. We think that further studies are needed to clarify the nature of this singularity line and its impact on the large n_S fixed point.

4.3.5 Fermions

The introduction of fermions can change the hierarchy of A and B at $\lambda = 0$ as they enter into $A(\lambda = 0)$(4.51) with the opposite sign than the scalar and vector fields. Depending on the slope of B, this can lead to the absence of crossing of A and B and therefore the vanishing of a fixed point candidate.

There are two scenarios in the purely fermionic case that still allow for a fixed point candidate, namely $A_0 < 0$ and $A_0 > 0$. They are both exemplarily shown in Figure 4.3 together with the critical case that represents the boundary between the two scenarios.

The first scenario

$$A_0 < 0 \tag{4.70}$$

still preserves the ordering of A and B at $\lambda = 0$ that we know from the pure gravity case. A representative of this case is the plot of A and B for $n_D = 0.5$ in Figure 4.3. For increasing n_D, the fixed point value λ^* approaches 0. λ changes sign at $A(\lambda = 0) = B(\lambda = 0) = 0$, which occurs at $n_D = 1$. This special value for n_D is also plotted in Figure 4.3.

The second scenario

$$A_0 > 0 \tag{4.71}$$

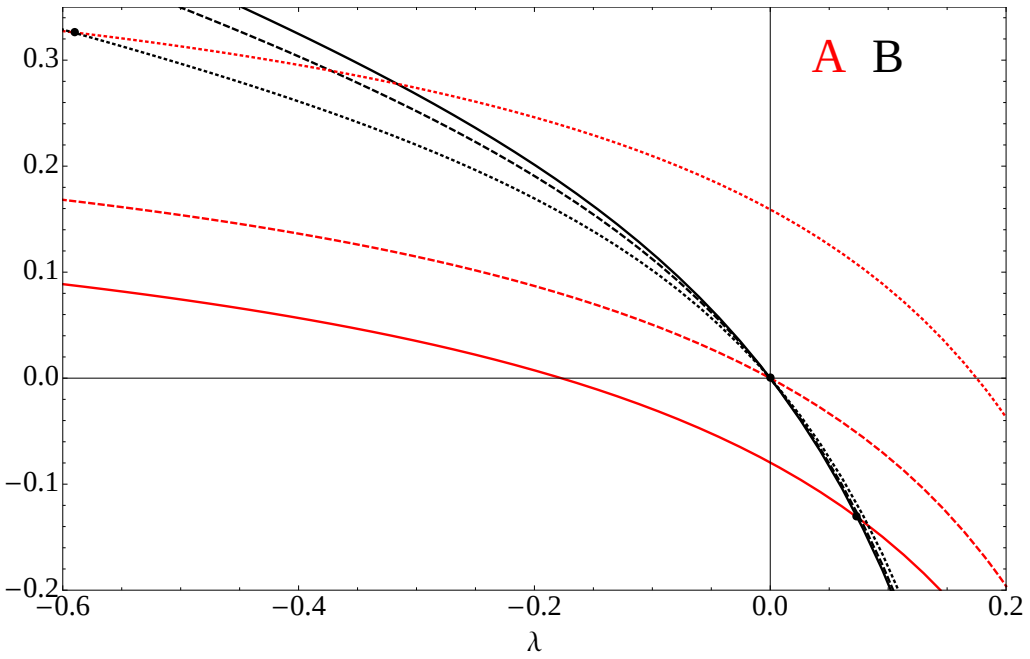

Figure 4.3: The functions $A(\lambda)$ (red) and $B(\lambda)$ (black) are plotted against λ in the purely fermionic case for different numbers of fermion fields n_D. The solid lines represent $n_D = 0.5$, the dashed lines $n_D = 1$ and the dotted lines $n_D = 2$. The intersection of a black and red line of the same type denotes a fixed point candidate for the corresponding case. With increasing n_D the fixed point moves to negative λ.

exhibits an inverted ordering between A and B at $\lambda = 0$ compared to the pure gravity case (cf. Section 4.3.3). However, there is still the possibility of a crossing at negative λ if the slope of B in the limit of $\lambda \to -\infty$ remains negative as A approaches a constant in this limit. A representative of this case is shown in Figure 4.3 at $n_D = 2$. There is an upper bound on n_D for which this scenario is still possible, as the slope of B in this limit increases with n_D:

$$n_D|_{\text{crit}} = \frac{9}{2} \, . \tag{4.72}$$

Beyond this, there is no continuously connected fixed point candidate. Thus Dirac fermions can spoil the existence of the fixed point close to pure gravity.

For the allowed range, the fixed point coordinates λ and g are plotted in Figure 4.14 and 4.15 . The eigenvalue spectrum is given in Figure 4.4.

4.3.6 Vectors

The introduction of Maxwell fields (vectors) alters the starting points of A and B, as shown exemplary in Figure 4.1:

A_0 is moved towards more negative values (cf. equation (4.51)). The slope B_0' stays

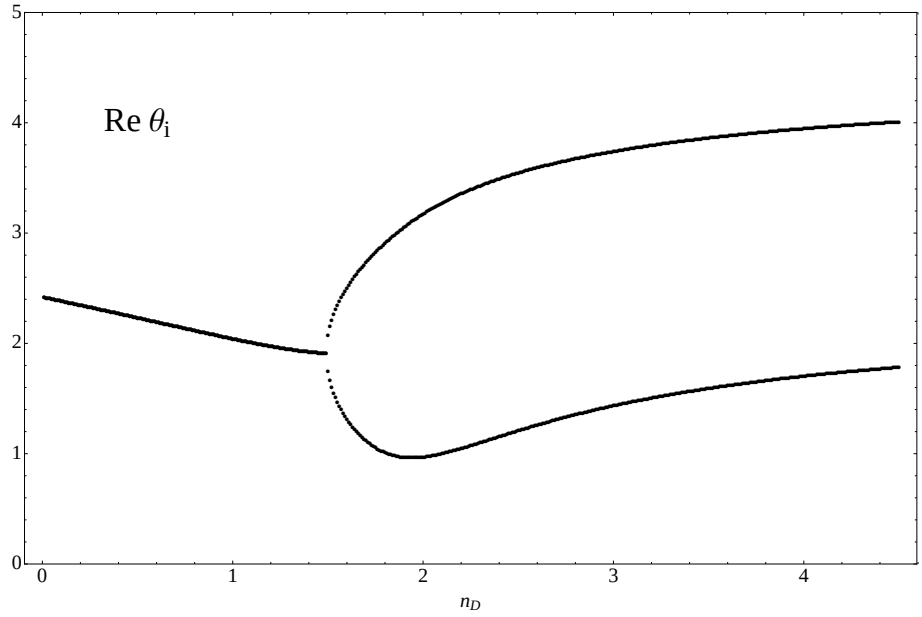

Figure 4.4: The critical exponents θ_i are plotted against the number of fermion fields n_D for the Einstein-Hilbert approximation. The complex conjugate pair splits up into two real branches. The line stops at finite $n_D = 4.5$.

negative and increases in magnitude (cf. equation (4.52)). The ordering between A and B at $\lambda = 0$ remains unchanged compared to the pure gravity case. This means that negative slope of B at the origin ensures a crossing and therefore a fixed point candidate. Please note the difference from the large n_S limit (cf. Section 4.3.4) where the singularity ensured the crossing.

A plot of the fixed point coordinates λ and g can be found in Figure 4.17 and 4.18. The critical exponents are presented in Figure 4.5.

The flow in the limit

$$n_M \to \infty \tag{4.73}$$

can be characterised by

$$A_0 < 0 \tag{4.74}$$

$$B_0' < 0\ . \tag{4.75}$$

It is dominated by the Maxwell fields and their ghosts, and gravitational contributions vanish in this limit. The fixed point candidate is found at

$$\lambda^* = \frac{3}{8} + \mathcal{O}\left(\frac{1}{n_M}\right) \tag{4.76}$$

$$g^* = \frac{3\,\pi}{n_M} + \mathcal{O}\left(\frac{1}{n_M^2}\right). \tag{4.77}$$

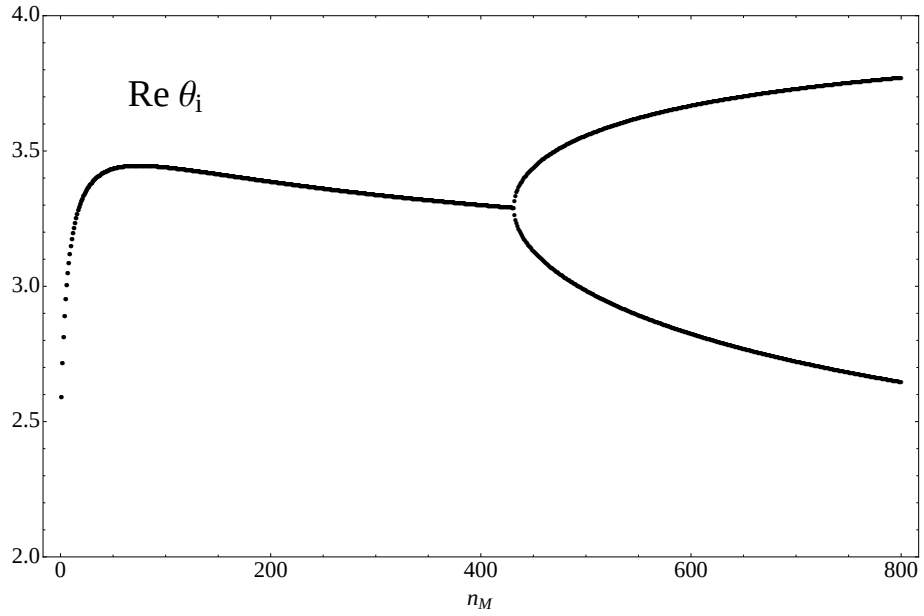

Figure 4.5: The critical exponents θ_i are plotted against the number of vector fields n_M for the Einstein-Hilbert approximation. The complex conjugate pair splits up at finite n_M. The critical exponents remain finite in the large n_M limit.

The cosmological constant approaches a constant that is generated through the presence of the vector matter fields only. It is noteworthy that it does not correspond to pole of threshold function (cf. large scalar limit in Section 4.3.4). Newton's coupling becomes small in this limit and decreases as $\propto 1/n_M$.

In order to calculate the eigenvalues, we need the stability matrix in this limit at the fixed point:

$$M_{11} = \left.\frac{\partial \beta_\lambda}{\partial \lambda}\right|_* = -4 + \mathcal{O}\left(\frac{1}{n_M}\right) \tag{4.78}$$

$$M_{12} = \left.\frac{\partial \beta_\lambda}{\partial g}\right|_* = \frac{n_M}{4\,\pi} + \mathcal{O}\left(1\right) \tag{4.79}$$

$$M_{21} = \left.\frac{\partial \beta_g}{\partial \lambda}\right|_* = -\frac{5468\,\pi}{n_M^2} + \mathcal{O}\left(\frac{1}{n_M^3}\right) \tag{4.80}$$

$$M_{22} = \left.\frac{\partial \beta_g}{\partial g}\right|_* = -2 + \mathcal{O}\left(\frac{1}{n_M}\right)\ . \tag{4.81}$$

As the off-diagonal contribution to the determinant of M decreases $\propto 1/n_M$, the eigenvalues can be read of directly and are

$$-\theta_0 = -4 + \mathcal{O}\left(\frac{1}{n_M}\right) \tag{4.82}$$

$$-\theta_1 = -2 + \mathcal{O}\left(\frac{1}{n_M}\right)\ . \tag{4.83}$$

They both correspond to relevant directions and are finite, in contrast to the unbounded growth of an eigenvalue in the large scalar limit. Furthermore they correspond to the canonical scaling exponents of the couplings. The eigenvalue $-\theta_0$ is completely controlled by λ (cf. M_{11} (4.78)) and $-\theta_1$ is completely controlled by g (cf. M_{22} (4.81)).
As this large vector limit is not influenced by potentially unphysical singularities in the flow, the results should have a higher confidence level than the large scalar limit in Section 4.3.4.

4.3.7 Interplay of different matter types

So far we have analysed scalars, fermions and vectors separately. We have found essentially three different limit cases:

- the large scalar limit (cf. Section 4.3.4)
- the fermion limit at $\lambda \to -\infty$ (cf. Section 4.3.5)
- the large vector limit (cf. Section 4.3.6)

We have to acknowledge that in a more physically realistic setup, we will encounter potentially all considered matter types at the same time, eg. in the SM. However, we will be able to translate our single matter type limits into limits that account for the interplay of the different matter fields.

Fermion bounds

The interplay of scalar and vector fields can lead to an alteration of the fermion bounds. This bound is no longer exclusively controlled by the limit $\lambda \to -\infty$, but there are two additional limits that can be characterised by a small finite λ and a finite λ approaching $1/2$.
There is a conservative bound on n_D that holds true for any number of scalars and vectors. It is characterised by $A = B = 0$ and yields

$$n_D|_{\text{crit}}^{\text{conservative}} = \frac{1}{4}\left(n_S + 2\,n_M + 4\right) \ . \tag{4.84}$$

As a first result, the presence of scalar and/or vector matter do increase the number of maximally allowed fermions in the system (cf. Figure 4.6).
The actual bound $n_D|_{\text{crit}}$ is always larger or equal than the conservative bound $n_D|_{\text{crit}}^{\text{conservative}}$.

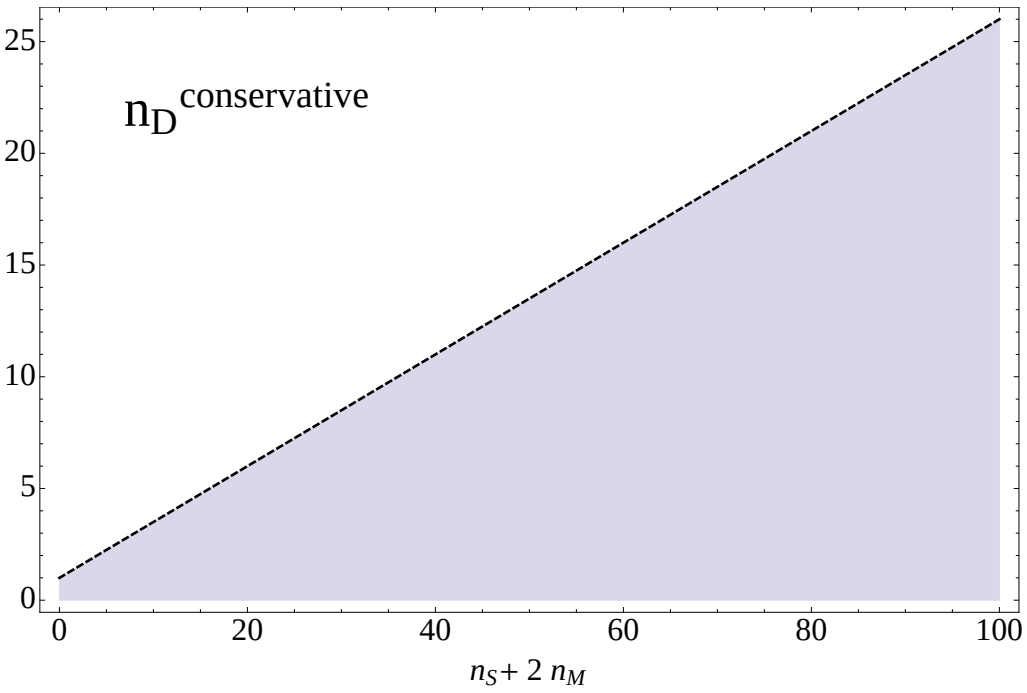

Figure 4.6: The conservative bound on n_D is given as function of $n_S + 2\,n_M$. The shaded region marks the compatible number of fermion fields for a given scalar and vector matter background. Both scalar and vector matter make room for more fermions in the system.

The difference between the two bounds is parametrised by Δ_{n_D}:

$$n_D|_{\text{crit}} = n_D|_{\text{crit}}^{\text{conservative}} + \Delta_{n_D} \tag{4.85}$$

$$\Delta_{n_D} \geq 0\ . \tag{4.86}$$

There are three distinct regimes where $n_D|_{\text{crit}}$ is controlled by different behaviours of A and B:

- The first limit is controlled by $A > 0$ at negative λ and the slope of B being negative at $\lambda \to -\infty$. The purely fermionic case already discussed falls into this limit (cf. Section 4.3.6).
- The second limit is controlled by $\partial_\lambda A$ and $\partial_\lambda B$ being equal at the bound $n_D|_{\text{crit}}$.
- The third limit is controlled by an increasingly positive slope of B at $n_D|_{\text{crit}}^{\text{conservative}}$ such that the second limit would yield an unphysical value of g^*.

A representative of each case is presented in Figure 4.7. The three cases can be discriminated via the slope B_0' at the conservative bound on n_D for a given field configuration of scalars n_S and vectors n_M. We define x to be proportional to this slope: $x = 9\,n_S - 18\,n_M - 142$ and observe that Δ_{n_D} solely depends on x It is plotted in Figure 4.8, where the different

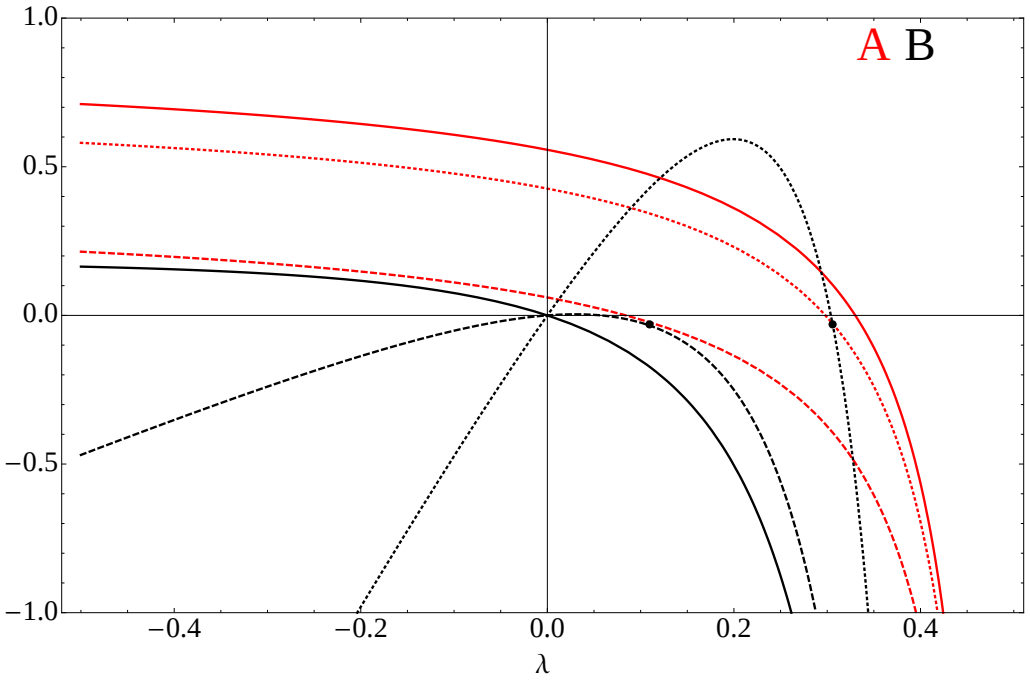

Figure 4.7: The functions $A(\lambda)$ (red) and $B(\lambda)$ (black) are plotted against λ in the fermionic case with matter interplay. We present a representative for each characteristic case at $n_D|_{\text{crit}}$: The solid line corresponds to the first ($\lambda \to -\infty$), the dashed to the second ($\partial_\lambda A = \partial_\lambda B$) and the dotted to the third case ($g \to \infty$).

origins are colour-coded. The first (second, third) limit is highlighted in blue (black, red). All limits are continuously connected, however not necessarily smoothly.

This concludes the discussion of the Einstein-Hilbert beta functions with matter. We will now examine effects of higher scalar curvature invariants.

4.4 Matter in the $f(R)$ approximation

The inclusion of further operators beyond the Einstein-Hilbert approximation may alter the behaviour of the flow. The first question is how stable our results from the Einstein-Hilbert action are against the inclusion of higher order curvature invariants.
In pure gravity (cf. Chapter 3), the marginal R^2 coupling generates an additional relevant direction of the flow (cf. Table 3.1 and Section 2.6). Going up to higher monomials in the Ricci scalar, a perturbative hierarchy was found in [39, 40, 66, 67] and chapter 3 (figures 3.3 and 3.4), meaning that the non-perturbative flow equation yields the result that the monomials R^n become less relevant with increasing mass dimension of the associated coupling. The scaling in the vicinity of the fixed point approaches classical scaling and

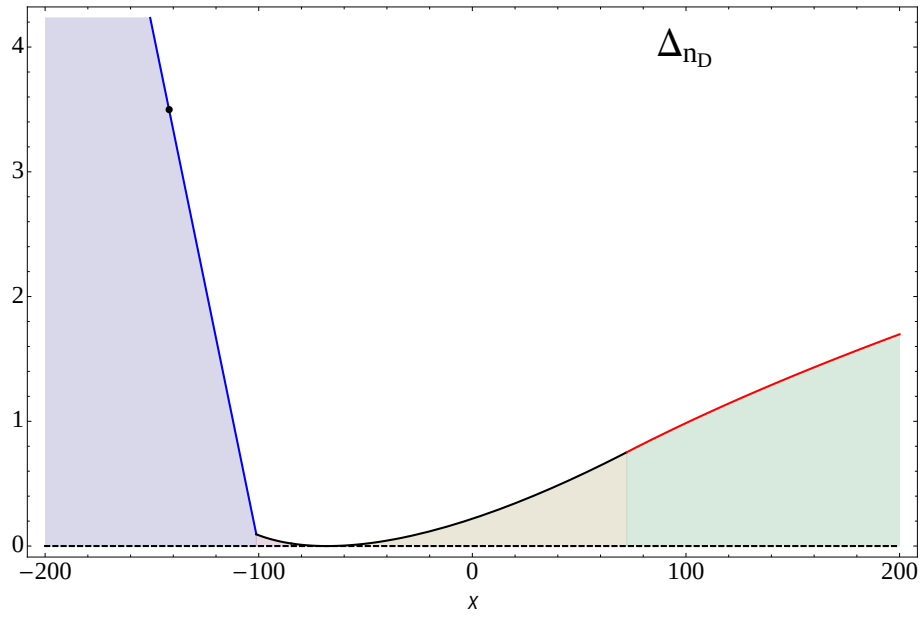

Figure 4.8: The deviation Δ_{n_D} of the bound on n_D and the conservative bound for a given matter configuration (cf. Figure 4.6) is given as function of the parameter $x = 9\,n_S - 18\,n_M - 142$. The first case is given in blue, the second in black and the third in red. The black dot marks the point of no scalar or vector fields.

quantum corrections are small.

The second question that automatically arises now is, if this holds true under the inclusion of minimally coupled matter.

We will analyse the different matter type, namely scalar (Section 4.4.2), fermionic (Section 4.4.3) and vector (Section 4.4.4) matter separately in the vicinity of the established pure gravity fixed point. In these sections we will also present tentative results regarding potential many matter limits that are not connected back to the pure gravity fixed point. We also comment on the several matter configurations (SM, MSSM, ...) and their compatibility with a gravitational UV fixed point in our treatment of $f(R)$ quantum gravity in Section 4.4.5.

4.4.1 Code

In this section we present the algorithms and code needed for examination of matter in $f(R)$ quantum gravity.

Since the flow equation (4.25) of $f(R)$ gravity with minimally coupled matter fields has the same structure as the flow equation (3.5) for pure $f(R)$ gravity, we continue to use the algorithm presented in Section 3.2. Recall that the gravitational couplings at the fixed point satisfy a recursion relation (3.26) which can be solved iteratively to yield a solution

(3.27) that depends on the two fixed point coordinates λ_0 and λ_1. Here, the matter fields introduce an additional parametric dependence on the matter field content to the recursion relation

$$\lambda_{n+2} = \tilde{X}_{n+2}(\lambda_0, \lambda_1, \ldots, \lambda_{n+1}; n_S, n_D, n_M) \tag{4.87}$$

and its solution

$$\lambda_{n+2} = X_{n+2}(\lambda_0, \lambda_1; n_S, n_D, n_M) \ . \tag{4.88}$$

For any fixed matter background, meaning that n_S, n_D and n_M attain explicit values, the couplings λ_{n+2} (4.88) are again determined via the boundary condition (3.28) for approximation order N

$$\lambda_N = 0 = \lambda_{N+1} \ . \tag{4.89}$$

The critical behaviour at the fixed point again can be derived through the stability matrix as presented in (3.33) with the underlying flow (4.25).

There are two main scenarios in which we want to analyse the fixed point behaviour with matter:

First in studies where the matter content of interest is chosen initially and we want to go to high approximation orders N. In this case the the recursion relation (4.87) looses its parametric dependence on the matter fields as they are fixed. Thereby the recursion falls back onto the same structure as in the pure gravity case (3.26). For this reason, the high performance code developed in Section 3.3 can be used with adjusted coefficients in (3.35) to account for the matter content.

Second in studies where the approximation order N is chosen initially and we want to scan over matter parameters. For each matter configuration we are interested in the whole range of potential fixed point solutions, so we can track different fixed point lines between neighbouring configurations.
For moderate approximation orders N, we can use *Mathematica* to solve the parametric recursion relation (4.87) and obtain the couplings λ_{n+2} at the fixed point, retaining their full parametric dependence (4.88). With these we can perform a scan through the desired matter configurations and look for all real solutions to the boundary condition (4.89).

Since the computations of the range of fixed point candidates at a given matter configuration during a scan are all independent from each other, this step allows for parallelisation. We developed a parallel *Mathematica* code that can be executed on the University of Sussex high performance cluster *apollo*. It computes λ_N and λ_{N+1} for a given approximation order N, retaining its parametric dependence on the matter fields (4.88) (not parallelised), and then scans through a range of matter configurations to compute the full set of fixed point candidates for each (parallelised).
The runtime and performance of this code highly depends on the approximation order N and the number of matter configurations analysed. A fast scenario is $N = 3$ with 1000 matter configurations which, if executed on 40 nodes, will have a runtime of a couple of minutes and a parallelisation factor of merely ~ 3. However, the same study in $N = 6$ will take several days up to a week and exhibit a parallelisation factor of ~ 30.

4.4.2 Scalars

On top of the Einstein-Hilbert approximation, scalar matter is analysed for the R^2, R^3, R^4 and R^5 approximation. This tests the stability of the results under inclusion of further scalar curvature operators.

In Figures 4.9 and 4.10, the dependence of the fixed point value of the cosmological constant λ and Newton's coupling g is given as a function of the number of scalar fields n_S for all analysed approximations. They show that the qualitative coupling behaviour of the Einstein-Hilbert approximation is conserved for the considered $f(R)$ approximations (cf. Section 4.3.4). The cosmological constant approaches a constant $1/2$, which corresponds to a pole in the flow and Newton's coupling becomes small $\sim 1/n_S$. It is also noteworthy that quantitatively the highest approximation orders, namely R^4 and R^5, exhibit only minor differences. This is consistent with observation of a convergence pattern in the couplings over the approximation orders for pure $f(R)$ gravity (cf. Chapter 3). Studies beyond approximation order R^5 will be able to provide further insight into a possible convergence pattern.

The eigenvalues (critical exponents) undergo a qualitative change with the inclusion of the R^2 operator: They get an additional relevant direction that is first introduced with the inclusion of the R^2 operator and persists for all considered higher approximation orders. This phenomenon is already known from pure gravity studies (cf. Chapter 3). An

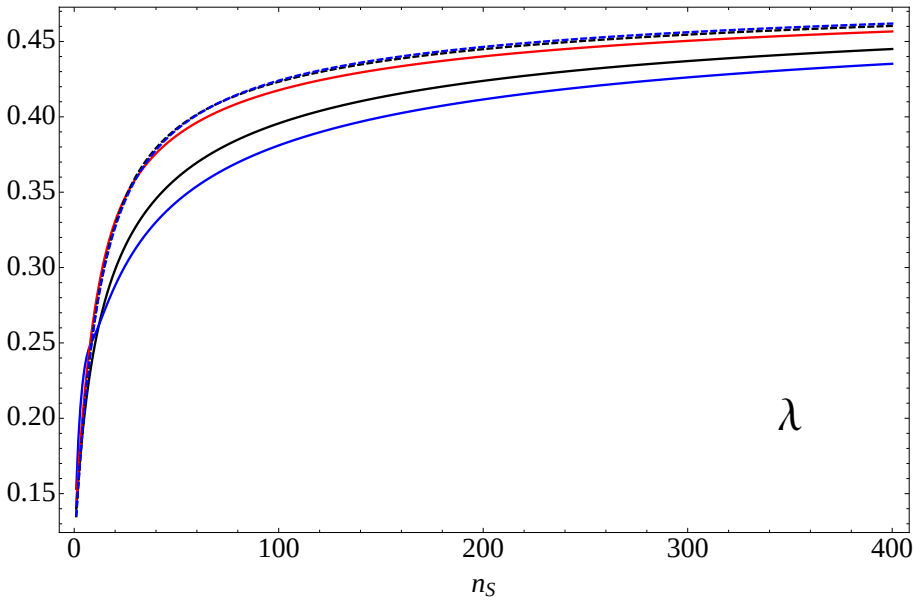

Figure 4.9: The fixed point value of the cosmological constant λ is plotted against the number of real scalar fields n_S for several approximation orders in $f(R)$, namely for approximation order R (black, solid), R^2 (blue, solid), R^3 (red, solid), R^4 (black, dashed) and R^5 (blue, dashed). They all approach $\lambda = 1/2$ in the large n_S limit.

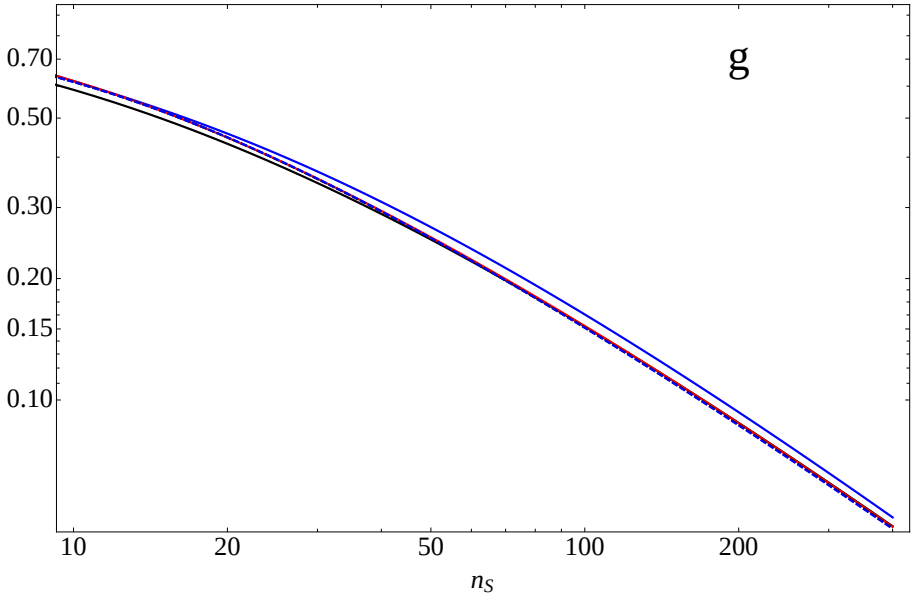

Figure 4.10: The fixed point value of Newton's coupling g is plotted against the number of real scalar fields n_S for several approximation orders in $f(R)$, namely for approximation order R (black, solid), R^2 (blue, solid), R^3 (red, solid), R^4 (black, dashed) and R^5 (blue, dashed). They all decrease eventually like $1/n_S$.

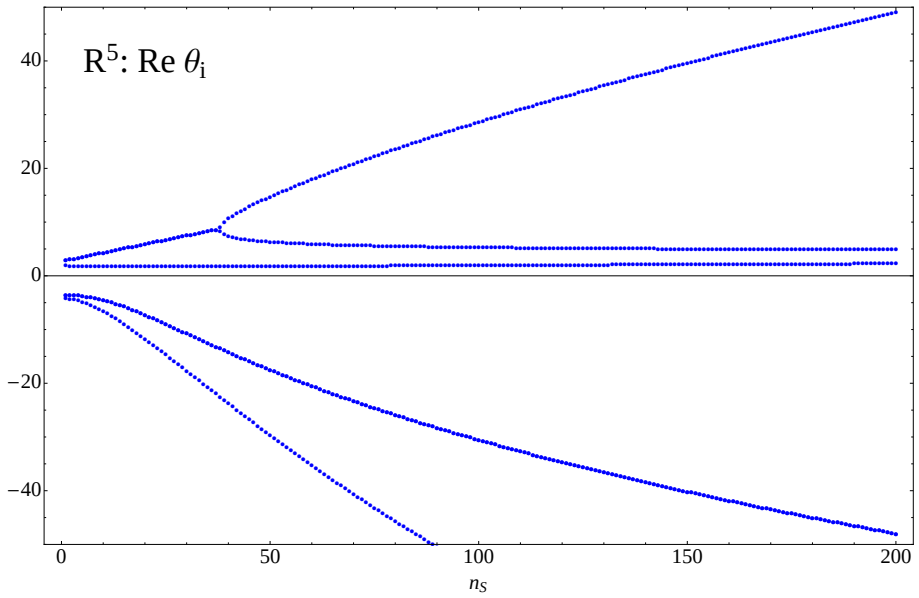

Figure 4.11: The critical exponents θ_i are plotted against the number of scalar fields n_S for the R^5 approximation. Relevant critical exponents are positive. One of the two diverging relevant exponents is clearly visible.

exemplary plot of the critical exponents θ_i is given for the R^5 approximation in Figure 4.11. The bifurcation of the originally complex conjugate pair of relevant critical exponents is visible at around $n_S \approx 37$. Two of the relevant exponents are diverging with increasing n_S. Again we consider this huge quantum correction to be a signifier for the limit of validity of our approximation. One relevant exponent seems to be approaching 4, the same as in the Einstein-Hilbert approximation (cf. Section 4.3.4).

We observed huge quantum corrections already on the level of the Einstein-Hilbert approximation. Our findings show that this picture persists in higher $f(R)$ studies. This can be interpreted as a strong hint that our approximation scheme may be insufficient to capture all the effects of many minimally coupled scalar fields to gravity in the many field limit. Improvements might be achieved either through the inclusion of further operator classes in the effective action Γ_k or through a further sophistication of the RG techniques. We would like to stress again that ultimately the large n_S behaviour is controlled by a singularity line in the flow at $\lambda = 1/2$. This has already been studied in detail for the Einstein-Hilbert approximation (cf. Section 4.3.4). It is not clear why this singularity line should be physical and therefore there might be a type of regulator to avoid it altogether. Future studies along these lines will provide further insights into the nature of this singularity and its implications on the large scalar limit.

Additionally, we observe a different many scalar limit, which is not controlled by the singularity at $\lambda = 1/2$ and always features two relevant eigendirections with canonical eigenvalues at -4 and -2, a marginal eigenvalue close to 0 (from R^2 onwards) and linearly increasing irrelevant directions (from R^3 onwards). In approximation orders beyond R^2 there can be several contesting branches which all share a fixed point location of $\lambda \to -3/4$ and a potentially unphysical $g \sim -12\,\pi/n_S$. These limits cannot be connected back to the pure gravity fixed point and stop at finite n_S. Due to the remarkable stability of this limit and the lack of any connection to a singularity in the flow, the question arises whether this limit persists in further sophistications of the RG flow, eg. running matter couplings and if g could attain positive values, possibly even downto the pure gravity fixed point.

Despite the troubles in the many scalar limit, we ascribe physical meaning to the few field limit as it arises as continuous deformation from the stable pure gravity fixed point, which has been established up to R^{70} in the polynomial $f(R)$ approximation.

The conjecture of stability of the few scalar scenario has been investigated in detail for $n_S = 4$ which corresponds to the real scalar degrees of freedom of a SM Higgs field. The a priori assumption that higher operators in the polynomial $f(R)$ approximation become less and less relevant can be tested when looking at the convergence pattern of the associated couplings. We assume that the fixed point value for all couplings at the highest approximation order N is closest to the real fixed point value. This implies that

$$n + 1 + \left(\frac{\lambda_n(N)}{\lambda_n(N_{\max})} - 1 \right) \tag{4.90}$$

should approach a constant $n + 1$ for large N if the assumption is valid.
The investigation of a setup of four real scalars has lead to a coupling convergence pattern that is presented in Figure 4.12. As visible in Figure 4.12, the low order couplings converge very quickly and become very stable. The convergence of a coupling can be destabilised by two effects. First, if the limiting value is close to 0, the relative error will be large, even for small absolute deviations. Second, after the first occurence of coupling λ_n in order $N = n + 1$, the coupling needs a couple of orders to stabilise. The fact that we use a boundary condition that forces $\lambda_{n+1} = \lambda_{n+2} = 0$ adds to this, as these boundary values are potentially far away from the fixed point values of these couplings.
The first effect can be observed for couplings λ_7 and λ_{11} . The second effect is visible for all higher order couplings in Figure 4.12.

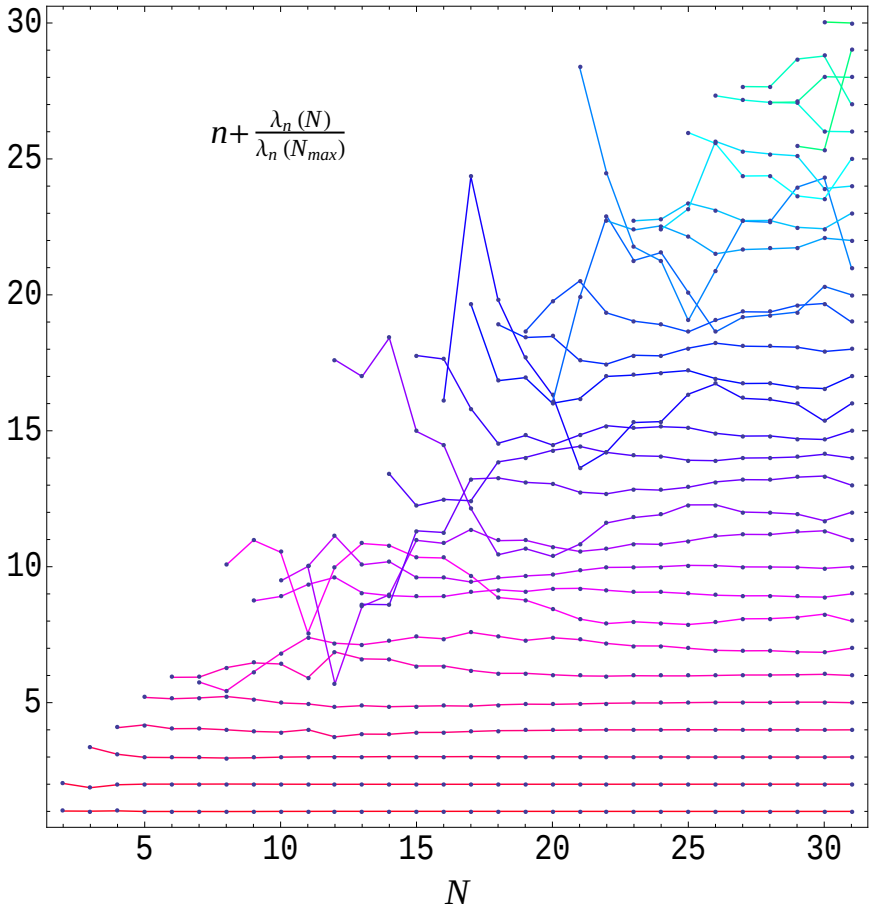

Figure 4.12: Study of four real scalar fields coupled to $f(R)$ gravity. Convergence pattern of the couplings λ_N at the fixed point at each order compared to the highest truncation order $\lambda_n(N)/\lambda_n(N_{\max}) - 1$. Top to bottom: decreasing n. All plotted lines contain an offset $n + 1$ for better visibility. The lower couplings exhibit a clear convergence pattern. The higher couplings still need further approximation orders to make their convergence clearly visible.

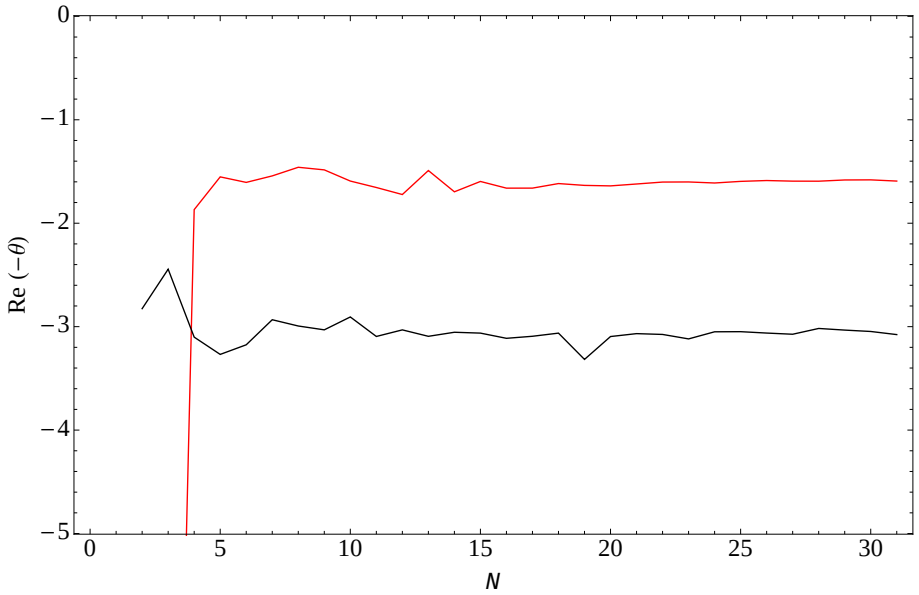

Figure 4.13: Study of four real scalar fields coupled to $f(R)$ gravity. Real part of the attractive eigenvalues against the approximation order N. The red line corresponds to a purely real eigenvalue whereas the black line corresponds to a complex conjugate pair of eigenvalues. Both lines stabilise with increasing approximation order.

We consistently observe three attractive eigendirections in this setup. Two constitute a complex conjugate pair and one is purely real. The convergence pattern of the eigenvalues $-\theta$ is shown in Figure 4.13. The eigenvalues stabilise around values of order 1.
In comparison with our studies of pure $f(R)$ gravity (cf. Section 4.3.4), we observe qualitatively the same picture with three attractive eigendirections and a stable convergence pattern over the orders. This provides further evidence for a physically meaningful few-scalar-limit.

4.4.3 Fermions

On top of the Einstein-Hilbert approximation, fermionic matter is analysed for the R^2, R^3, R^4 and R^5 approximation. The introduction of the R^2 coupling introduces a new relevant direction for the UV fixed point, which persists in all higher approximations considered.

A maximally allowed number of fermion fields $n_D|_{\text{crit}}$ continues to exist (cf. Table 4.1) close to pure gravity. This is linked to the understanding of any fixed point including matter fields as a continuous deformation of the pure gravity fixed point. If the line of fixed points ends at some n_D, either on the level of the couplings or the level of the eigenvalues, we can define a critical matter configuration. This is shown up to the R^5

approx. order	R	R^2	R^3	R^4	R^5
$n_D\|_{\text{crit}}$	4.50	3.14	1.65	1.66	1.68

Table 4.1: The maximally allowed number of fermion fields $n_D|_{\text{crit}}$ for various approximation orders.

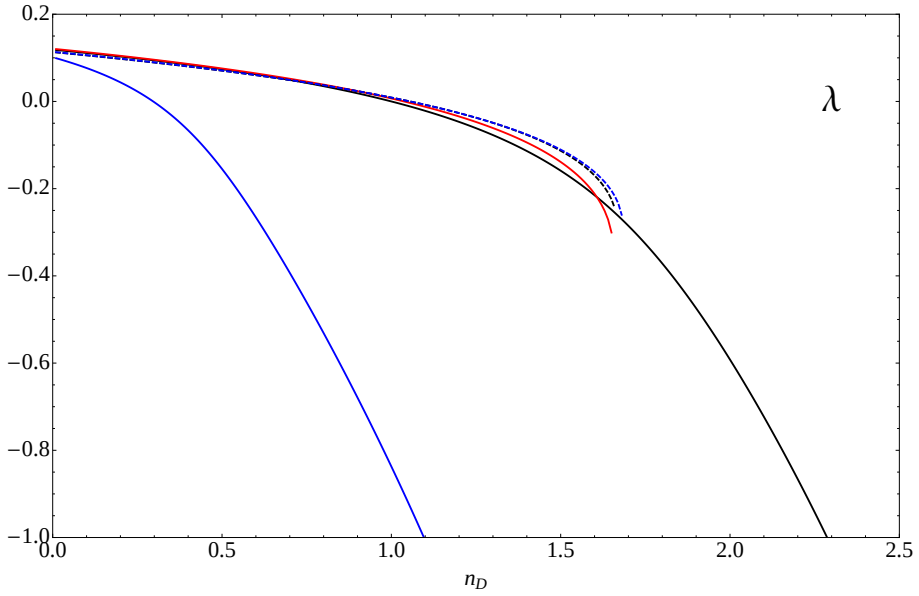

Figure 4.14: The cosmological constant λ is plotted against the number of fermion fields n_D for several approximation orders in $f(R)$, namely for approximation order R (black, solid), R^2 (blue, solid), R^3 (red, solid), R^4 (black, dashed) and R^5 (blue, dashed). From R^3 onwards the behaviour is very similar.

approximation on the level of λ (cf. Figure 4.14), g (cf. Figure 4.15) and the critical exponents θ_i, exemplarily for R^5 (cf. Figure 4.16).

It is noteworthy that the value of $n_D|_{\text{crit}}$ in Table 4.1 seems to stabilise with increasing approximation order. This is consistent with the hierarchy of operators observed in pure gravity and may be viewed as a first hint towards a similar hierarchy present at $n_D|_{\text{crit}}$ fermion fields.

Despite the finite bound on the number of fermion fields in the few fermion limit, there is the possibility of many fermion limit. In order to distinguish it from a mere artefact of the approximation order, there needs to be consistent occurrence over the orders, leading to similar fixed point locations, limiting behaviour and eigenvalue spectrum. We find the onset of such a regime from approximation order $N = 2$ (Einstein-Hilbert) onwards. It

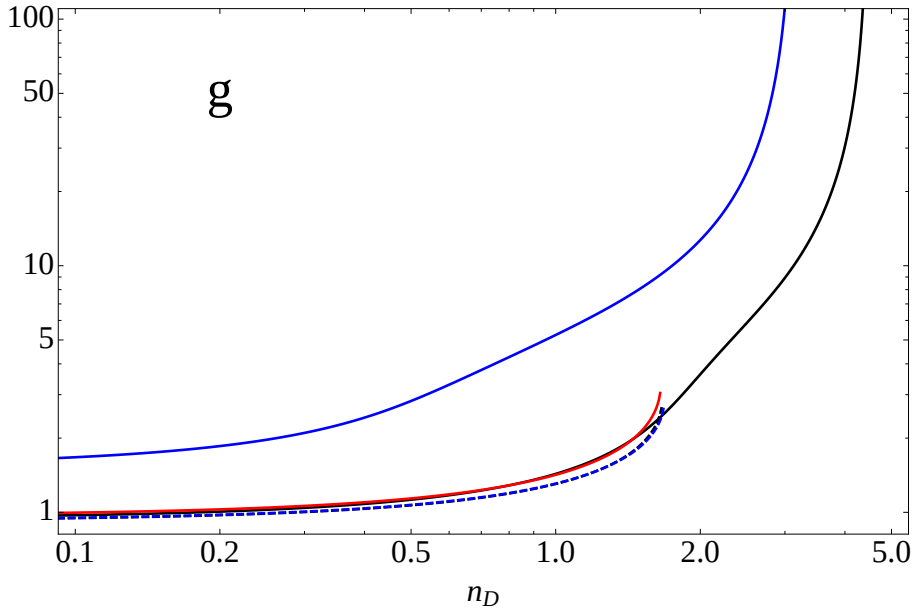

Figure 4.15: Newton's coupling g is plotted against the number of fermion fields n_D for several approximation orders in $f(R)$, namely for approximation order R (black, solid), R^2 (blue, solid), R^3 (red, solid), R^4 (black, dashed) and R^5 (blue, dashed). From R^3 onwards the behaviour is very similar.

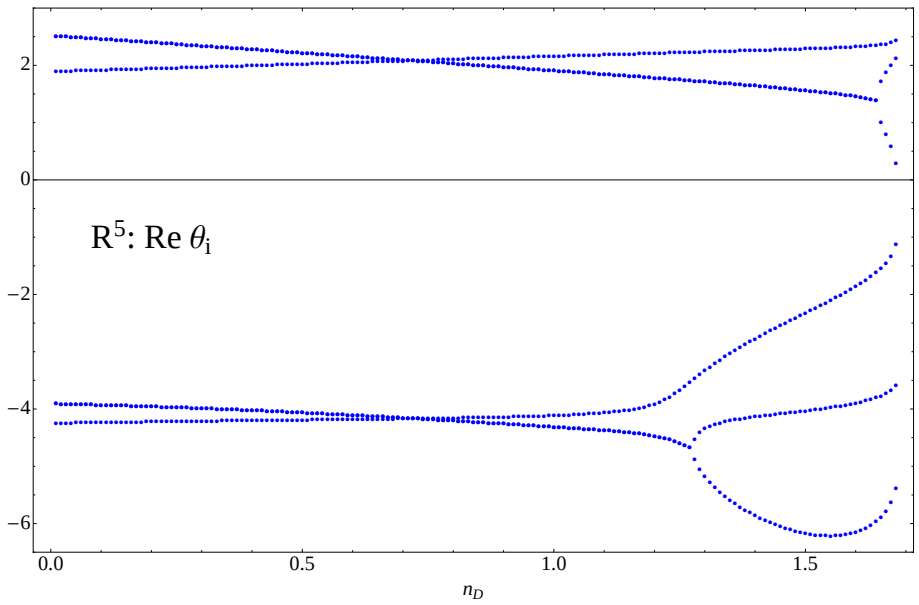

Figure 4.16: The critical exponents θ_i are plotted against the number of fermion fields n_D for the R^5 approximation. All critical exponents turned real before the bound in n_D is reached.

approx. order	R	R^2	R^3	R^4	R^5
$n_M\|_{\text{crit}}$	∞	448	191	191	164

Table 4.2: The maximally allowed number of vector fields $n_M|_{\text{crit}}$ for various approximation orders.

exhibits two relevant directions of order $\mathcal{O}(1)$ which go to the canonical eigenvalues -4 and -2. From order $N = 4$ onwards, there is also a marginal direction which exhibits a critical exponent close to 0. With increasing approximation order there can be several candidate branches featuring both signs for the marginal direction. These branches all share a fixed point candidate with a finite $\lambda \to 3/2$ and a potentially unphysical $g \sim -6\,\pi/n_D$. The question arises whether the negative sign of g persists in more sophisticated treatments of fermion fields, including the running of fermion couplings. It is striking to observe such a stable canonical pattern that does not seem to be connected to any singularity in the flow, and thereby fails any obvious classification as mere truncation artefact.

4.4.4 Vectors

On top of the Einstein-Hilbert approximation, Maxwell fields are analysed for the R^2, R^3, R^4 and R^5 approximation.

The R^2 operator introduces again a third relevant direction to the fixed point which persists in all higher approximations considered. The R^2 approximation is also the lowest approximation order in which an upper limit on the number of vector fields consistent with a fixed point, continuously connected to the pure gravity fixed point, can be observed. This means that the introduction of higher scalar curvature invariants beyond Einstein-Hilbert has a significant impact on the qualitative behaviour of the system that goes beyond the mere introduction of a new relevant direction at the UV fixed point.
The upper limits of allowed Maxwell fields $n_M|_{\text{crit}}$ for the range of analysed approximation orders is given in Table 4.2. The upper limit is also visible in the level of the couplings λ (cf. Figure 4.17) and g (cf. Figure 4.18). The cosmological constant stays clear of any pole in the flow for all examined approximation orders and follows the qualitative behaviour of the Einstein-Hilbert approximation, before stopping at $n_M|_{\text{crit}}$. Newton's coupling g becomes small $\propto 1/n_M$, which is again consistent with the qualitative behaviour of the Einstein-Hilbert approximation.

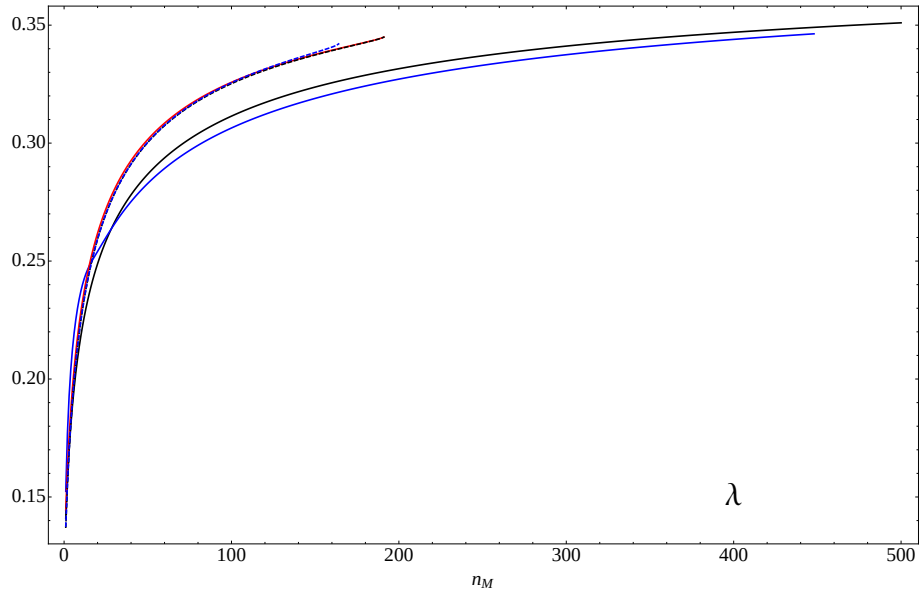

Figure 4.17: The fixed point value of the cosmological constant λ is plotted against the number of vector fields n_M for several approximation orders in $f(R)$, namely for approximation order R (black, solid), R^2 (blue, solid), R^3 (red, solid), R^4 (black, dashed) and R^5 (blue, dashed). λ never exceeds 3/8.

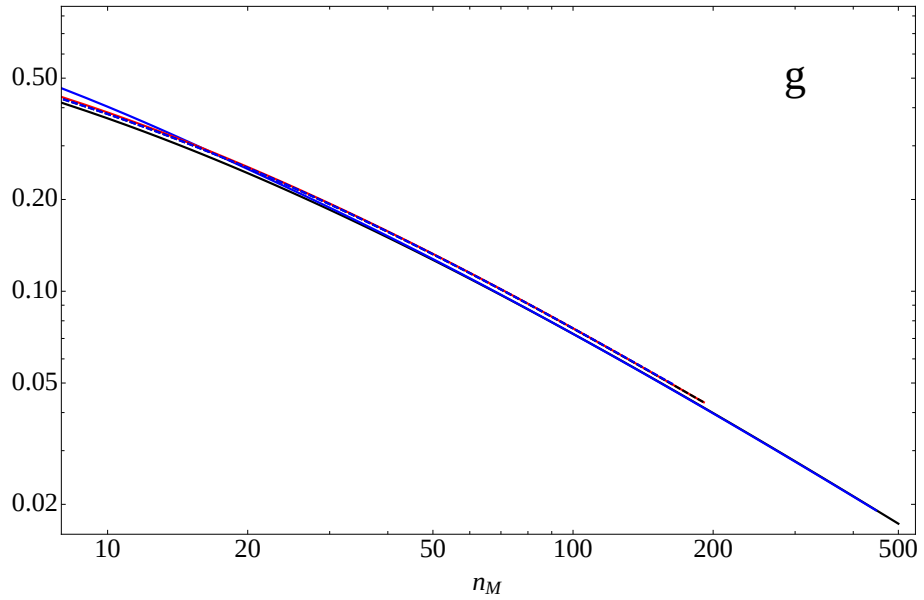

Figure 4.18: The fixed point value of Newton's coupling g is plotted against the number of vector fields n_M for several approximation orders in $f(R)$, namely for approximation order R (black, solid), R^2 (blue, solid), R^3 (red, solid), R^4 (black, dashed) and R^5 (blue, dashed). g decreases with n_M.

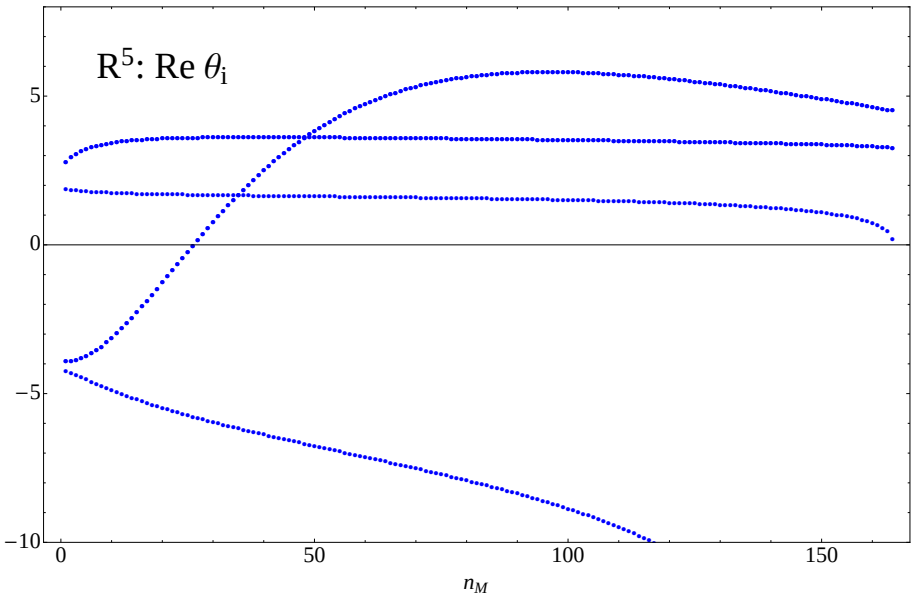

Figure 4.19: The critical exponents θ_i are plotted against the number of vector fields n_M for the R^5 approximation. An initially irrelevant critical exponent turns relevant with the presence of vector fields.

A new qualitative effect is the turning relevant of former irrelevant directions at the UV fixed point for pure gravity with increasing numbers of Maxwell fields n_M. This first occurs in the R^3 approximation, and an example is given in Figure 4.19 for the R^5 approximation where a complex conjugate pair of formerly irrelevant eigenvalues turns relevant at $n_M \approx 26$. This leads to 5 out of 6 eigenvalues being attractive in the R^5 approximation for $n_M \geq 26$.

Despite the introduction of an upper limit on the number of vector fields, there is still the possibility of a many vector limit consistent with the one observed at Einstein-Hilbert. We find two consistent limits that have the same fixed point location $\lambda \to 3/8$ and $g \to 3\,\pi/n_M$ and canonical eigenvalues as the Einstein-Hilbert approximation. These two lines can only be distinguished by their number of relevant directions, where one exhibits 2 and the other 3. They have the same magnitude for this third relevant direction $\mathcal{O}(10^{-2})$ and differ only by the sign. Due to the small magnitude, this direction can be viewed as marginal compared to others. It seems to reflect the nature of the R^2 coupling, which is marginal coupling according to canonical power counting.

This pattern has been examined until R^5. The many vector limit thereby provides a first hint that a physically meaningful many matter limit could exist, although it cannot be traced back to the pure gravity fixed point.

4.4.5 SM and beyond

The Standard Model of particle physics is the most successful description of particles and their interactions at quantum level to date. At a fundamental level its matter degrees of freedom are $n_S = 4$, $n_D = 22.5$ and $n_M = 12$ (in agreement with [52]). Here the three neutrinos are assumed to be Majorana particles and each carries 3/2 times the degrees of freedom of a Dirac fermion. This is the minimal assumption in terms of Dirac fermion degrees of freedom because otherwise the three fermions and their antiparticles will generate a larger n_D.
As we have already observed, the fermions can spoil the existence of a fixed point candidate (cf. Sections 4.3.5, 4.3.7 and 4.4.3). On the level of the Einstein-Hilbert approximation the scalars and vectors of the SM lead to a $n_D|_{\text{crit}} = 26.5$ (cf. Section 4.3.7). Although thereby the SM seems compatible with the asymptotic safety conjecture in this setup, this bound will be tightened when going to higher approximation order. It fails already at R^2. A deeper analysis up to R^{20} shows that there is no consistent fixed point pattern present over the approximation orders. Thereby this setup requires to go beyond the standard model matter content as we have shown that both scalar and vector matter can make room for further fermions in the system.

The MSSM is the minimal supersymmetric extension of the SM and features $n_S = 49$, $n_D = 30.5$ and $n_M = 12$ (in agreement with [52]). Again on the level of the Einstein-Hilbert approximation the maximum number of Dirac fermion compatible with this setup can be derived to be $n_D|_{\text{crit}} = 20.1$ (cf. Section 4.3.7). This means that the huge number of scalars in the theory does not account for the increased number of fermions and the MSSM is incompatible for this particular setup of $f(R)$ quantum gravity.

Moving towards GUT theories, we exemplarily consider two models (same matter configuration as [52]):

- SU(5) GUT: $n_S = 124$, $n_D = 24$, $n_M = 24$
- SO(10) GUT: $n_S = 97$, $n_D = 24$, $n_M = 45$.

Here it turns out that both models are compatible with this setup of asymptotic safety. The fixed point could be confirmed up to R^{20} and exhibits a stable convergence pattern.

One has to be very careful when interpreting compatibility of certain matter setups. The

exclusion of the SM is right on the verge of the fermion bound. The numerical value might be subject to quantitative changes in further approximation including different types of operators and could shift from incompatibility to compatibility.
All other models considered feature a large number of scalars. As it has been shown (cf. Section 4.3.4 and 4.4.2), this leads to a potential breakdown of the approximation. Therefore further studies are needed to clarify the behaviour.

4.5 Summary

We have studied the influence of minimally coupled scalar, fermion and vector matter on the non-Gaussian fixed point of the asymptotic safety scenario.
The analysis went beyond the previously considered Einstein-Hilbert approximation for gravity in combination with matter fields [41, 42, 43, 45, 47, 48, 50, 51, 52] and also accounted for effects due to higher scalar curvature invariants.
We examined the vicinity of the well-established pure $f(R)$ gravity fixed point and determined bounds on the number of matter fields to be compatible with this understanding.

Scalar matter allows for UV- fixed point of gravity, regardless of the number of scalar matter fields. This was tested for studies including gravitational operators up to R^5. Close to pure gravity at four scalar fields, a convergence pattern in couplings and eigenvalues could be established and was tested up to R^{20}.
The many scalar limit shows the fixed point coordinate λ approaching the finite value $1/2$. This value corresponds to a pole in the beta functions, originating from gravitational contributions in the flow. Thereby parts of the gravity fluctuations are still important in the many scalar limit. It is also accompanied by a growing $\propto \sqrt{n_S}$ relevant eigenvalue, implying huge quantum corrections in the critical behaviour. These observations of a pole and a growing relevant direction in the many scalar limit are consistent with findings in [52] although they employed a different RG treatment of Einstein-Hilbert gravity [94] and accounted for matter anomalous dimensions.
It poses the question of the physical significance of this limit. An unbounded growth of quantum corrections should be treated with caution beacuse it can signify the breakdown of one or several approximation assumptions. A promising first ansatz, aiming to remove the pole structure in the gravitational beta functions via a spectrally adjusted cutoff, was presented in [123].

The fermion fields are compatible with the existence of UV- fixed point for gravity close to the pure gravity fixed point. Their influence on the gravitational couplings is strong in the sense that there is an $\mathcal{O}(1)$ bound on the number of compatible fermion fields in the absence of other matter. The bound is tightened through the introduction of higher scalar curvature operators R^2 and beyond.
Scalar and vector matter can relax the bound and make room for more fermion fields.
The vector fields allow for a gravitational UV- fixed point connected to the pure $f(R)$ gravity fixed point. The introduction of higher scalar curvature operators beyond the Einstein-Hilbert approximation is accompanied by a bound $\mathcal{O}(100)$ on the number of compatible vector fields. In addition we observe the introduction of further relevant directions with increasing number of vector fields. The amount of newly introduced relevant directions depends on the approximation order N and grows with it. It can be viewed as a hint towards a challenge of predictivity of the setup since the gravitational non-interacting fixed point may only exhibit a finite amount of relevant directions. A challenge to predictivity in the vector sector was also found in [52] although already in the Einstein-Hilbert approximation and using a different indicator.

Motivated by the recent findings of [118], we also made tentative studies exploring the possibility of many matter limits that are not necessarily connected back to a pure gravity fixed point. The physical relevance of these limits is a scenario where asymptotic safety for gravity is only realised through the presence of matter.
Although consistent many matter limits are found for scalars and fermions in approximation orders up to R^5, the question of their physical relevance still requires further examination.
A promising many matter limit is found in the vector sector for all approximation orders up to R^5. It features a cosmological constant approaching a finite value and a parametrically small Newton's coupling. Its critical behaviour exhibits two relevant eigenvalues, which attain canonical values -4 and -2 and a marginal direction. It can be viewed as a tentative hint towards physically meaningful many matter limit.

Chapter 5

Gravitational eikonal scattering and asymptotic safety

5.1 Introduction

In this chapter, we are going to examine phenomenological implications of the asymptotic safety scenario. We are interested in graviton-mediated scattering processes.
Dimensional analysis of classical gravity suggests that the relevant scale for quantum gravity is the Planck scale

$$M_P \approx 10^{18}\,\text{GeV}. \tag{5.1}$$

Unfortunately this scale (5.1) is by far out of reach for current particle accelerator technology, which can create collision energies of around $10^4\,\text{GeV}$. There might be cosmological/astrophysical processes that can realise energies of the order of M_P.
But what if the fundamental scale of gravity M_D was actually much lower than (5.1) and we had

$$M_D \ll M_P. \tag{5.2}$$

This can be realised in models with extra dimensions [57, 124], where the fundamental scale can be as low as

$$M_D \sim \mathcal{O}(1-10)\,\text{TeV}. \tag{5.3}$$

Quantum gravity effects become important at the scale M_D, and therefore they are within reach of existing particle accelerators, such as the *LHC*.
In this work, we focus on the ADD model [57] where n compact and flat extra dimensions

are introduced. The volume of the extra dimensions relates the two gravity scales (see [125] for conventions)

$$M_P^2 \sim L^n M_D^{n+2} \ . \tag{5.4}$$

Each extra dimension has the same compactification length L. In this scenario the standard model is confined to a four-dimensional hypersurface, or brane, in a $4+n$ -dimensional spacetime. Only gravity propagates in the full $4+n$ dimensional spacetime. The requirement of a TeV-sized Planck mass already constraints the number of extra dimensions that are compatible with the experimental evidence. The crucial quantity is the size of the extra dimensions which need to be small enough in order to avoid contradictions with observations in gravity and large enough to suppress the Planck mass. Therefore $n = 1$ can be safely ruled out as effects would be visible on length scales of the solar system. $n \geq 2$ is no longer in contradiction to measurements in classical gravity.

Because momentum conservation of gravitons transverse to the brane is spontaneously broken [126], one must sum over the possible Kaluza-Klein masses of internal graviton lines in Feynman diagrams. For this reason, already the tree-level graviton exchange in $n > 2$ is UV-divergent and hence sensitive to the UV-completion of gravity [58, 127].

In contrast there exists a kinematic regime of multi-graviton scattering, called the eikonal approximation, which has been argued to be insensitive to the UV completion of gravity [59, 2, 56]. It is a semiclassical approximation to elastic scattering at small angles in the sense that it has been calculated by [55] in four dimensions using a test particle in the background metric generated by another particle [128]. The amplitude remains predictive although perturbative Einstein-Hilbert gravity is non-renormalizable, underlining a sense of insensitivity to the UV-completion. The connection between the semiclassical calculation of [55] and the eikonal approximation was shown by [56].

The fact that LHC energies could even substantially exceed the gravitational scale M_D has motivated recent considerations of the eikonal approximation in this context [58, 59, 60, 61].

Our main new addition is to implement the asymptotic safety scenario [7] (see Chapter 1 and 2 for overview) for eikonal scattering. Asymptotic safety has inspired a range of work considering scattering phenomenology [129, 130, 131, 132, 62, 133, 134, 135, 136, 137, 138, 63] and black holes [139, 140, 141, 142, 143, 144, 145].

The key ingredient from asymptotic safety, for our purpose, is a wave function renormalisation factor for the graviton propagator [130, 62]. As the eikonal approximation relies on

t-channel exchange, the graviton propagators occurring have euclidean signature. Since asymptotic safety has been mainly examined in euclidean space-times, a euclidean propagator matches the studied space-time structure.

Contrary to previous claims, we will identify signatures of the employed UV-completion on the level of the eikonal phase (cf. Section 5.5) and the eikonal amplitude (cf. Section 5.6).

We start by briefly reviewing the theory of the eikonal approximation in Section 5.2, and summarise the key results obtained within the framework of large extra dimensions. Section 5.3 reviews the framework of asymptotic safety and presents our RG-improvement to the graviton propagator. Section 5.4 reviews first implications of our RG-improvement to the tree-level graviton exchange.

5.2 Gravitational scattering

The eikonal approximation is a semiclassical approximation to gravity-mediated elastic scattering amplitudes at small angles.

In order to understand its position within the phase space of gravitational scattering, we need to introduce two parameters, namely the dimensionless center of mass energy

$$\frac{E_{CM}}{M_D} \tag{5.5}$$

and the dimensionless impact parameter

$$b\, M_D \ . \tag{5.6}$$

The impact parameter b is a length scale that can be interpreted as the shortest distance between the two interacting particles. Both quantities are measured against the fundamental scale of gravity M_D.

The kinematics of a two particle scattering process can be characterised by the Mandelstam variables s and t. If the incoming particles have momenta p_1, p_2 and the outgoing particles have momenta p_3, p_4, we have

$$s = (p_1 + p_2)^2 = E_{CM}^2 \tag{5.7}$$

$$t = (p_1 - p_3)^2 = -2p_{CM}^2(1 - \cos\theta_{CM}) \tag{5.8}$$

where $E_{CM}, p_{CM}, \theta_{CM}$ are respectively the total energy, the momentum of either particle, and the scattering angle in the centre-of-mass frame. Note that t becomes small for small scattering angles θ_{CM}.

We now have the terminology to discuss the phase space of gravitational scattering:

Since we have compact extra dimensions, the basic gravitational scattering amplitude consists of a single sum over Kaluza-Klein gravitons. A representative of this tree-level process in the kinematic t-channel is given in Figure 5.1. The corresponding amplitude is called the Born amplitude. The KK tower probes the UV behaviour of gravity and for

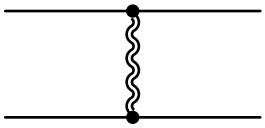

Figure 5.1: A t-channel one graviton exchange This diagram represents the Born amplitude.

this reason the Born amplitude is sensitive to the UV completion of gravity (cf. Section 5.2.1 and 5.4).

The Born amplitude will receive corrections from higher order diagrams when going to higher centre of mass energies $\sqrt{s}$ (5.7) or to smaller impact parameters b. Generically implications from details of the UV behaviour of gravity are expected to become more important for the scattering amplitude. However, there can be still regimes where semiclassical approaches remain a valid approximation. An example would be the regime where the impact parameter becomes less than the Schwarzschild radius of the two particle system and black holes are expected to form. A semiclassical treatment is expected to describe the black holes with masses much larger than the Planck scale [146, 147]. Details of quantum treatment become important when the black hole has a mass comparable to the Planck scale.

We are particularly interested in the regime of eikonal scattering, for which it has been argued in the past [59, 2, 56] that a semiclassical approximation is valid. Kinematically the regime is characterised by

$$-\frac{t}{s} \ll 1, \tag{5.9}$$

which implies small angle scattering (5.8).

The diagrams retained in this approximation contain multiple KK graviton towers. They exhibit a "ladder" and "cross-ladder" type structure. A typical diagram is displayed in Figure 5.2.

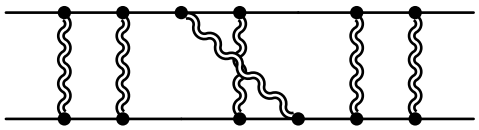

Figure 5.2: A typical ladder diagram that contributes to the eikonal amplitude. The straight lines denote the participating scattering particles. The wiggly lines represent virtual gravitons.

The eikonal amplitude is obtained via the summation over all diagrams of the type presented in Figure 5.2.

A visualisation of the discussed scattering regimes has been created by [2] and is reproduced in Figure 5.3. The diagram is made from the viewpoint of effective field theory (cf. Section 5.2.1) and "NR" denotes the non-perturbative regime which is not accessible utilising perturbative methods. The Born approximation and the eikonal approximation are separated by a critical impact parameter (blue line, cf. equation (5.17)). The dashed blue line marks the onset of model-dependent corrections to the eikonal approximation before the onset of black hole production. Black hole production occurs below the Schwarzschild radius (red line). The red dashed line "quantum limit" comes from the uncertainty principle $E\,b \approx 1$. Note that the sharp distinction between the region "NR" and the others is not perfectly clear, as our Born amplitude (cf. Section 5.4), as well as our eikonal amplitude, will turn out to have a sensitivity to the UV completion (cf. Section 5.6).

This concludes our brief review of gravitational scattering. We will now focus on an explicit implementation of the eikonal regime in effective field theory (cf. Section 5.2.1). We use the effective field theory considerations as a reference point to identify fingerprints of asymptotic safety in our treatment and argue that sensitivity to the UV-completion of gravity is retained in this case.

5.2.1 Effective field theory

In this section we give a brief review of the effective field theory results of the eikonal regime. For further details on benefits and shortcomings of the effective field theory treatment in this context see [63].

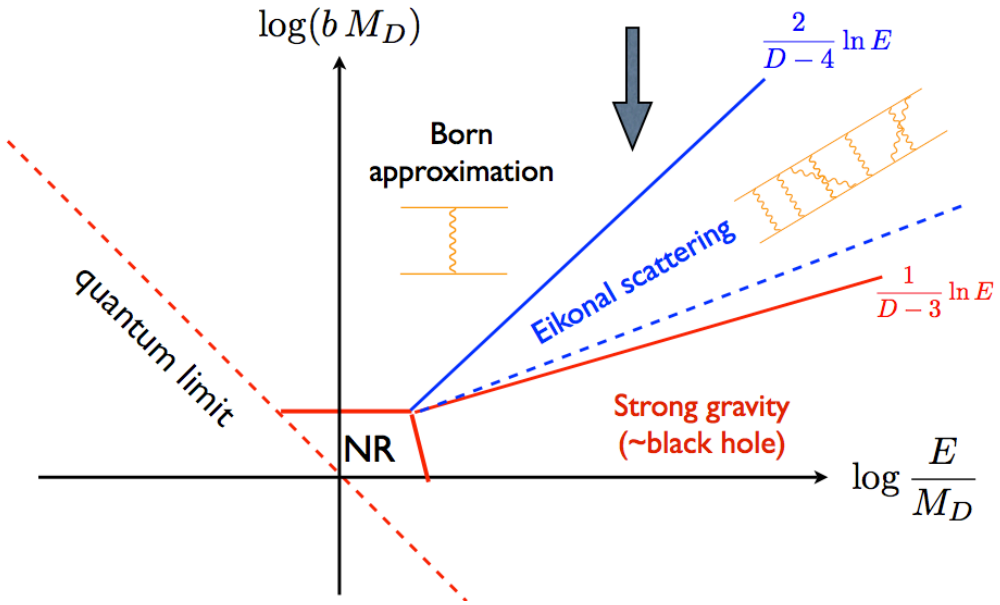

Figure 5.3: A phase diagram of different regimes of the gravitational scattering amplitude in the energy E - impact parameter b plane from the viewpoint of effective field theory, reproduced from [2]: The uncertainty principle dictates that at a given energy E only length scales above the red dashed line can be probed. NR refers to the non-perturbative regime of gravity. With decreasing impact parameter b one moves from the regime of single-graviton exchange (Born) to multi-graviton exchanges (Eikonal) and eventually to black hole formation.

In order to derive the Feynman rules of effective field theory, the Einstein-Hilbert action minimally coupled to matter is analysed for perturbations around a Minkowski background [58, 59].

Because of the universal nature of the gravitational coupling to matter, the details of the following procedure are expected to be largely independent of the spin of the matter field, and it is conventional to consider Klein-Gordan scalar fields for simplicity, ignoring any non-gravitational interactions of the matter.

The eikonal approximation requires the summation of an infinite set of "ladder" and "crossed ladder" Feynman diagrams (cf. Figure 5.2). This summation is carried out under the assumption that throughout the exchange of gravitons, the matter particles remain approximately on-shell; we are effectively in the domain of relativistic quantum mechanics. For further details see [56, 148, 149, 150].

In terms of the Mandelstam variables, the eikonal approximation is expected to be accurate up to terms of order $\mathcal{O}(-t/s)$ (5.9). This follows from the fact that a spacelike perturbative propagator carrying the full 4-momentum transferred between the two particles suppresses the diagram by a factor $\sim 1/t$, while a propagator carrying timelike momentum suppresses it by a factor $\sim 1/s$. The terms omitted from the sum of diagrams can be regarded as negligible if we restrict ourselves to scattering at small angles (cf. equation (5.8)). It is these neglected terms in which the divergences expected in quantum gravity appear. The reasoning by which such infinite terms can be regarded as "negligibly small" is that some ultimate theory of quantum gravity must smooth the divergences out. Once this has been achieved whatever finite contribution remains will be suppressed by a power of $-t/s$. This picture has been tested and confirmed in explicit theories of quantum gravity, namely supergravity [151] and extensively in string theory [152, 153, 154, 155, 156].

The starting point for evaluating the eikonal sum of diagrams is the Born amplitude $\mathcal{A}_B(s,t)$ of the theory (cf. Figure 5.1). Under the kinematic assumption that $-t/s \ll 1$ (5.9), the Born amplitude of our linearised theory is dominated by t-channel exchange. From the Feynman rules for the ADD model given in [58, 127], the leading order contribution in the limit of negligible external particle mass is found to take the form

$$\mathcal{A}_B(s,t) = \frac{s^2}{M_D^{n+2}} \int \frac{d^n m}{t - m^2} \tag{5.10}$$

In this equation the integral represents a sum over the possible KK masses of the exchanged graviton. The splitting of the energy levels in the KK tower is taken to be negligible, owing to the large compactification scales associated with the extra dimensions. In two or more

extra dimensions this integral is found to be UV divergent, and therefore requires some kind of regularisation. For $0 < n < 2$ the integral is finite, and it is found that

$$\begin{aligned}\mathcal{A}_B(s,t) &= \frac{s^2}{M_D^{n+2}} S_n \int dm \frac{m^{n-1}}{t-m^2} \\ &= -c_n \frac{s^2}{M_D^4} \left(\frac{-t}{M_D^2}\right)^{n/2-1} ,\end{aligned} \tag{5.11}$$

where

$$S_n = \frac{2\pi^{n/2}}{\Gamma(n/2)} \tag{5.12}$$

$$\text{and } c_n = \pi^{n/2}\Gamma(1-n/2) \ . \tag{5.13}$$

The Born amplitude has poles for even integers $n \geq 2$ but is otherwise well-behaved. It can be regarded as a dimensional regularization of the divergent KK sum, and we will subsequently refer to the Born amplitude (5.11) as $\mathcal{A}_{DR}(s,t)$. Note that for $n \geq 2$ this is an increasing function of momentum transfer

$$q = \sqrt{-t} \ , \tag{5.14}$$

wheras for $0 < n < 2$ where the integral converges it is a decreasing function, as would be required for forward scattering to dominate.

Once the Born term has been determined, the eikonal phase χ is defined by [59]

$$\chi(b,s) = \frac{1}{2s} \int \frac{dq}{2\,\pi}\, q\, J_0(b\,q)\, \mathcal{A}_B(s,-q^2) \ , \tag{5.15}$$

where J_0 is a Bessel function. The definition of the eikonal phase χ (5.15) formally introduces the impact parameter b (5.6), as being the conjugate length scale to the exchanged momentum q.

In this dimensional regularization ansatz (5.11), the eikonal phase (5.15) evaluates to be

$$\chi_{DR} = -\left(\frac{b_c}{b}\right)^n , \tag{5.16}$$

with the critical impact parameter

$$b_c = \left(\frac{(4\pi)^{n/2-1}\,\Gamma(n/2)\,s}{4\,M_D^2}\right)^{1/n} \frac{1}{M_D} \ . \tag{5.17}$$

The critical impact parameter (5.17) is the scale at which χ_{DR} (5.16) becomes of order one. It is also the impact parameter below which the eikonal resummation is expected to be necessary to describe elastic scattering rather than the Born approximation (cf. Figure

5.3 (blue line)).

We remark that this result for the eikonal phase (5.16) is finite for any value of n, even though it is obtained as a the result of successive integrations, each of which is only convergent for small values of n.

Another observation is that χ_{DR} (5.16) diverges as $b \to 0$. This is a reflection of the bad short distance behaviour of perturbative gravity. The eikonal phase even remains divergent in this limit when the finite width of the brane is accounted for and generates an exponential suppression of the KK excitations [60]. However the divergence is logarithmical $\propto \log(b)$ rather than a powerlaw as before (5.16).

The full eikonal amplitude is expressed in terms of the eikonal phase χ (5.15) as [59]

$$\mathcal{A}_{\rm Eik}(q,s) = -4\,\pi\,i\,s\int db\,b\,J_0(q\,b)\,(e^{i\chi(b,s)}-1)\ . \tag{5.18}$$

From the discussion above, it should be clear that the usual rationale for the eikonal approximation being independent of the UV completion of gravity no longer applies. For the case where both matter and gravity propagate freely, it is argued [2] that UV contributions are kinematically suppressed in small-angle scattering and only appear in Feynman diagrams that are suppressed by a power of $-t/s$. Here, even our starting point in the Born amplitude (5.10) is sensitive to the regulation of ultraviolet divergences.

Nevertheless the eikonal amplitude in dimensional regularisation remains finite despite the divergences in the Born amplitude (5.11) and the eikonal phase (5.16) and can be analytically expressed (initially in[157], corrected in [63]). Using the eikonal phase (5.16) we write

$$\mathcal{A}^{DR}_{\rm Eik} = -4\,\pi\,i\,s\int db\,b\,J_0(qb)\,(e^{-i\left(\frac{b_c}{b}\right)^n}-1) \tag{5.19}$$

$$\equiv 4\,\pi\,s\,b_c^2\,F_n(q\,b_c)\ , \tag{5.20}$$

It has been argued in [59] that the eikonal amplitude (5.20) retains its insensitivity to the UV completion of gravity despite the divergencies in the Born amplitude (5.10). This is because the bad short distance behaviour of gravity enters into the full eikonal amplitude (5.18) only via very rapid oscillations of the phase χ so that the small-b region makes a vanishingly small contribution to the integral (5.18). We will perform explicit calculations within the context of asymptotic safety, in which these divergences are not present, and show that the results can indeed differ significantly from the semiclassical prediction (cf. Section 5.6).

5.2.2 Born limit of the eikonal amplitude

In this section we examine the requirements of the falling back of the eikonal approximation to the Born approximation.

In the limit of a small modulus of the eikonal phase $|\chi|$ over the whole impact parameter range b range

$$|\chi(b)| < 1 \ , \tag{5.21}$$

the integral for the eikonal (5.18) amplitude can be expanded as

$$\mathcal{A}_{\text{Eik}}(q) = -4\,\pi\,i\,s \int_0^\infty db\,b\,J_0(q\,b) \sum_{k=1}^{\infty} \frac{(i\,\chi(b))^k}{k!} \ . \tag{5.22}$$

This expansion (5.22) is only meaningful if every integral of the sum is convergent on its own, as in our RG-improved setup (cf. Section 5.4). The semiclassical approximation violates this condition (cf. χ_{DR} in (5.16)).

The sum converges rapidly. An approximation to the eikonal amplitude is obtained by truncating the sum at finite $k = f$:

$$\mathcal{A}_{\text{Eik}}(q) \approx \mathcal{A}^f_{\text{Eik}} = -4\,\pi\,i\,s \int_0^\infty db\,b\,J_0(q\,b) \sum_{k=1}^{f} \frac{(i\,\chi(b))^k}{k!} \ . \tag{5.23}$$

For $f = 1$ the sum collapses to one term and the approximation just gives back the Born amplitude:

$$\mathcal{A}_{\text{Eik}}(q) \approx -4\,\pi\,i\,s \int_0^\infty db\,b\,J_0(q\,b)\,i\,\chi(b) = \mathcal{A}_{\text{Born}} \ . \tag{5.24}$$

This identity can be shown using the definition of χ as 2 dimensional Fourier transform of the Born amplitude (cf. [2]). The integral in the definition of $\mathcal{A}_{\text{Eik}}$ [2] then effectively acts as an inverse Fourier transform and gives back the original Born amplitude.

5.3 Asymptotic safety and the renormalization group

In this section, we specify the regularisation of the Born amplitude (5.10) due to asymptotic safety. We follow the implementation of asymptotic safety as a graviton propagator regularisation put forward in [130, 62]. The key observation within the asymptotic safety scenario for this application is the running of gravitational couplings (cf. Chapter 2). Here we are particularly interested in the d-dimensional Newton's coupling G_D. Newton's

coupling becomes a running coupling G, due to the functional renormalisation group (cf. Chapter 2):

$$G(\mu) = G_D \, Z^{-1}(\mu) \ , \tag{5.25}$$

where μ is a renormalisation group scale and $Z^{-1}(\mu)$ is a field strength renormalisation factor for the graviton. The field strength renormalisation encodes the information of the UV behaviour of the theory. We recall that within asymptotic safety the dimensionless couplings approach an interacting fixed point (cf. Chapter 1). The existence of a UV-fixed point in $d > 4$ dimensions, using the Einstein-Hilbert approximation, has been established in [32, 53, 54]. We remark here that in the limit of shortest distances the behaviour of compactified and infinite extra dimensions cannot be distinguished. These effects are only visible at distances at the order of the compactification length. Therefore we will be able to use the results presented in [32, 53, 54] for the UV limit in our setup:

$$Z^{-1}(\mu) = \frac{G(\mu)}{G_D} = \begin{cases} \mu \to 0 : & 1 \\ \mu \to \infty : & \mu^{2-d} \end{cases} \ . \tag{5.26}$$

The low scale behaviour in (5.26) recovers the classical limit whereas in the large scale limit we enter fixed point scaling. In $d > 2$ the fixed point scaling acts as a powerlaw suppression and this property will regularise the Born amplitude (cf. equation (5.10)).
This existence of two limits introduces a transition scale

$$\Lambda_T \tag{5.27}$$

that marks the transition from the classical regime to the fixed point regime. This transition scale is a characteristic parameter of this theory in analogy to Λ_{QCD} in quantum chromodynamics.
As the classical and quantum limit of $Z^{-1}(\mu)$ (5.26) have been identified, we can construct an explicit function to interpolate between the two regimes. The form of Z^{-1} is subject to the details of the renormalisation treatment but the physical regime (classical and quantum) have to be independent of these details. We employ a smooth interpolation between the two regimes (originally proposed in [62]):

$$Z^{-1}(\mu/\Lambda_T) = \left[1 + \left(\frac{\mu}{\Lambda_T} \right)^{n+2} \right]^{-1} \ , \tag{5.28}$$

with

$$d = 4 + n \ . \tag{5.29}$$

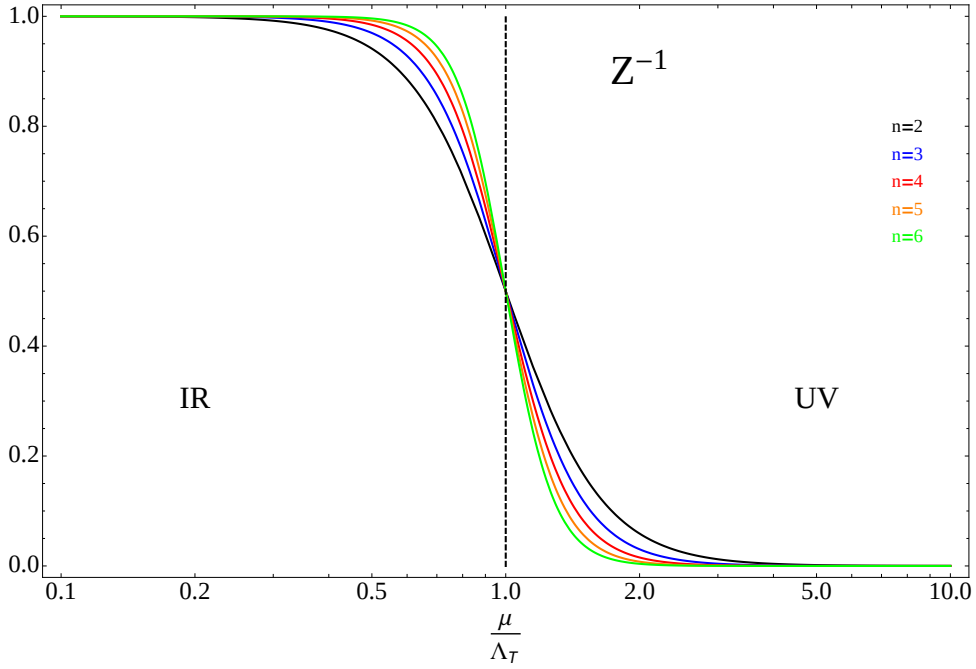

Figure 5.4: The inverse renormalisation group constant Z^{-1} is plotted against the RG scale μ for different numbers of extra dimensions: $n = 2$ (black), $n = 3$ (blue), $n = 4$ (red), $n = 5$ (orange), $n = 6$ (green). For small μ the behaviour is nearly classical. Around the transition scale Λ_T it moves into fixed point scaling.

The field strength renormalisation (5.28) is plotted for several explicit numbers of extra dimensions n in Figure 5.4.

Implementing an RG improvement necessitates making a connection between the RG scale μ and some momentum scale in our physical problem. We will take μ to be the d-dimensional graviton momentum so that

$$\mu^2 \quad = -t + m^2 = q^2 + m^2 \ , \tag{5.30}$$

where we made use of $q = \sqrt{-t}$ (5.14). There are also other scale identifications conceivable that render the KK summation finite. However, unitarity considerations suggest that the graviton momentum yields the best unitarity behaviour among the choices investigated [133, 135].

We are now in the position to study the effects of our propagator modification (5.28), motivated by the asymptotic safety scenario. We start by looking at the Born amplitude (cf. Section 5.4) and present our new findings for the eikonal phase (cf. Section 5.5) and

the eikonal amplitude (cf. Section 5.6).

5.4 Born amplitude

In this section we recall the key features of the Born amplitude with the regularisation presented in section 5.3.

Much of the work on renormalisation group improvement of the Born amplitude was already carried out for the s-channel in [62], which considered the gravitational contribution to Drell-Yan production. The full tree-level gravitational contribution to elastic scattering summed over all channels was considered in [135].

The Born amplitude (5.10) obtains a propagator renormalisation factor Z^{-1} (5.26):

$$\mathcal{A}_{RG}(s,t) = -\frac{s^2}{M_D^{n+2}} S_n \int dm \frac{m^{n-1}}{-t+m^2} Z^{-1}(\sqrt{-t+m^2}/\Lambda_T) \ . \tag{5.31}$$

Recall that for small arguments $Z^{-1}(\mu/\Lambda^T) \sim 1$, whilst for large arguments $Z^{-1}(\mu/\Lambda_T) \sim \mu^{2-d}/\Lambda_T^{2-d}$, where here d is taken to be $4+n$, as gravity propagates in the full spacetime. The RG-running of Newton's coupling renders the KK integration finite. The amplitude (5.31) attains its maximum value at $t=0$, where the KK integration becomes

$$\mathcal{A}_{RG}(s,t=0) \quad \propto \quad \Lambda_T^{n-2} \ . \tag{5.32}$$

The absolute value of the amplitude decreases monotonically with momentum transfer. For large exchanged momentum $q = \sqrt{-t} \gg \Lambda_T$ the entirety of the KK tower lies within the fixed point regime, and we find that

$$\mathcal{A}_{RG}(s, t \gg \Lambda_T^2) \propto \Lambda_T^{n-2} \left(\frac{\Lambda_T}{q}\right)^4 \ . \tag{5.33}$$

We therefore expect that the scattering will indeed be sharply peaked about the forward direction in our scheme. This can be observed in the plot of the Born amplitude in Figure 5.5, using the explicit shape of Z^{-1} (5.28). So far we have only exploited the limiting properties of our renormalisation group constant (5.26). Thus the statements are independent of the specific shape of the transition.

We will now move on to examine the eikonal phase within this setup (cf. Section 5.5).

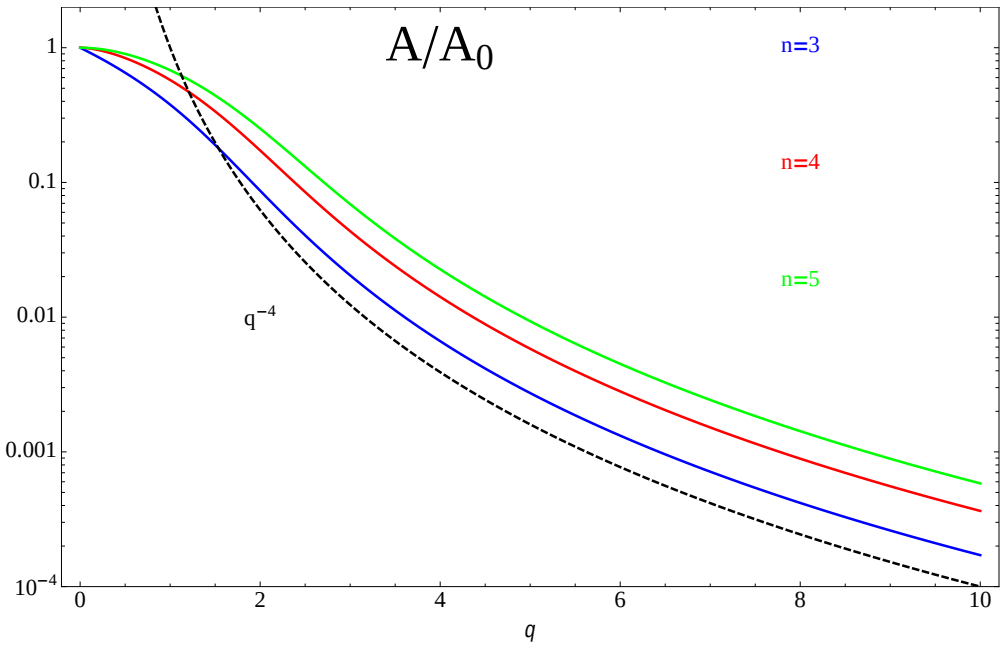

Figure 5.5: The normalised Born amplitude in the linear approximation is plotted against the exchanged momentum q for various numbers of extra dimensions n, namely $n = 3$ (blue), $n = 4$ (red) and $n = 5$ (green). All decrease eventually as $\sim q^{-4}$ (black, dashed).

5.5 Eikonal phase

In this section we consider the effects of the RG improvement (5.26) on the eikonal phase (5.15), which from the RG-modified Born amplitude (5.31) takes the form

$$\chi(b,s) = -\frac{s}{M_D^{n+2}} \frac{S_n}{4\,\pi} \int dq\, q J_0(q\,b) \int dm\, \frac{m^{n-1}}{-t+m^2}\, Z^{-1}(\sqrt{-t+m^2}/\Lambda_T)\ . \tag{5.34}$$

Because the Born amplitude (5.31) is absolutely convergent, we can legitimately exchange the orders of integration in (5.34). It is convenient to switch to polar coordinates in momentum space via the prescription $q \to \mu \sin\theta$, $m \to \mu \cos\theta$. The integral in (5.34) becomes

$$\chi(b,s) = -\frac{S_n}{4\pi} \frac{s}{M_D^{n+2}}\, b^{-n} \int_0^\infty \frac{d\mu}{\mu}\, (\mu\, b)^{n/2}\, J_{n/2}(b\,\mu)\, Z^{-1}(\mu/\Lambda_T)\ . \tag{5.35}$$

At small arguments $J_{n/2}(x)$ behaves as $\sim x^{n/2}$ in (5.35). Because of the propagator renormalisation Z^{-1} (5.28), the eikonal phase (5.35) tends to a finite constant χ_0 at vanishing impact parameter $b = 0$. The dimensionally regularised phase (5.16) exhibited an unbounded $\sim b^{-n}$ growth. The precise value of the constant χ_0 depends on the explicit shape of the propagator renormalisation (5.28). But the argument only requires the general property of all explicit approximations for $Z^{-1}(\hat{\mu})$ that it decreases for large scales $\mu/\Lambda_T \gg$

1 with μ^{-2-n} (cf. equation (5.26)). The relationship of χ_0 to the dimensionful parameters of the model is of the form

$$\chi_0 \equiv \chi(b=0,s) = -\mathcal{C}_n \frac{s}{M_D^2} \frac{\Lambda_T^n}{M_D^n}, \tag{5.36}$$

where in this approximation (5.28)

$$\mathcal{C}_n = \frac{\pi \csc\left(\frac{n\pi}{n+2}\right)}{2^{n-2}\,\Gamma^2\left(\frac{n}{2}\right)\,n\,(n+2)}\,. \tag{5.37}$$

The eikonal phase at vanishing impact parameter $b = 0$ is rendered finite in this implementation of asymptotic safety. Furthermore it exhibits a direct proportionality to the transition scale Λ_T. Thus it is sensitive to the key parameter in asymptotic safety and thereby to the UV-completion of the theory.

The eikonal phase (5.35) connects back to the previously discussed case of dimensional regularisation (5.16) via the removal of the fixed point regime which means $\Lambda_T \to \infty$.

We also recover the semi-classical limit (5.16) in (5.35) for large impact parameters $b \gg \Lambda_T^{-1}$:

$$\chi(b \gg \Lambda_T^{-1}, s) \to \chi_{\rm DR} = -\left(\frac{b_c}{b}\right)^n. \tag{5.38}$$

So we have two regimes in the eikonal phase χ (5.35): a fixed point regime at $b \ll \Lambda_T^{-1}$ and a semi-classical regime at $b \gg \Lambda_T^{-1}$. This introduces a new impact parameter

$$b_T \tag{5.39}$$

which marks the transition between the fixed point and semiclassical regime in the eikonal phase (5.35).

The new impact parameter b_T can be estimated by equating (5.36) and (5.38), leading to

$$\chi_0 \equiv -\left(\frac{b_c}{b_T}\right)^n. \tag{5.40}$$

With this definition (5.40), the impact parameter b_T signifies the point where the semi-classical approximation $\chi_{\rm DR}$ (5.16) crosses the fixed point limit χ_0 (5.36) and thereby it marks the onset of the dominance of fixed point physics over semiclassical physics. This idea is illustrated in Figure 5.6, where χ is plotted for $n = 2$.

The impact parameter b_T can be explicitly calculated from (5.40). As it involves χ_0 (5.36), its numerical n-dependent prefactor ξ_n depends on the explicit shape of Z^{-1}:

$$b_T = \xi_n\,\Lambda_T^{-1}, \tag{5.41}$$

where we use (5.28) to obtain

$$\xi_n = \sqrt[n]{\mathcal{C}_n^{-1}} = \left[\frac{2^{n-2}\,\Gamma^2\left(\frac{n}{2}\right)\,n\,(n+2)}{\pi\,\csc\left(\frac{n\,\pi}{n+2}\right)}\right]^{\frac{1}{n}} . \tag{5.42}$$

For numbers of extra dimensions n up to 15, ξ_n (5.42) can be considered $\mathcal{O}(1)$.

The ratio

$$z = \frac{b_c}{b_T} = \sqrt[n]{-\chi_0} \tag{5.43}$$

is linked to certain limits of the eikonal approximation. Recall that in the limit of $|\chi| < 1$, the eikonal amplitude is well approximated by the Born amplitude (for details see Section 5.2.2). In our case the eikonal phase χ (5.35) is bounded by χ_0 (5.36), so the general condition boils down to $|\chi_0| < 1$. Via the definition of b_T in (5.40) this further simplifies to

$$z < 1. \tag{5.44}$$

So there is a "quasi Born" regime for $b_c < b_T$, where the eikonal resummation is well-approximated by the Born amplitude.
If we require $s > M_D^2$ to be transplanckian, then also $\Lambda_T \ll M_D$ has to be satisfied to be in the "quasi Born" regime.
We also have a "strong eikonal" regime for

$$z > 1, \tag{5.45}$$

or $b_c > b_T$, where the accuracy of the eikonal resummation significantly surpasses the accuracy of the Born approximation. If we require $s > M_D^2$ to be transplanckian, then also $\Lambda_T \geq M_D$ has to be satisfied to be in the "strong eikonal" regime.
As generically

$$\Lambda_T = \mathcal{O}(M_D), \tag{5.46}$$

transplanckian scattering takes place in the strong eikonal regime.

As mentioned before, it has been argued that the ultraviolet behaviour of gravity has little quantitative effect on the eikonal amplitude [59, 2, 56]. However, here we see that the fixed point scaling serves to tame the growth of χ (5.35), such that the sensitivity of the integral to the short distance region is increased. The fixed point leaves its imprint on χ_0 (5.36) via the transition scale Λ_T.

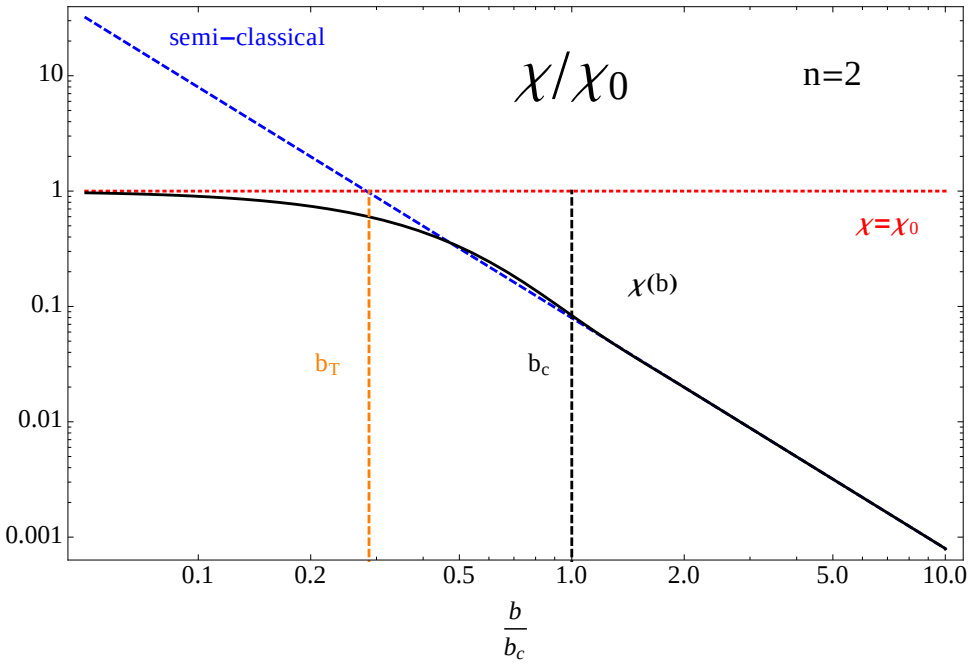

Figure 5.6: The normalized eikonal phase χ/χ_0 for the linear approximation is plotted against the b/b_c (black) in $n = 2$. The fixed point limit χ_0 (red, dotted) and the semi-classical limit (blue, dashed) intersect and thereby define b_T. It separates the fixed point from the semi-classical regime. The semi-classical scale b_c is different from b_T and larger if the eikonal corrections are to dominate over the Born approximation.

5.6 Eikonal amplitude

Here we analyse the implications of the eikonal phase (5.35) (cf. Section 5.5) on the eikonal amplitude (5.18).

First we observe that the eikonal amplitude (5.35) can be reexpressed

$$\chi(x,z) = -\frac{S_n}{4\,\pi}\,\xi_n^{n/2}\,\int_0^\infty \frac{d\hat{\mu}}{\hat{\mu}}\;(x\,z\,\hat{\mu})^{n/2}\;J_{n/2}(x\,z\,\hat{\mu}\,\xi_n)\,Z^{-1}(\hat{\mu}), \tag{5.47}$$

with ξ_n (5.42) and $\hat{\mu} = \mu/\Lambda^T$, using the dimensionless impact parameter

$$x = \frac{b}{b_c} \tag{5.48}$$

and the parameter z (5.43)

$$z = \frac{b_c}{b_T}\;. \tag{5.49}$$

Using the dimensionless exchanged momentum

$$y = q\,b_c\;, \tag{5.50}$$

and the eikonal phase (5.47), the eikonal amplitude (5.18) can be written in terms of a dimensionless function $F_n(y,z)$ which depends on two arguments now (compared to just one in the case of dimensional regularisation (5.20)):

$$\mathcal{A}_{\text{Eik}} = 4\,\pi\,s\,b_c^2\,F_n(y,z) \tag{5.51}$$

$$F_n(y,z) = \int dx\,x\,J_0(x\,y)\,(e^{i\,\chi(x,z)} - 1)\;. \tag{5.52}$$

A comparison of the dimensionless eikonal ampitude F_n (5.52) for various numbers of extra dimensions n is presented in Figure 5.7. For low transferred momenta y, the absolute value of F_n decreases with increasing number of extra dimensions n. This is due to the sharper falloff of the corresponding eikonal phase $\chi_n \propto b^{-n}$ (5.38) at large impact parameter b. In the large momentum limit a y^{-4} powerlaw is observed for this particular value of the ratio $z = 1$. This is the same powerlaw as in the Born amplitude (5.31). It can be explained as $z = 1$ is still close to the quasi Born regime. Therefore it is not a general feature of the dimensionless eikonal amplitude but depends on the value of z.

We study now the behaviour of F_n for fixed z. Exemplarily this is presented in Figure 5.8 for F_4. The value of z influences the starting value at low momenta y, as well as the shape of the decrease for large y. There are two interesting limits. The quasi Born

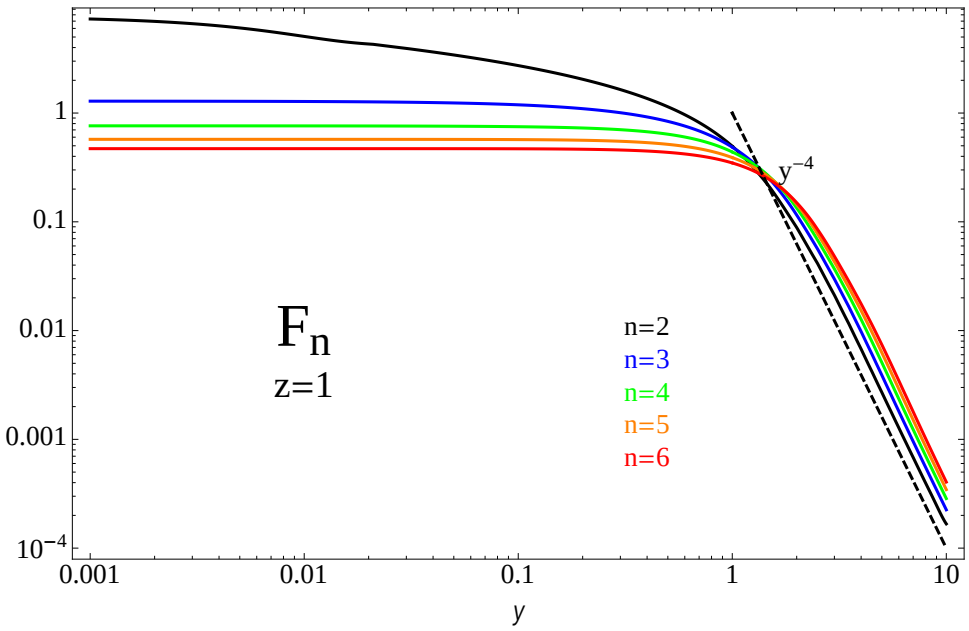

Figure 5.7: The absolute value of the dimensionless eikonal amplitude F_n in the linear approximation is given as a function of the dimensionless momentum transfer y for fixed $z = 1$. The plot compares different numbers of extra dimensions: $n = 2$ (black), $n = 3$ (blue), $n = 4$ (green), $n = 5$ (orange) and $n = 6$ (red). The large momentum limit y^{-4} is given for comparison (black, dashed).

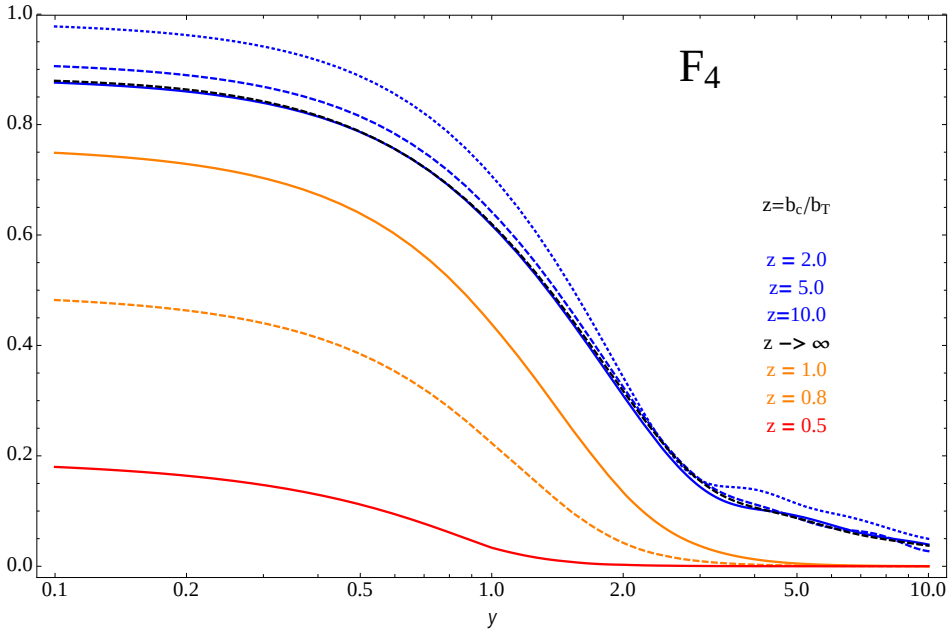

Figure 5.8: The absolute value of the dimensionless eikonal amplitude F_4 is given as a function of the dimensionless momentum transfer y for various z. For comparison the semiclassical limit of dimensional regularisation (DR, black) is given. The amplitude approaches the semiclassical limit as $z \to \infty$.

regime $z < 1$ features a powerlaw like decrease of F_n with $\sim y^{-4}$. The very strong eikonal regime ($z \to \infty$) approaches the semiclassical limit (5.20) already known from dimensional regularisation. The semiclassical limit seems to be a good approximation already at $z = 10$ (cf. Figure 5.8).

The study of F_n for fixed exchanged momentun y shows a new striking feature of this particular setup of quantum gravity. The eikonal amplitude appears to be either suppressed or enhanced compared to the semiclassical limit when scanning through the ratio z, which encodes the transition scale Λ_T(cf equations (5.43) and (5.41)). An example for this is shown for F_3 in Figure 5.9. This behaviour is strongest for low momenta y. We thereby provide strong evidence that the eikonal amplitude can be sensitive to the UV completion of gravity, contrary to previous claims [59, 2, 56].

The suppression and enhancement of the eikonal amplitude in this implementation of asymptotic safety as a UV completion of gravity could potentially be visible in scattering amplitudes at the LHC. Further work is needed to study theoretical predictions in proton - proton collisions, which means that parton distribution function and spin effects will have

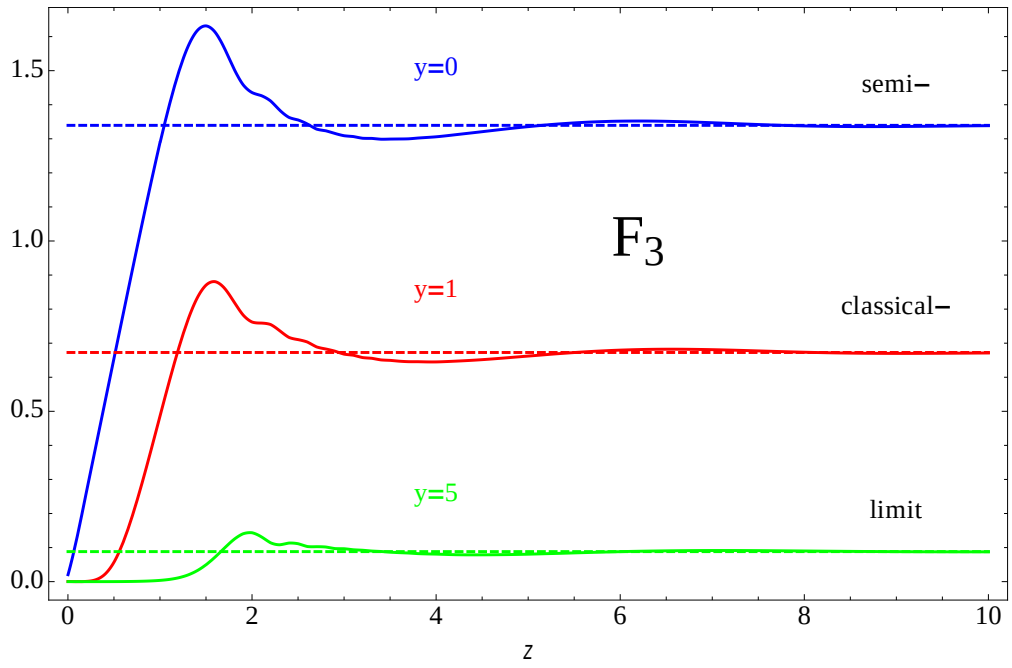

Figure 5.9: The absolute value of the dimensionless eikonal amplitude F_3 in the linear approximation is given as a function of the theory parameter z for several fixed dimensionless momentum transfer y, namely $y = 0$ (blue), $y = 1$ (red) and $y = 5$ (green). Depending on z, there can be a suppression or an enhancement of the semi-classical prediction. The semi-classical limit is recovered for large z.

to be considered. This could lead to experimentally testable predictions. First signatures of asymptotic safety at the LHC have been considered in [63].

5.7 Summary

We have examined an implementation of asymptotic safety at the level of the eikonal resummation technique for graviton scattering. Our key observation is that the UV completion of the theory is reflected in the eikonal phase χ. The limiting value χ_0 is linked to the key parameter of asymptotic safety, namely the transition scale Λ_T. Furthermore we found a transition parameter b_T that separates the eikonal phase into a fixed point and a semi-classical regime. We compared the asymptotic safety parameter b_T to the semi-classical parameter b_c and discussed the implications for eikonal resummation. We identified a "quasi-Born" and a "strong eikonal" regime.

The footprint of asymptotic safety is also visible in the eikonal amplitude, where dependent on the transferred momentum, we have an enhancement or a suppression. It is an interesting question for further research how this will translate to actual phenomenological observables for parton-parton scattering at the LHC.

Chapter 6

Conclusions

In this thesis we studied aspects of quantum gravity coupled to matter. A conservative approach was taken where we examined gravity as a quantum field theory, utilising the functional renormalisation group to gain insights into non-perturbative effects. We provided further evidence for the asymptotic safety scenario to be a strong contender for a quantum theory of gravity by considering a gravitational template action. This action consists of the essential gravitational couplings, the cosmological constant and Newton's coupling, as well as higher order terms in the Ricci curvature scalar. It can be written as a generic function $f(R)$. We reviewed the functional renormalisation group and its application to gravity in Chapter 2.

In Chapter 3, we managed to remove spurious poles in the renormalisation group flow of quantum gravity and were able to extend polynomial studies to very high orders. The results remain stable, which supports the view that the fixed point is a stable property of the theory. The resulting picture is that gravity displays a UV interacting fixed point with three relevant directions. Higher order invariants do not add new free parameters. Yet they are important quantitatively as they stabilise the renormalisation group flow. It will be interesting to identify global fixed point solutions for this new flow in the future, following the ideas of [110].

In Chapter 4, we confirmed that the minimal coupling of matter to gravity leaves the gravitational fixed point intact. Here, the effect of higher order couplings is more pronounced, leading to more substantial constraints.
Interestingly, we also found signs for new gravity-matter fixed points that are not continuously connected back to the purely gravitational fixed point. A similar pattern has

recently been observed in four dimensional Yukawa theories where an interacting UV fixed point in the gauge sector exists in perturbation theory if scalar matter is present [118, 119]. This is intriguing in its own right and deserves more studies in the future.

As a phenomenological application, in chapter 5, we studied the impact of quantum gravity effects in graviton-mediated scattering at high energies. If gravity weakens in the manner as predicted by the asymptotic safety scenario, we found that the eikonal phase at vanishing impact parameter becomes finite. This is quite intriguing and distinct from all semiclassical studies which predict at least a logarithmic or stronger divergence. However, this result is in agreement with findings from string quantum gravity [152]. In our study no inelastic contribution due to an imaginary part of the eikonal phase has arisen. It will be interesting to extend our examination to include further quantum gravity effects. This could give access to the regime where black hole formation is expected to set in.

From a broader vantage point, the research field of asymptotic safety has established a huge body of evidence for it to be realised in euclidean quantum field theory. However, there are still open challenges. The ongoing systematic study and classification of curvature operators will provide further insights into the relation of operators and fixed point existence/properties. The inclusion of more sophisticated matter setups will further clarify the role of matter to the RG running of the gravitational sector and vice versa. The goal of these studies is to understand the prerequisites for the scenario to emerge.
In the long term the euclidean results need to be carefully tested whether and how they can be translated to spacetimes with Minkowski signature. If the qualitative findings of a UV fixed with a finite amount of relevant directions hold true, the asymptotic safety scenario of gravity could become the contender of choice for a quantum theory of gravity.

Bibliography

[1] G. D. Phillips, ed., *Stanley Kubrick: Interviews*. Univ. Press of Mississippi, 2001. v

[2] S. B. Giddings, "The gravitational S-matrix: Erice lectures," arXiv:1105.2036 [hep-th]. xiv, 88, 90, 91, 92, 95, 96, 102, 106

[3] M. H. Goroff and A. Sagnotti, "Quantum Gravity at two Loops," *Phys.Lett.* **B160** (1985) 81. 1, 4

[4] G. 't Hooft and M. Veltman, "One loop divergencies in the theory of gravitation," *Annales Poincare Phys.Theor.* **A20** (1974) 69–94. 1, 3, 4

[5] J. Polchinski, *String Theory Vol I & II*. Cambridge University Press, 2008. 1

[6] C. Rovelli, *Quantum Gravity*. Cambridge University Press, 2007. 1

[7] S. Weinberg, *General Relativity: An Einstein Centenary Survey*. 1979. 2, 54, 88

[8] R. Gastmans, R. Kallosh, and C. Truffin, "Quantum Gravity Near Two-Dimensions," *Nucl.Phys.* **B133** (1978) 417. 2

[9] S. Christensen and M. Duff, "Quantum Gravity in Two + ϵ Dimensions," *Phys.Lett.* **B79** (1978) 213. 2

[10] J. F. Donoghue, "Leading quantum correction to the Newtonian potential," *Phys.Rev.Lett.* **72** (1994) 2996–2999, arXiv:gr-qc/9310024 [gr-qc]. 2

[11] C. Burgess, "Quantum gravity in everyday life: General relativity as an effective field theory," *Living Rev.Rel.* **7** (2004) 5–56, arXiv:gr-qc/0311082 [gr-qc]. 2

[12] M. Niedermaier, "The asymptotic safety scenario in quantum gravity: An introduction," *Class. Quant. Grav.* **24** (2007) R171–230, arXiv:gr-qc/0610018. 2, 10, 54

[13] K. Stelle, "Renormalization of Higher Derivative Quantum Gravity," *Phys.Rev.* **D16** (1977) 953–969. 2

[14] S. Nagy, "Lectures on renormalization and asymptotic safety," arXiv:1211.4151 [hep-th]. 2, 54

[15] M. Reuter and F. Saueressig, "Asymptotic Safety, Fractals, and Cosmology," *Lect.Notes Phys.* **863** (2013) 185–223, arXiv:1205.5431 [hep-th]. 2, 54

[16] M. Reuter and F. Saueressig, "Quantum Einstein Gravity," *New J.Phys.* **14** (2012) 055022, arXiv:1202.2274 [hep-th]. 2, 10, 54

[17] R. Percacci, "A Short introduction to asymptotic safety," arXiv:1110.6389 [hep-th]. 2, 10, 54

[18] D. F. Litim, "Renormalisation group and the Planck scale," *Phil.Trans.Roy.Soc.Lond.* **A369** (2011) 2759–2778, arXiv:1102.4624 [hep-th]. 2, 4, 54

[19] D. F. Litim, "Fixed Points of Quantum Gravity and the Renormalisation Group," *PoS* **QG-Ph** (2007) 024, arXiv:0810.3675 [hep-th]. 2, 7, 54

[20] R. Percacci, "Asymptotic Safety," arXiv:0709.3851 [hep-th]. 2, 10, 54

[21] M. Niedermaier and M. Reuter, "The asymptotic safety scenario in quantum gravity," *Living Reviews in Relativity* **9** no. 5, (2006) . 2, 10, 54

[22] C. Wetterich, "Exact evolution equation for the effective potential," *Phys.Lett.* **B301** (1993) 90–94. 2, 4, 7

[23] T. R. Morris, "The Exact renormalization group and approximate solutions," *Int.J.Mod.Phys.* **A9** (1994) 2411–2450, arXiv:hep-ph/9308265 [hep-ph]. 2, 4, 7

[24] M. Reuter, "Nonperturbative evolution equation for quantum gravity," *Phys. Rev. D* **57** no. 2, (Jan, 1998) 971–985. 2, 3, 4, 8, 9, 10

[25] K. Wilson and J. B. Kogut, "The Renormalization group and the epsilon expansion," *Phys.Rept.* **12** (1974) 75–200. 2, 4

[26] K. G. Wilson, "The Renormalization Group: Critical Phenomena and the Kondo Problem," *Rev.Mod.Phys.* **47** (1975) 773. 2, 4

[27] A. Bytsenko, L. Granda, and S. Odintsov, "Exact renormalization group and running Newtonian coupling in higher derivative gravity," *JETP Lett.* **65** (1997) 600–604, arXiv:hep-th/9705008 [hep-th]. 3

[28] L. Granda and S. Odintsov, "Effective average action and nonperturbative renormalization group equation in higher derivative quantum gravity," *Grav.Cosmol.* **4** (1998) 85–95, arXiv:gr-qc/9801026 [gr-qc]. 3

[29] O. Lauscher and M. Reuter, "Ultraviolet fixed point and generalized flow equation of quantum gravity," *Phys. Rev.* **D65** (2002) 025013, arXiv:hep-th/0108040. 3, 10

[30] O. Lauscher and M. Reuter, "Flow equation of quantum Einstein gravity in a higher- derivative truncation," *Phys. Rev.* **D66** (2002) 025026, arXiv:hep-th/0205062. 3, 10

[31] D. F. Litim, "Fixed points of quantum gravity," *Phys. Rev. Lett.* **92** (2004) 201301, arXiv:hep-th/0312114. 3, 10

[32] P. Fischer and D. F. Litim, "Fixed points of quantum gravity in extra dimensions," *Phys. Lett.* **B638** (2006) 497–502, arXiv:hep-th/0602203. 3, 10, 97

[33] A. Codello and R. Percacci, "Fixed points of higher derivative gravity," *Phys.Rev.Lett.* **97** (2006) 221301, arXiv:hep-th/0607128 [hep-th]. 3, 10, 11

[34] A. Codello, R. Percacci, and C. Rahmede, "Ultraviolet properties of f(R)-gravity," *Int. J. Mod. Phys.* **A23** (2008) 143–150, arXiv:0705.1769 [hep-th]. 3, 4, 8, 10, 11, 12, 20

[35] D. Benedetti, P. F. Machado, and F. Saueressig, "Taming perturbative divergences in asymptotically safe gravity," *Nucl. Phys.* **B824** (2010) 168–191, arXiv:0902.4630 [hep-th]. 3, 10

[36] A. Eichhorn, H. Gies, and M. M. Scherer, "Asymptotically free scalar curvature-ghost coupling in Quantum Einstein Gravity," *Phys.Rev.* **D80** (2009) 104003, arXiv:0907.1828 [hep-th]. 3, 10

[37] E. Manrique and M. Reuter, "Bimetric Truncations for Quantum Einstein Gravity and Asymptotic Safety," *Annals Phys.* **325** (2010) 785–815, arXiv:0907.2617 [gr-qc]. 3, 10

[38] A. Eichhorn, "Faddeev-Popov ghosts in quantum gravity beyond perturbation theory," *Phys.Rev.* **D87** no. 12, (2013) 124016, arXiv:1301.0632 [hep-th]. 3

[39] K. Falls, D. Litim, K. Nikolakopoulos, and C. Rahmede, "A bootstrap towards asymptotic safety," arXiv:1301.4191 [hep-th]. 3, 10, 11, 16, 19, 20, 22, 23, 24, 26, 27, 32, 37, 70

[40] K. Falls, D. F. Litim, K. Nikolakopoulos, and C. Rahmede, "Further evidence for asymptotic safety of quantum gravity," arXiv:1410.4815 [hep-th]. 3, 10, 11, 16, 19, 20, 22, 23, 24, 26, 27, 32, 37, 70

[41] D. Dou and R. Percacci, "The running gravitational couplings," *Class.Quant.Grav.* **15** (1998) 3449–3468, arXiv:hep-th/9707239 [hep-th]. 3, 10, 56, 85

[42] R. Percacci and D. Perini, "Constraints on matter from asymptotic safety," *Phys.Rev.* **D67** (2003) 081503, arXiv:hep-th/0207033 [hep-th]. 3, 10, 56, 85

[43] R. Percacci and D. Perini, "Asymptotic safety of gravity coupled to matter," *Phys.Rev.* **D68** (2003) 044018, arXiv:hep-th/0304222 [hep-th]. 3, 10, 85

[44] R. Percacci, "Further evidence for a gravitational fixed point," *Phys.Rev.* **D73** (2006) 041501, arXiv:hep-th/0511177 [hep-th]. 3, 10, 56

[45] G. Narain and R. Percacci, "Renormalization Group Flow in Scalar-Tensor Theories. I," *Class.Quant.Grav.* **27** (2010) 075001, arXiv:0911.0386 [hep-th]. 3, 10, 85

[46] G. Narain and C. Rahmede, "Renormalization Group Flow in Scalar-Tensor Theories. II," *Class.Quant.Grav.* **27** (2010) 075002, arXiv:0911.0394 [hep-th]. 3, 10

[47] A. Eichhorn and H. Gies, "Light fermions in quantum gravity," *New J.Phys.* **13** (2011) 125012, arXiv:1104.5366 [hep-th]. 3, 10, 85

[48] A. Eichhorn, "Quantum-gravity-induced matter self-interactions in the asymptotic-safety scenario," *Phys.Rev.* **D86** (2012) 105021, arXiv:1204.0965 [gr-qc]. 3, 10, 85

[49] S. Folkerts, D. F. Litim, and J. M. Pawlowski, "Asymptotic freedom of Yang-Mills theory with gravity," arXiv:1101.5552 [hep-th]. 3, 10

[50] U. Harst and M. Reuter, "QED coupled to QEG," *JHEP* **1105** (2011) 119, arXiv:1101.6007 [hep-th]. 3, 10, 85

[51] O. Zanusso, L. Zambelli, G. Vacca, and R. Percacci, "Gravitational corrections to Yukawa systems," *Phys.Lett.* **B689** (2010) 90–94, arXiv:0904.0938 [hep-th]. 3, 10, 85

[52] P. Dona, A. Eichhorn, and R. Percacci, "Matter matters in asymptotically safe quantum gravity," arXiv:1311.2898 [hep-th]. 3, 10, 54, 84, 85, 86

[53] P. Fischer and D. F. Litim, "Fixed points of quantum gravity in higher dimensions," *AIP Conf.Proc.* **861** (2006) 336–343, arXiv:hep-th/0606135 [hep-th]. 3, 10, 97

[54] D. F. Litim, "On fixed points of quantum gravity," *AIP Conf. Proc.* **841** (2006) 322–329, arXiv:hep-th/0606044. 3, 10, 97

[55] G. t Hooft, "Graviton dominance in ultra-high-energy scattering," *Physics Letters B* **198** no. 1, (1987) 61 – 63. http://www.sciencedirect.com/science/article/pii/0370269387901596. 3, 88

[56] D. N. Kabat and M. Ortiz, "Eikonal quantum gravity and Planckian scattering," *Nucl. Phys.* **B388** (1992) 570–592, arXiv:hep-th/9203082. 3, 88, 90, 93, 102, 106

[57] N. Arkani-Hamed, S. Dimopoulos, and G. R. Dvali, "The hierarchy problem and new dimensions at a millimeter," *Phys. Lett.* **B429** (1998) 263–272, arXiv:hep-ph/9803315. 3, 87

[58] G. F. Giudice, R. Rattazzi, and J. D. Wells, "Quantum gravity and extra dimensions at high-energy colliders," *Nucl. Phys.* **B544** (1999) 3–38, arXiv:hep-ph/9811291. 3, 88, 93

[59] G. F. Giudice, R. Rattazzi, and J. D. Wells, "Transplanckian collisions at the LHC and beyond," *Nucl. Phys.* **B630** (2002) 293–325, arXiv:hep-ph/0112161. 3, 88, 90, 93, 94, 95, 102, 106

[60] M. Sjodahl and G. Gustafson, "Gravitational scattering in the ADD-model at high and low energies," *Eur. Phys. J.* **C53** (2008) 109–119, arXiv:hep-ph/0608080. 3, 88, 95

[61] W. J. Stirling, E. Vryonidou, and J. D. Wells, "Eikonal regime of gravity-induced scattering at higher energy proton colliders," *Eur. Phys. J.* **C71** (2011) 1642, arXiv:1102.3844 [hep-ph]. 3, 88

[62] E. Gerwick, D. Litim, and T. Plehn, "Asymptotic safety and Kaluza-Klein gravitons at the LHC," *Phys.Rev.* **D83** (2011) 084048, arXiv:1101.5548 [hep-ph]. 3, 88, 96, 97, 99

[63] R. Old, *Asymptotic Safety And High-Energy Scattering At The Large Hadron Collider*. PhD thesis, University of Sussex, 2014. 3, 88, 91, 95, 108

[64] J. Berges, N. Tetradis, and C. Wetterich, "Non-perturbative renormalization flow in quantum field theory and statistical physics," *Phys. Rept.* **363** (2002) 223–386, arXiv:hep-ph/0005122. 4, 7

[65] H. Gies, "Introduction to the functional RG and applications to gauge theories," *Lect.Notes Phys.* **852** (2012) 287–348, arXiv:hep-ph/0611146 [hep-ph]. 4

[66] K. Falls, *Asymptotic safety and black holes*. PhD thesis, University of Sussex, 2013. http://sro.sussex.ac.uk/id/eprint/45249. 4, 19, 20, 22, 23, 24, 26, 27, 32, 37, 51, 70

[67] K. Nikolakopoulos, *Quantum Gravity and the Renormalisation Group*. PhD thesis, University of Sussex, 2013. http://sro.sussex.ac.uk/id/eprint/47448. 4, 19, 20, 22, 23, 24, 26, 27, 32, 37, 70

[68] S. Weinberg, "The Quantum theory of fields. Vol. 1: Foundations,". 4

[69] D. F. Litim, "Optimization of the exact renormalization group," *Phys.Lett.* **B486** (2000) 92–99, arXiv:hep-th/0005245 [hep-th]. 6, 7, 8, 18

[70] D. F. Litim, "Optimized renormalization group flows," *Phys.Rev.* **D64** (2001) 105007, arXiv:hep-th/0103195 [hep-th]. 6, 7, 8, 18

[71] D. F. Litim, "Mind the gap," *Int.J.Mod.Phys.* **A16** (2001) 2081–2088, arXiv:hep-th/0104221 [hep-th]. 6, 7

[72] D. F. Litim, "Critical exponents from optimized renormalization group flows," *Nucl.Phys.* **B631** (2002) 128–158, arXiv:hep-th/0203006 [hep-th]. 6, 7

[73] J. M. Pawlowski, "Aspects of the functional renormalisation group," *Annals Phys.* **322** (2007) 2831–2915, arXiv:hep-th/0512261 [hep-th]. 6, 7, 9

[74] K. Symanzik, "Small distance behavior in field theory and power counting," *Commun.Math.Phys.* **18** (1970) 227–246. 7

[75] J. Polchinski, "Renormalization and Effective Lagrangians," *Nucl.Phys.* **B231** (1984) 269–295. 7

[76] D. F. Litim, "Universality and the renormalisation group," *JHEP* **0507** (2005) 005, arXiv:hep-th/0503096 [hep-th]. 7

[77] T. R. Morris, "Equivalence of local potential approximations," *JHEP* **0507** (2005) 027, arXiv:hep-th/0503161 [hep-th]. 7

[78] C. Bervillier, A. Juttner, and D. F. Litim, "High-accuracy scaling exponents in the local potential approximation," *Nucl.Phys.* **B783** (2007) 213–226, arXiv:hep-th/0701172 [hep-th]. 7

[79] D. F. Litim and J. M. Pawlowski, "Perturbation theory and renormalization group equations," *Phys.Rev.* **D65** (2002) 081701, arXiv:hep-th/0111191 [hep-th]. 7

[80] D. F. Litim and J. M. Pawlowski, "Completeness and consistency of renormalisation group flows," *Phys.Rev.* **D66** (2002) 025030, arXiv:hep-th/0202188 [hep-th]. 7

[81] D. F. Litim and D. Zappala, "Ising exponents from the functional renormalisation group," *Phys.Rev.* **D83** (2011) 085009, arXiv:1009.1948 [hep-th]. 7

[82] R. D. Ball, P. E. Haagensen, I. Latorre, Jose, and E. Moreno, "Scheme independence and the exact renormalization group," *Phys.Lett.* **B347** (1995) 80–88, arXiv:hep-th/9411122 [hep-th]. 8

[83] D. F. Litim, "Scheme independence at first order phase transitions and the renormalization group," *Phys.Lett.* **B393** (1997) 103–109, arXiv:hep-th/9609040 [hep-th]. 8

[84] K.-I. Aoki, K. Morikawa, W. Souma, J.-I. Sumi, and H. Terao, "Rapidly converging truncation scheme of the exact renormalization group," *Prog.Theor.Phys.* **99** (1998) 451–466, arXiv:hep-th/9803056 [hep-th]. 8

[85] D. F. Litim and J. M. Pawlowski, "On gauge invariant Wilsonian flows," arXiv:hep-th/9901063 [hep-th]. 9

[86] F. Freire, D. F. Litim, and J. M. Pawlowski, "Gauge invariance and background field formalism in the exact renormalization group," *Phys.Lett.* **B495** (2000) 256–262, arXiv:hep-th/0009110 [hep-th]. 9

[87] D. F. Litim and J. M. Pawlowski, "Wilsonian flows and background fields," *Phys.Lett.* **B546** (2002) 279–286, arXiv:hep-th/0208216 [hep-th]. 9, 10

[88] E. Manrique, M. Reuter, and F. Saueressig, "Matter Induced Bimetric Actions for Gravity," *Annals Phys.* **326** (2011) 440–462, arXiv:1003.5129 [hep-th]. 10

[89] E. Manrique, M. Reuter, and F. Saueressig, "Bimetric Renormalization Group Flows in Quantum Einstein Gravity," *Annals Phys.* **326** (2011) 463–485, arXiv:1006.0099 [hep-th]. 10

[90] D. Becker and M. Reuter, "Running boundary actions, Asymptotic Safety, and black hole thermodynamics," *JHEP* **1207** (2012) 172, arXiv:1205.3583 [hep-th]. 10

[91] D. Becker and M. Reuter, "En route to Background Independence: Broken split-symmetry, and how to restore it with bi-metric average actions," *Annals Phys.* **350** (2014) 225–301, arXiv:1404.4537 [hep-th]. 10

[92] I. Donkin and J. M. Pawlowski, "The phase diagram of quantum gravity from diffeomorphism-invariant RG-flows," arXiv:1203.4207 [hep-th]. 10

[93] N. Christiansen, D. F. Litim, J. M. Pawlowski, and A. Rodigast, "Fixed points and infrared completion of quantum gravity," *Phys.Lett.* **B728** (2014) 114–117, arXiv:1209.4038 [hep-th]. 10

[94] A. Codello, G. D'Odorico, and C. Pagani, "Consistent closure of RG flow equations in quantum gravity," arXiv:1304.4777 [gr-qc]. 10, 85

[95] W. Souma, "Non-trivial ultraviolet fixed point in quantum gravity," *Prog. Theor. Phys.* **102** (1999) 181–195, arXiv:hep-th/9907027. 10

[96] M. Reuter and F. Saueressig, "Renormalization group flow of quantum gravity in the Einstein-Hilbert truncation," *Phys.Rev.* **D65** (2002) 065016, arXiv:hep-th/0110054 [hep-th]. 10

[97] D. Litim and A. Satz, "Limit cycles and quantum gravity," arXiv:1205.4218 [hep-th]. 10

[98] N. Christiansen, B. Knorr, J. M. Pawlowski, and A. Rodigast, "Global Flows in Quantum Gravity," arXiv:1403.1232 [hep-th]. 10

[99] A. Codello, R. Percacci, and C. Rahmede, "Investigating the Ultraviolet Properties of Gravity with a Wilsonian Renormalization Group Equation," *Annals Phys.* **324** (2009) 414–469, arXiv:0805.2909 [hep-th]. 10, 11, 13, 14, 16, 20

[100] P. F. Machado and F. Saueressig, "On the renormalization group flow of f(R)-gravity," *Phys. Rev.* **D77** (2008) 124045, arXiv:0712.0445 [hep-th]. 10, 20

[101] D. Benedetti, P. F. Machado, and F. Saueressig, "Asymptotic safety in higher-derivative gravity," *Mod. Phys. Lett.* **A24** (2009) 2233–2241, arXiv:0901.2984 [hep-th]. 10, 11

[102] K. Groh, S. Rechenberger, F. Saueressig, and O. Zanusso, "Higher Derivative Gravity from the Universal Renormalization Group Machine," *PoS* **EPS-HEP2011** (2011) 124, arXiv:1111.1743 [hep-th]. 10, 11

[103] A. Eichhorn and H. Gies, "Ghost anomalous dimension in asymptotically safe quantum gravity," *Phys.Rev.* **D81** (2010) 104010, arXiv:1001.5033 [hep-th]. 10

[104] K. Groh and F. Saueressig, "Ghost wave-function renormalization in Asymptotically Safe Quantum Gravity," *J.Phys.* **A43** (2010) 365403, arXiv:1001.5032 [hep-th]. 10

[105] M. Reuter and F. Saueressig, "Functional Renormalization Group Equations, Asymptotic Safety, and Quantum Einstein Gravity," *arXiv:hep-th/0708.1317* (2007) , arXiv:0708.1317 [hep-th]. 10

[106] J. York, James W., "Conformatlly invariant orthogonal decomposition of symmetric tensors on Riemannian manifolds and the initial value problem of general relativity," *J.Math.Phys.* **14** (1973) 456–464. 12

[107] I. Avramidi, "Heat kernel and quantum gravity," *Lect.Notes Phys.* **M64** (2000) 1–149. 18

[108] A. Bonanno, A. Contillo, and R. Percacci, "Inflationary solutions in asymptotically safe f(R) theories," *Class. Quant. Grav.* **28** (2011) 145026, arXiv:1006.0192 [gr-qc]. 20

[109] D. Benedetti and F. Caravelli, "The Local potential approximation in quantum gravity," *JHEP* **1206** (2012) 017, arXiv:1204.3541 [hep-th]. 20

[110] J. A. Dietz and T. R. Morris, "Asymptotic safety in the f(R) approximation," *JHEP* **1301** (2013) 108, arXiv:1211.0955 [hep-th]. 20, 23, 109

[111] J. A. Dietz and T. R. Morris, "Redundant operators in the exact renormalisation group and in the f(R) approximation to asymptotic safety," arXiv:1306.1223 [hep-th]. 20

[112] D. F. Litim and L. Vergara, "Subleading critical exponents from the renormalization group," *Phys.Lett.* **B581** (2004) 263–269, arXiv:hep-th/0310101 [hep-th]. 29, 42

[113] "Gnu multiple precision library." https://gmplib.org. 30

[114] "boost c++ libraries." http://www.boost.org. 30

[115] H. Kawai and M. Ninomiya, "Renormalization Group and Quantum Gravity," *Nucl.Phys.* **B336** (1990) 115. 45

[116] D. J. Gross and F. Wilczek, "Ultraviolet Behavior of Nonabelian Gauge Theories," *Phys.Rev.Lett.* **30** (1973) 1343–1346. 53

[117] H. D. Politzer, "Reliable Perturbative Results for Strong Interactions?," *Phys.Rev.Lett.* **30** (1973) 1346–1349. 53

[118] D. F. Litim and F. Sannino, "Asymptotic safety guaranteed," arXiv:1406.2337 [hep-th]. 54, 86, 110

[119] D. F. Litim, M. Mojaza, and F. Sannino, "Vacuum stability of asymptotically safe gauge-Yukawa theories," arXiv:1501.03061 [hep-th]. 54, 110

[120] P. Dona and R. Percacci, "Functional renormalization with fermions and tetrads," *Phys.Rev.* **D87** (2013) 045002, arXiv:1209.3649 [hep-th]. 56

[121] A. Barvinsky and G. Vilkovisky, "The Generalized Schwinger-Dewitt Technique in Gauge Theories and Quantum Gravity," *Phys.Rept.* **119** (1985) 1–74. 56

[122] M. Moshe and J. Zinn-Justin, "Quantum field theory in the large N limit: A Review," *Phys.Rept.* **385** (2003) 69–228, arXiv:hep-th/0306133 [hep-th]. 63

[123] K. Falls, "Asymptotic safety and the cosmological constant," arXiv:1408.0276 [hep-th]. 85

[124] L. Randall and R. Sundrum, "A Large mass hierarchy from a small extra dimension," *Phys.Rev.Lett.* **83** (1999) 3370–3373, arXiv:hep-ph/9905221 [hep-ph]. 87

[125] L. Lonnblad and M. Sjodahl, "Classical and non-classical ADD-phenomenology with high-E (perpendicular) jet observables at collider experiments," *JHEP* **0610** (2006) 088, arXiv:hep-ph/0608210 [hep-ph]. 88

[126] R. Sundrum, "Effective field theory for a three-brane universe," *Phys.Rev.* **D59** (1999) 085009, arXiv:hep-ph/9805471 [hep-ph]. 88

[127] T. Han, J. D. Lykken, and R.-J. Zhang, "On Kaluza-Klein states from large extra dimensions," *Phys. Rev.* **D59** (1999) 105006, arXiv:hep-ph/9811350. 88, 93

[128] P. Aichelburg and R. Sexl, "On the Gravitational field of a massless particle," *Gen.Rel.Grav.* **2** (1971) 303–312. 88

[129] J. Hewett and T. Rizzo, "Collider Signals of Gravitational Fixed Points," *JHEP* **0712** (2007) 009, arXiv:0707.3182 [hep-ph]. 88

[130] D. F. Litim and T. Plehn, "Signatures of gravitational fixed points at the LHC," *Phys. Rev. Lett.* **100** (2008) 131301, arXiv:0707.3983 [hep-ph]. 88, 96

[131] J. P. Brinkmann, "Unitarity of Higgs Scattering in Extra Dimensional Models within Fixed Point Gravity," diploma thesis, Lehrstuhl für Theoretische Physik III, Fakulät für Physik, Technische Universität Dortmund, 2009. 88

[132] E. Gerwick, "Asymptotically Safe Gravitons in Electroweak Precision Physics," *Eur.Phys.J.* **C71** (2011) 1676, arXiv:1012.1118 [hep-ph]. 88

[133] J. Schröder, "Unitarity Bounds for Higgs Scattering within a 4+n dimensional setup of Fixed Point Gravity," diploma thesis, Lehrstuhl für Theoretische Physik III, Fakultät für Physik, Technische Universität Dortmund, 2011. 88, 98

[134] M. Demmel, "Real Graviton Production in Asymptotically-Safe Quantum Gravity," diploma thesis, TU Dortmund, 2011. 88

[135] J. P. Brinkmann, G. Hiller, D. F. Litim, and J. Schröder, "to appear," arXiv:to appear. to appear. 88, 98, 99

[136] J. P. Dabruck, "Constraining Asymptotically Safe Quantum Einstein Gravity in Large Extra Dimensions," diploma thesis, TU Dortmund, 2012. 88

[137] M. Zenglein, "Diphoton signals of asymptotically safe gravity at the LHC," Master's thesis, TU Dortmud, 2014. 88

[138] H. Sedello, *Collider Physics in Anticipation of new TeV-scale Phenomena*. PhD thesis, TU Dortmund, 2014. 88

[139] K. Falls, D. F. Litim, and A. Raghuraman, "Black Holes and Asymptotically Safe Gravity," *Int.J.Mod.Phys.* **A27** (2012) 1250019, arXiv:1002.0260 [hep-th]. 88

[140] D. Becker and M. Reuter, "Asymptotic Safety and Black Hole Thermodynamics," arXiv:1212.4274 [hep-th]. 88

[141] K. Falls and D. F. Litim, "Black hole thermodynamics under the microscope," *Phys.Rev.* **D89** no. 8, (2014) 084002, arXiv:1212.1821 [gr-qc]. 88

[142] D. F. Litim and K. Nikolakopoulos, "Quantum gravity effects in Myers-Perry space-times," *JHEP* **1404** (2014) 021, arXiv:1308.5630 [hep-th]. 88

[143] B. Koch, C. Contreras, P. Rioseco, and F. Saueressig, "Black holes and running couplings: A comparison of two complementary approaches," arXiv:1311.1121 [hep-th]. 88

[144] B. Koch and F. Saueressig, "Structural aspects of asymptotically safe black holes," *Class.Quant.Grav.* **31** (2014) 015006, arXiv:1306.1546 [hep-th]. 88

[145] B. Koch and F. Saueressig, "Black holes within Asymptotic Safety," *Int.J.Mod.Phys.* **A29** no. 8, (2014) 1430011, arXiv:1401.4452 [hep-th]. 88

[146] T. Banks and W. Fischler, "A Model for high-energy scattering in quantum gravity," arXiv:hep-th/9906038 [hep-th]. 90

[147] S. D. Hsu, "Quantum production of black holes," *Phys.Lett.* **B555** (2003) 92–98, arXiv:hep-ph/0203154 [hep-ph]. 90

[148] H. Cheng and T. Wu, *Expanding Protons: Scattering at High Energies*. MIT Press, 1987. 93

[149] M. Levy and J. Sucher, "Eikonal approximation in quantum field theory," *Phys.Rev.* **186** (1969) 1656–1670. 93

[150] L. Cornalba, M. S. Costa, and J. Penedones, "Eikonal approximation in AdS/CFT: Resumming the gravitational loop expansion," *JHEP* **0709** (2007) 037, arXiv:0707.0120 [hep-th]. 93

[151] S. B. Giddings, M. Schmidt-Sommerfeld, and J. R. Andersen, "High energy scattering in gravity and supergravity," *Phys.Rev.* **D82** (2010) 104022, arXiv:1005.5408 [hep-th]. 93

[152] D. Amati, M. Ciafaloni, and G. Veneziano, "Superstring Collisions at Planckian Energies," *Phys.Lett.* **B197** (1987) 81. 93, 110

[153] D. Amati, M. Ciafaloni, and G. Veneziano, "Classical and Quantum Gravity Effects from Planckian Energy Superstring Collisions," *Int.J.Mod.Phys.* **A3** (1988) 1615–1661. 93

[154] D. Amati, M. Ciafaloni, and G. Veneziano, "Can Space-Time Be Probed Below the String Size?," *Phys.Lett.* **B216** (1989) 41. 93

[155] D. Amati, M. Ciafaloni, and G. Veneziano, "Higher Order Gravitational Deflection and Soft Bremsstrahlung in Planckian Energy Superstring Collisions," *Nucl.Phys.* **B347** (1990) 550–580. 93

[156] D. Amati, M. Ciafaloni, and G. Veneziano, "Planckian scattering beyond the semiclassical approximation," *Phys.Lett.* **B289** (1992) 87–91. 93

[157] E. Sessolo and D. McKay, "Eikonal contributions to ultra high energy neutrino-nucleon cross sections in low scale gravity models," *Phys.Lett.* **B668** (2008) 396–403, arXiv:0803.3724 [hep-ph]. 95

[158] P. T. Anderson (Director), "There Will Be Blood." Paramount vantage and miramax films, 2007. 127

Appendix A

Traces for the improved flow equation

Here we provide the explicit values for the traces necessary to obtain the right hand side (2.67) of the improved flow equation (3.5). The improved flow is introduced in Chapter 3 to remove the explicit poles $\rho = 3$ and $\rho = 4$ in the flow (2.85). It achieves this by exploiting the freedom to choose a suitable regulator for certain traces: the gravitational vector mode ξ (A.4) and the scalar modes σ (A.7) and (A.8), η (A.17) and (A.18), λ (A.27) and (A.28), ω (A.34) and (A.35).

The gravitational contributions are:

$$\Delta_{h^T h^T} = -\nabla^2 \tag{A.1}$$

$$\Gamma^{(2)}_{h^T h^T} = -\frac{f}{2} - \left(\frac{\Delta_{h^T h^T}}{2} - \frac{\rho}{6}\right) \tag{A.2}$$

$$\begin{aligned}\frac{1}{2}\,\mathrm{Tr}\left[\frac{\partial_t \mathcal{R}_k^{h^T h^T}}{\Gamma^{(2)}_{h^T h^T} + \mathcal{R}_k^{h^T h^T}}\right] &= \frac{\left(311\rho^3 - 126\,\rho^2 - 22680\,\rho + 45360\right)\left(\partial_t f' - 2\,\rho\, f''\right)}{580608\,\pi^2\,\left(3\,f - (\rho-3)\,f'\right)} \\ &\quad + \frac{2\left(311\,\rho^3 - 252\,\rho^2 - 68040\,\rho + 181440\right) f'}{580608\,\pi^2\,\left(3\,f - (\rho-3)\,f'\right)}\end{aligned} \tag{A.3}$$

$$\Delta_{\xi\xi} = -\nabla^2 - \frac{\rho}{4} \tag{A.4}$$

$$\Gamma^{(2)}_{\xi\xi} = \Delta^2_{\xi\xi} \tag{A.5}$$

$$\frac{1}{2}\,\mathrm{Tr}'\left[\frac{\partial_t \mathcal{R}_k^{\xi\xi}}{\Gamma^{(2)}_{\xi\xi} + \mathcal{R}_k^{\xi\xi}}\right] = \frac{-191\,\rho^2 + 720\,\rho + 1080}{5760\pi^2} \tag{A.6}$$

$$\Delta_{\sigma\sigma,1} = -\nabla^2 \tag{A.7}$$

$$\Delta_{\sigma\sigma,2} = -\nabla^2 - \frac{\rho}{3} \tag{A.8}$$

$$\Gamma^{(2)}_{\sigma\sigma} = \frac{9}{16}\,\Delta_{\sigma\sigma,1}\,\Delta^2_{\sigma\sigma,2} \tag{A.9}$$

$$\frac{1}{2}\,\mathrm{Tr}''\left[\frac{\partial_t \mathcal{R}^{\sigma\sigma}_k}{\Gamma^{(2)}_{\sigma\sigma} + \mathcal{R}^{\sigma\sigma}_k}\right] = \frac{-117\,\rho^2 + 280\,\rho + 360}{3840\,\pi^2} \tag{A.10}$$

$$\Delta_{hh} = -\nabla^2 \tag{A.11}$$

$$\Gamma^{(2)}_{hh} = \frac{f}{8} + \left(\frac{3}{16}\,\Delta^2_{hh} - \frac{\rho}{8}\right)\,f' + \left(\frac{3}{4}\,\Delta^2_{hh} - \frac{\rho}{4}\right)^2\,f'' \tag{A.12}$$

$$\begin{aligned}
\frac{1}{2}\,\mathrm{Tr}\left[\frac{\partial_t \mathcal{R}^{hh}_k}{\Gamma^{(2)}_{hh} + \mathcal{R}^{hh}_k}\right] &= \frac{\left(3258\,\rho^5 + 58464\,\rho^4 + 275184\,\rho^3 - 1632960\,\rho\right)\,f^{(3)}}{11612160\,\pi^2\,\left((\rho-3)^2\,f'' + (3-2\rho)\,f' + 2\,f\right)} \\
&+ \frac{\left(-1480\,\rho^4 - 87696\,\rho^3 - 731808\,\rho^2 - 362880\rho + 6531840\right)\,f''}{11612160\,\pi^2\,\left((\rho-3)^2\,f'' + (3-2\rho)\,f' + 2\,f\right)} \\
&+ \frac{8\,\left(185\,\rho^3 + 7308\,\rho^2 + 68040\,\rho + 181440\right)\,f'}{11612160\,\pi^2\,\left((\rho-3)^2\,f'' + (3-2\rho)\,f'(R) + 2\,f\right)} \\
&+ \frac{\left(-1629\,\rho^4 - 29232\,\rho^3 - 137592\,\rho^2 + 816480\right)\,\partial_t f''}{11612160\,\pi^2\,\left((\rho-3)^2\,f'' + (3-2\rho)\,f' + 2\,f\right)} \\
&+ \frac{4\,\left(185\,\rho^3 + 3654\,\rho^2 + 22680\,\rho + 45360\right)\,\partial_t f'}{11612160\,\pi^2\,\left((\rho-3)^2\,f'' + (3-2\rho)\,f' + 2\,f\right)}
\end{aligned} \tag{A.13}$$

The ghosts contribute with:

$$\Delta_{\bar{C}^T C^T} = -\nabla^2 - \frac{\rho}{4} \tag{A.14}$$

$$\Gamma^{(2)}_{\bar{C}^T C^T} = -\Delta_{\bar{C}^T C^T} \tag{A.15}$$

$$\frac{1}{2}\,\mathrm{Tr}'\left[\frac{\partial_t \mathcal{R}^{\bar{C}^T C^T}_k}{\Gamma^{(2)}_{\bar{C}^T C^T} + \mathcal{R}^{\bar{C}^T C^T}_k}\right] = \frac{-191\,\rho^2 + 720\,\rho + 1080}{11520\,\pi^2} \tag{A.16}$$

$$\Delta_{\bar{\eta}\eta,1} = -\nabla^2 \tag{A.17}$$

$$\Delta_{\bar{\eta}\eta,2} = -\nabla^2 - \frac{\rho}{3} \tag{A.18}$$

$$\Gamma^{(2)}_{\bar{\eta}\eta} = \frac{9}{16}\,\Delta_{\bar{\eta}\eta,1}\,\Delta_{\bar{\eta}\eta,2} \tag{A.19}$$

$$\frac{1}{2}\,\mathrm{Tr}''\left[\frac{\partial_t \mathcal{R}^{\bar{\eta}\eta}_k}{\Gamma^{(2)}_{\bar{\eta}\eta} + \mathcal{R}^{\bar{\eta}\eta}_k}\right] = \frac{-391\,\rho^2 + 720\,\rho + 1080}{17280\,\pi^2} \tag{A.20}$$

The auxiliary fields enter as:

$$\Delta_{\bar{c}^T c^T} = -\nabla^2 - \frac{\rho}{4} \tag{A.21}$$

$$\Gamma^{(2)}_{\bar{c}^T c^T} = 2\,\Delta_{\bar{c}^T c^T} \tag{A.22}$$

$$\frac{1}{2}\,\mathrm{Tr}'\left[\frac{\partial_t \mathcal{R}^{\bar{c}^T c^T}_k}{\Gamma^{(2)}_{\bar{c}^T c^T} + \mathcal{R}^{\bar{c}^T c^T}_k}\right] = \frac{-191\,\rho^2 + 720\,\rho + 1080}{11520\,\pi^2} \tag{A.23}$$

$$\Delta_{\zeta^T\zeta^T} = -\nabla^2 - \frac{\rho}{4} \tag{A.24}$$

$$\Gamma^{(2)}_{\zeta^T\zeta^T} = 4\,\Delta_{\zeta^T\zeta^T} \tag{A.25}$$

$$\frac{1}{2}\,\mathrm{Tr}'\left[\frac{\partial_t \mathcal{R}_k^{\zeta^T\zeta^T}}{\Gamma^{(2)}_{\zeta^T\zeta^T} + \mathcal{R}_k^{\zeta^T\zeta^T}}\right] = \frac{-191\,\rho^2 + 720\,\rho + 1080}{11520\,\pi^2} \tag{A.26}$$

$$\Delta_{\bar{\lambda}\lambda,1} = -\nabla^2 \tag{A.27}$$

$$\Delta_{\bar{\lambda}\lambda,2} = -\nabla^2 - \frac{\rho}{3} \tag{A.28}$$

$$\Gamma^{(2)}_{\bar{\lambda}\lambda} = \frac{3}{4}\,\Delta_{\bar{\lambda}\lambda,1}\,\Delta_{\bar{\lambda}\lambda,2} \tag{A.29}$$

$$\frac{1}{2}\,\mathrm{Tr}''\left[\frac{\partial_t \mathcal{R}_k^{\bar{\lambda}\lambda}}{\Gamma^{(2)}_{\bar{\lambda}\lambda} + \mathcal{R}_k^{\bar{\lambda}\lambda}}\right] = \frac{-391\,\rho^2 + 720\,\rho + 1080}{17280\,\pi^2} \tag{A.30}$$

$$\Delta_{\bar{s}s} = -\nabla^2 \tag{A.31}$$

$$\Gamma^{(2)}_{\bar{s}s} = \Delta_{\bar{s}s} \tag{A.32}$$

$$\frac{1}{2}\,\mathrm{Tr}''\left[\frac{\partial_t \mathcal{R}_k^{\bar{s}s}}{\Gamma^{(2)}_{\bar{s}s} + \mathcal{R}_k^{\bar{s}s}}\right] = \frac{-511\,\rho^2 + 360\,\rho + 1080}{34560\,\pi^2} \tag{A.33}$$

$$\Delta_{\omega\omega,1} = -\nabla^2 \tag{A.34}$$

$$\Delta_{\omega\omega,2} = -\nabla^2 - \frac{\rho}{3} \tag{A.35}$$

$$\Gamma^{(2)}_{\omega\omega} = \frac{3}{2}\,\Delta_{\omega\omega,1}\,\Delta_{\omega\omega,2} \tag{A.36}$$

$$\frac{1}{2}\,\mathrm{Tr}''\left[\frac{\partial_t \mathcal{R}_k^{\omega\omega}}{\Gamma^{(2)}_{\omega\omega} + \mathcal{R}_k^{\omega\omega}}\right] = \frac{-391\,\rho^2 + 720\,\rho + 1080}{17280\,\pi^2} \tag{A.37}$$

This provides all the required information to explicitly compute the right hand side of the flow (2.67).

I'm finished.

-*Daniel Plainview* in the film *There Will Be Blood* [158]